Molecular-based optical measurement techniques for transition and turbulence in high-speed flow

Brett F. Bathel[*] and Paul M. Danehy[†]
NASA Langley Research Center, Hampton, Virginia, 23681-2199

Andrew D. Cutler[‡]
The George Washington University, Newport News, VA 23602, USA

1. Introduction

High-speed laminar-to-turbulent transition and turbulence affect the control of flight vehicles, the heat transfer rate to a flight vehicle's surface, the material selected to protect such vehicles from high heating loads, the ultimate weight of a flight vehicle due to the presence of thermal protection systems, the efficiency of fuel-air mixing processes in high-speed combustion applications, etc. Gaining a fundamental understanding the physical mechanisms involved in the transition process will lead to the development of predictive capabilities that can identify transition location and its impact on parameters like surface heating. Currently, there is no general theory that can completely describe the transition-to-turbulence process. However, transition research has led to the identification of the predominant pathways by which this process occurs. Figure 1.1, taken from Ref. 1, graphically depicts the known pathways by which by which an initially stable, laminar boundary layer can become unstable, undergo a process of instability growth, and eventually break down into turbulence. For a truly physics-based model of transition to be developed, the individual stages in the paths leading to the onset of fully turbulent flow must be well understood. This requires that

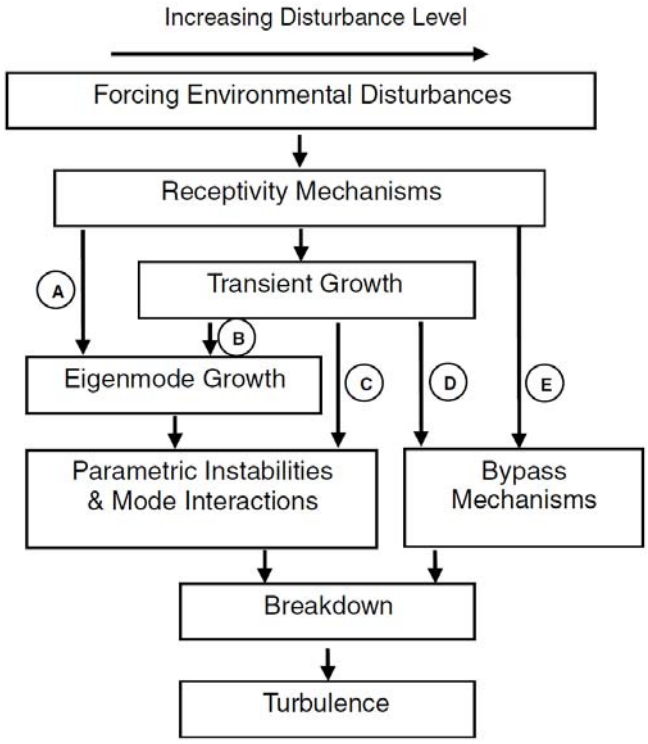

Figure 1.1: Transition pathways from laminar to turbulent flow. Image taken from Ref. 1. (Reprinted with permission of the author and the American Institute of Aeronautics and Astronautics).

[*] Graduate Student, University of Virginia and NASA Graduate Co-op, Hampton, Virginia.
[†] Research Scientist, Advanced Sensing and Optical Measurement Branch, MS 493.
[‡] Professor, Mechanical and Aerospace Engineering Department, 1 Old Oyster Point Road, Suite 200.

each pathway be computationally modeled and experimentally characterized and validated. This may also lead to the discovery of new physical pathways.

The path to transition in Figure 1 begins with the presence of an initial disturbance, either in the freestream flow or within the boundary layer itself. Disturbances can be classified into one of three types: entropy spots (related to temperature fluctuations), vorticity, and sound. [2] Disturbances in the freestream can originate in the settling chamber of a high-speed wind tunnel and pass into the test section. Entropy spots and vorticity originating in the settling chamber can be convected into the test section.[3,4] Sound disturbances can originate in the settling chamber, from the wind tunnel nozzle walls, and along the wind tunnel walls.[3,4] Sound radiating from the nozzle walls is of particular concern as it is the dominant source of noise in high-speed wind tunnels,[5] with its magnitude scaling with Mach number to the fourth power.[6] These disturbances can significantly alter the transition-to-turbulence process.[6-9] Low-disturbance, high-speed wind tunnels have been developed to mitigate these disturbances.5 These *quiet tunnels* provide a hypersonic freestream flow with disturbance levels similar to those encountered in flight, with freestream pressure fluctuations of less than 0.1%.[6] However, they are limited in extent of Reynolds number, Mach number, and enthalpy operability.[10] Table 1.1 provides velocity (U), temperature (T), mass-flow (m), and pressure (P) fluctuation levels for two conventional hypersonic tunnels[10-12] and one quiet hypersonic tunnel[13,14] as measured with hot-wire (U, T, m) or Pitot (P) probes.

Table 1.1: Measured or computed maximum fluctuation magnitudes in high-speed wind tunnel facilities.

Tunnel Freestream Property	Von Karman Institute Mach 6 Hypersonic Wind Tunnel H3	NASA Langley 20-Inch Mach 6	Purdue Boeing/AFOSR Mach 6 Quiet Tunnel
$U'/\bar{U}$	0.6 %* (Ref. 15)	-	-
$T'/\bar{T}$	0.8 % (Ref. 15)	0.20 % (Ref. 16)	-
$m'/\bar{m}$	5.2 % (Ref. 15)	1.01 % (Ref. 16)	0.2 %** (Ref. 13)
$P'/\bar{P}$	1.0 % (Ref. 15)	1.6 % (Ref. 17)	0.01 % (Ref. 18)

* Derived value
** Measurement made within laminar boundary layer

Disturbances that originate within the boundary layer can be caused by a number of factors, including the presence of discrete two-dimensional and three-dimensional roughness elements, cavities, distributed roughness, and mass injection. Various roughness types, cavity types, and mass injection schemes have been used in transition experiments at NASA Langley.[19-22] The influence of roughness on the hypersonic transition process varies, although transition typically moves forward (i.e. upstream) with increasing roughness height. [23] A roughness Reynolds number of the form $Re_k = \rho_k U_k k/\mu_k$, with k being the roughness height and all other parameters (density, ρ, velocity, U, and viscosity, μ) evaluated at k, is often used in correlation-based approaches to estimate transition location[23] or the effectiveness of inducing transition behavior in the wake region or immediate vicinity of the trip.[24] There is no physical mechanism-based theory for roughness-induced transition, although roughness can generate streamwise

vorticity, a wake shear layer, and can interact with incident freestream disturbances.[23] These disturbances then enter the boundary via the receptivity process Streamwise vorticity generation can result in transient growth instability amplification.[23,25] Mass-flow fluctuation amplitude and frequency measurements in the wake of a roughness element in a quiet tunnel were performed in Ref. 13, with sample results are listed in Table 1.2. Note that the percentage fluctuations are ~2 orders of magnitude larger than the freestream fluctuations in a quiet wind tunnel (Table 1.1).

Table 1.2: Measured or computed maximum fluctuation magnitudes in high speed transition and turbulent flows.

Property	Transition downstream of a large roughness element in a laminar boundary layer	Fully Developed Hypersonic Turbulent Boundary Layer (non-reacting)
$U'/\bar{U}$	25 % (Ref. 26)	15 % (Ref. 27)
$T'/\bar{T}$	33 % (Ref. 26)	47 % (Ref. 27)
$m'/\bar{m}$	43 % (Ref. 13)	52 % (Ref. 27)
$P'/\bar{P}$	5 % (Ref. 13)	7.5 % (Ref. 27)

Receptivity is the process by which either the freestream or roughness-generated disturbances mentioned are coupled into the boundary layer flow, generating and/or enhancing instabilities.[28] Returning to Fig. 1, the magnitude of the imparted disturbance determines which pathway to turbulence they will follow. Reviews of the various instability types encountered along paths A-E in Fig. 1 can be found in the literature.[29 - 34] Both computational and experimental studies have been performed to study the interaction of the disturbances with the various instability mechanisms.[35] The majority of experiments used to conduct these studies involve physical probes, which are either surface mounted or placed in the boundary layer flow itself, to measure disturbance parameters. In low-speed environments, the magnitude of these disturbances varies from a few hundredths of a percent to ~10%.[36] Similar magnitudes can be expected for higher-speed flows.[37] Experiments characterizing normalized amplitude growth of instabilities for supersonic and hypersonic cases have also been conducted.[38]

Fully developed turbulent flowfields are computed using several different computational fluid dynamics (CFD) approaches including Reynolds Averaged Navier Stokes (RANS), Large Eddy Simulation (LES) and Direct Numerical Simulation (DNS) and other methods, including hybrid techniques.[39] Unfortunately, experimental high-speed hypersonic turbulence data is very sparse. For experimental data in this regime that does exist, much of it is absent chemistry effects, which play a critical role in high hypersonic Mach number flows.[40] Even when limiting discussion to perfect gas experimentation, measurements of turbulent fluctuations in the hypersonic regime with hot-wire probes appear to suffer from many of the limitations, as discussed below.[40] Therefore, molecular-based optical diagnostics seem well-poised for both non-reacting and reacting high-speed turbulent flow measurements. A survey was recently commissioned by NASA to look at simulation requirements, technology gaps and critical impediments that need to be overcome to greatly enhance CFD analysis and design capabilities by the year 2030.[41] The report found that "The single greatest impediment mentioned by a majority of the survey participants is the lack of foundational building-block validation datasets

for physical model development." Such datasets would benefit from optical diagnostics such as those described herein. The right hand column of Table 1.2 shows computed property fluctuations in a fully developed non-reacting boundary layer.

Tables 1.1 and 1.2 provide indications of the measurement precisions that would be required to resolve the relevant flow property fluctuations in different applications. These data provide a guide for comparison with the individual measurement technique's capabilities detailed below. Measurement precision is a key consideration in developing measurement technology for transitional and turbulent flows because precise instruments are needed to measure the fluctuations and the growth of the fluctuations. Ideally, an instrument's precision would be negligible compared to the fluctuations in the parameter being measured. When choosing to implement a particular measurement approach, additional considerations are also important. These include considerations of the required accuracy, frequency response, the prior experience of the research team, available equipment, available budget and other factors. These factors are discussed in more detail in the Conclusions.

As stated previously, some of the more common measurement devices for flowfield transition-to-turbulence and turbulent boundary layer measurements include hot-wires and Pitot probes. While hot-wire probes can have a response time and dynamic range appropriate for high-speed measurements, they only provide data at a point, are difficult to calibrate,[36] are fragile, have limited bandwidth,[37] and are intrusive.[10] Pitot probes, while more robust than hot-wires, have similar issues. Since the fluctuation levels associated with the onset of instabilities is an order-of-magnitude less than those associated with turbulence,[37] the intrusive nature of such probes can have an adverse effect on the parameter being measured. Limitations on bandwidth preclude these physical probes from resolving high-speed, high-frequency instability modes, with bandwidths of ~1 MHz being desired.[37] Additionally, the point-wise nature of data acquisition prevents the detailed study of spatial behavior of transition-to-turbulence and fully-developed turbulent behavior. A review of some of the available non-intrusive optical diagnostic capabilities with applicability to transition-to-turbulence measurements is available in Ref. 37.

This document is intended to describe molecular based measurement techniques that have been developed, addressing the needs of the high-speed transition-to-turbulence and high-speed turbulence research fields. In particular, we focus on techniques that have either been used to study high speed transition and turbulence or techniques that show promise for studying these flows. This review is not exhaustive. In addition to the probe-based techniques described in the previous paragraph, several other classes of measurement techniques that are, or could be, used to study high speed transition and turbulence are excluded from this manuscript. For example, surface measurement techniques such as pressure and temperature paint, phosphor thermography, skin friction measurements and photogrammetry (for model attitude and deformation measurement) are excluded to limit the scope of this report. Other physical probes such as heat flux gauges, total temperature probes are also excluded. We further exclude

measurement techniques that require particle seeding though particle based methods may still be useful in many high speed flow applications.

This manuscript details some of the more widely used molecular-based measurement techniques for studying transition and turbulence: laser-induced fluorescence (LIF), Rayleigh and Raman Scattering and coherent anti-Stokes Raman scattering (CARS). These techniques are emphasized, in part, because of the prior experience of the authors. Additional molecular based techniques are described, albeit in less detail. Where possible, an effort is made to compare the relative advantages and disadvantages of the various measurement techniques, although these comparisons can be subjective views of the authors. Finally, the manuscript concludes by evaluating the different measurement techniques in view of the precision requirements described in this chapter. Additional requirements and considerations are discussed to assist with choosing an optical measurement technique for a given application.

2. Laser-Induced Fluorescence (LIF)

Laser-induced fluorescence (LIF) uses a laser to probe individual species within the flowfield, providing information pertaining to both the thermodynamic (pressure, temperature, mole fraction) and fluid dynamic state (velocity) of the gas. The laser can either be focused to a point for LIF measurements, formed into a thin sheet using a cylindrical and focusing lens in combination for planar LIF measurements (PLIF), or used to illuminate a volume for three-dimensional or stereoscopic imaging. Reviews of the laser-induced fluorescence measurement technique are available from Eckbreth[42] and others.[43,44] The measurement technique works by inducing a transition, usually of an electron, from a lower energy state (E_1) to an excited energy state (E_2) via stimulated absorption of one or more photons in the atomic or molecular species of interest. In a two-level model assumption, the atom or molecule of interest in the E_2 state then returns to the E_1 state by transferring energy via spontaneous emission of a photon (fluorescence), or by transferring energy non-radiatively through a collision with another atom or molecule (collisional quenching).

For an atom, such as N or O, the energy required to induce an absorption transition of an electron to the E_2 state from the ground (E_1) state is equal to the energy difference between the atom with an electron occupying the excited electronic orbital and the atom's ground electronic orbital configuration, respectively. For molecules, such as N_2 and O_2, the energies of the E_2 and E_1 states include the energies associated with the vibrational and rotational motion of the molecule in addition to the energy associated with the molecule's electronic configuration. Figure 2.1 shows a generalized two-level energy model for

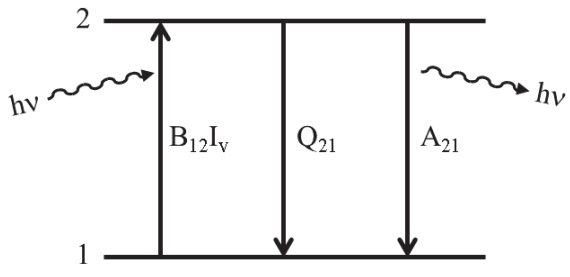

Figure 2.1: Two-level energy model of single-photon fluorescence.

fluorescence with the stimulated absorption transition induced by a single photon.

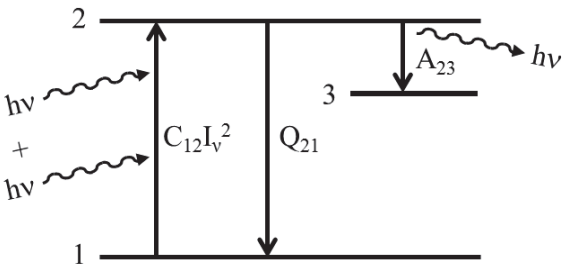

Figure 2.2: Two-level energy model of two-photon fluorescence.

In Fig. 2.1, the rate at which the absorbing medium in the E_1 state transitions to the E_2 state is proportional to the product of the Einstein coefficient for stimulated absorption, B_{12}, and the laser's spectral irradiance (power per unit area per unit frequency), $I_\nu = IL_\nu$, where I is the irradiance (power per unit area) and L_ν is the laser spectral profile or laser line-shape (per unit of frequency).[42] The energy of the absorbed and emitted photons is the frequency, ν, multiplied by Planck's constant, h. The Einstein A_{21} and B_{12} coefficients describe the probabilities for emission and absorption,[45] respectively, while Q_{21} is the collisional quenching rate. For absorbing species, the line-shape function, Y_ν, describes the spectral width for a particular energy level. This line-shape function combines broadening effects due to Gaussian-shaped Doppler broadening and Lorentzian-shaped homogeneous broadening mechanisms and is represented as:[42]

$$Y_\nu = \frac{2}{\Delta\nu_D}\sqrt{\frac{\ln(2)}{\pi}}V(a,x) \tag{2.1}$$

Here, $\Delta\nu_D$ is the Doppler-broadened line width due to the thermal motion of the absorbing species and $V(a,x)$ is the Voigt integral function describing the convolution of homogeneous and Doppler broadening mechanisms. The line-width resulting from Doppler broadening is given by:[42,45]

$$\Delta\nu_D = \frac{\nu_0}{c}\sqrt{\frac{8\ln(2)k_BT}{m}} \tag{2.2}$$

Here, ν_0 is the transition center frequency, c is the speed of light, k_B is the Boltzmann constant, T the temperature, and m the species mass. The Voigt integral function is given by:[42]

$$V(a,x) = \frac{a}{\pi}\int_{-\infty}^{\infty}\frac{e^{-y^2}}{a^2+(x-y)^2}dy \tag{2.3}$$

where $a = (\Delta\nu_H/\Delta\nu_D)\sqrt{\ln(2)}$ accounts for effects of homogeneous broadening ($\Delta\nu_H$) and $x = \{(\nu-\nu_0)/\Delta\nu_D\}\sqrt{4\ln(2)}$. Methods for computing this integral are given in Refs. 46-48.

The integral of the product of the absorption line-shape function, Y_ν, and the laser's spectral profile, L_ν, is defined by the overlap integral, $G = \int L_\nu Y_\nu d\nu$, and describes what portion of a particular absorption transition is affected by the incident laser radiation. The rate constant for

stimulated absorption, W_{12}, which describes the rate at which species in E_1 transition to E_2 via absorption of a single photon[42,44] is given by:

$$W_{12} = B_{12}IG \tag{2.4}$$

As the laser passes through a flowfield, it is absorbed at a rate corresponding to Eq. 2.4, inducing a transition between the E_1 and E_2 states. Consequently, as the laser continues to propagate through the flowfield, the irradiance is continually diminished as a result of the absorption process. The Beer-Lambert law describes the magnitude of the decrease of the spectral irradiance, and is of the form:[49]

$$-dI_\nu = I_\nu k_s(\nu)dx \tag{2.5}$$

where k_s is the absorption coefficient. The absorption coefficient can be related to B_{12} by the relation $\int k_s(\nu)d\nu = N_S B_{12}\, h\nu_0/c$,[49] where N_S is the number density of the species, h is Plank's constant, and c the speed of light. Integrating Eq. 2.5 results in the relation:[49]

$$I_{\nu,x} = I_{\nu,0}e^{-k_s(\nu)x} \tag{2.6}$$

where $I_{\nu,0}$ is the incident spectral irradiance and $I_{\nu,x}$ the spectral irradiance after the beam travels a distance x.

In certain circumstances, the energy separation between the E_1 and E_2 states for the species being examined with LIF is such that the frequency of a photon necessary to induce an absorption transition is far into the ultra-violet portion of the electro-magnetic spectrum. However, achieving frequencies far into the UV with conventional laser systems can be difficult.[45] Additionally, strong absorption of UV radiation by many materials and gases (including air) below approximately 200 nm limits the application of laser systems capable of producing such frequencies.[42] One solution is to use two-photon LIF techniques to probe species having absorption transitions in the deep UV. With a two-photon technique, the frequency (and therefore energy) of each photon is half that required by a single photon for the same transition. Figure 2.2 shows a generalized two-photon fluorescence energy model for two-photon LIF. For atomic species, such as N or O, spontaneous emission is often observed between E_2 and an intermediate energy state, E_3.

For the two-photon LIF process in Fig. 2.2, the two-photon absorption cross-section results in a rate constant different from that in Eq. 2.4 and has the form:[42,45,50-53]

$$W_{12} = C_{12}I^2G \tag{2.7}$$

where C_{12} relates to the two-photon absorption cross-section. Note that the dependence of the rate constant scales with the square of the incident laser irradiance, I. This behavior arises from the probability of observing the simultaneous arrival of two photons, which is the square of the probability for the arrival of a single photon.[45]

In both Figures 1 and 2, Q_{21} is the so called *quenching* rate constant. It describes the rate at which energy is transferred through non-radiative collisions between excited atoms or molecules in the E_2 state and atomic or molecular collision partners of species i. This rate constant is computed similarly to that in Ref. 42 as:

$$Q_{21} = N_T \sum_i \chi_i \sigma_{s,i} v_{s,i} \tag{2.8}$$

where $N_T = P/k_B T$ is the total population of the excited state, χ_i is the mole fraction of quenching species i, $\sigma_{s,i}$ is the collision cross-section between the excited species, s, and quenching species, i, and $v_{s,i} = \sqrt{8k_B T_{trans}/\pi\mu_{s,i}}$ is the mean relative velocity[54,55] between the excited species and quenching species, with $\mu_{s,i}$ being their reduced mass and T_{trans} their translational temperature. The spontaneous emission coefficient, A, in Figures 1 and 2 is also known as the Einstein A coefficient and describes the probability for spontaneous emission of a photon by an atom or molecule in the excited state.[45]

For the two-level model in Fig. 2.1, the rate of change of the populations N_1 and N_2, in the E_1 and E_2 states, respectively, can be obtained from relations similar to those presented in Ref. 42:

$$\frac{dN_1}{dt} = -\frac{dN_2}{dt} = -N_1 W_{12} + N_2(Q_{21} + A_{21}) \tag{2.9}$$

$$N_1 + N_2 = N_S = \chi_s f_B N_T \tag{2.10}$$

Equation 2.10 is a conservation law saying that the combined populations of the E_1 and E_2 states is equal to the initial population of the excitation species' E_1 state, N_S, which is in turn the product of the species mole fraction, χ_s, the total population, N_T, and the temperature-dependent Boltzmann fraction, f_B. Equation 2.9 assumes that the laser intensity is sufficiently weak such that stimulated emission (W_{21}) can be neglected.

The Boltzmann fraction, f_B, describes the ratio of the number of absorbers initially occupying E_1 relative to all possible energy states at a particular temperature, T, when a system is in thermodynamic equilibrium.[55] This term has a general form given by:[42,55,56]

$$f_B = \frac{g_j e^{-E_j/k_B T}}{\sum_j g_j e^{-E_j/k_B T}} \tag{2.11}$$

where g_j is the degeneracy of state j. Degeneracy refers to the number of quantized states that exist in a given energy level, E_j.[55] The summation in the denominator is termed the *partition function*, Z, and for a diatomic molecule can be represented as the product of the individual partition functions for rotational and vibrational energies, $Z = Z_{rot} Z_{vib}$. The individual partition functions take a form similar to that in Ref. 55:

$$Z_{rot} = \sum_{J=0.5,1.5,2.5,\cdots}(2J+1)\exp\left[-\frac{F_J}{k_B T_{rot}}\right]$$
$$Z_{vib} = \sum_{v=0,1,2,\cdots}\exp\left[-\frac{G_v}{k_B T_{vib}}\right] \quad (2.12)$$

where J is the rotational quantum number, v is the vibrational quantum number, F_J the rotational energy, G_v the vibrational energy, T_{rot} the characteristic rotational temperature, and T_{vib} the characteristic vibrational temperature.

More involved differential rate equations can be formulated for the two-photon method like those presented in Ref. 53. It should be noted that the models presented in Figures 1 and 2 neglect transitions from E_1 to E_2 resulting from collisions, with a rate constant of Q_{12}. This is usually a good assumption for large energy separations associated with the visible or UV transitions typically employed for LIF. Transitions from the E_2 and E_3 states resulting from pre-dissociation (Q_{pre}) and ionization (Q_{ion}), which are described in Refs. 42 and 44, have also been neglected.

2.1 Linear, Steady State Solution

If a continuous laser source is used to populate the E_2 state and detection of fluorescence occurs well after this source is turned on, then N_2 can be assumed to have reached its steady-state value. From this assumption, the left-hand-side of Eq. 2.9 is set to zero, resulting in two algebraic equations (Eqs. 2.9 and 2.10) for two unknowns (N_1 and N_2). The same assumption can be made to determine the population, N_2, achieved by a pulsed laser source if the time required to reach steady state is short compared to the duration of the pulse. This population is computed as:

$$N_2 = \frac{\chi_s f_B N_T W_{12}}{W_{12}+Q_{21}+A_{21}} \quad (2.13)$$

The product of this excited state population and the spontaneous emission rate constant is N_2A_{21} and represents the number of transitions per unit time and per unit volume. Integrating this constant value with respect to time gives the total number of transitions per unit volume during the detection period. Substituting Eq. 2.4 for W_{12}, and assuming that W_{12} is small compared to A_{21} and Q_{21} (which is valid for low-intensity excitation), a relation for the total number of photons collected via fluorescence by the detection device is:[44]

$$S_{LIF} = \chi_s f_B N_T B_{12} I G \Phi t_{det} V \frac{\Omega}{4\pi}\eta \quad (2.14)$$

where $\Phi = A_{21}/(Q_{21}+A_{21})$ is the fluorescence yield, t_{det} is the period of detection, V is the volume probed by the laser source, Ω is the solid angle over which detection occurs, and η is the detection efficiency. The fluorescence yield, Φ, describes the fraction of de-excitation transitions that occur via spontaneous emission (fluorescence) relative to all de-excitation transitions (i.e. spontaneous emission and collisional quenching, assuming pre-dissociation and ionization are negligible). Neglecting the constants in Eq. 2.14, a generalized form for the fluorescence signal

similar to that presented in Refs. 44 and 57, including its thermodynamic (χ,P,T) dependencies and velocity dependence (arising from the Doppler effect), is:

$$S_{LIF} \propto \chi_s f_B(T) B_{12} I G(\chi_s, P, T, U) \Phi(\chi_s, \chi_i, P, T) t_{det} \tag{2.15}$$

2.2 Non-Steady State Solution

For a pulsed laser source, if N_2 is changing during the period of detection, then the entirety of Eq. 2.9 must be solved to obtain the time-dependent population, $N_2(t)$. Similarly, if the duration of the laser pulse is of the same order of magnitude as the time required to reach steady state, then the population at the end of the laser pulse, $N_2(t_{laser})$, can be obtained by solving Eq. 2.9. By assuming the laser intensity behaves as a Heaviside step function in time, the population $N_2(t)$, existing during laser excitation can be calculated by substituting the relation for N_1 from Eq. 2.10 into Eq. 2.9 and integrating with respect to time:[44]

$$N_2(t) = \chi_s f_B N_T \frac{W_{12}}{r} \cdot (1 - e^{-rt}),\ 0 < t \leq t_{laser} \tag{2.16}$$

where $r = W_{12} + Q_{21} + A_{21}$. The inverse of this value, r^{-1}, is the characteristic time needed to achieve steady state. This solution assumes an initial condition which typically specifies the initial excited state population to be zero ($N_2(0) = 0$).

When the laser source is turned off, the only pathways to return to the ground state from the excited state are assumed to be through either spontaneous emission or collisional quenching. Therefore, for the period following laser excitation, the first term on the right-hand-side of Eq. 2.9 is zero. This modified version of Eq. 2.9 is then used to determine the excited-state population for the period after laser excitation by integrating with respect to time:[44]

$$N_2(t) = \chi_s f_B N_T \frac{W_{12}}{r} \cdot (1 - e^{-rt_{laser}}) \cdot e^{-(t - t_{laser})/\tau_{LIF}},\ t > t_{laser} \tag{2.17}$$

This solution assumes that the laser intensity is turned off instantaneously, with an initial condition given by Eq. 2.16, evaluated at $t = t_{laser}$. This solution shows that the population in the excited state decreases exponentially in time after the laser pulse.

The term $\tau_{LIF} = (Q_{21} + A_{21})^{-1}$ in Eq. 2.17 is referred to as the fluorescence lifetime and describes the rate at which the population in a particular excited state transitions to a lower state. As with the derivation of Eq. 2.14, the total number of photons collected via fluorescence over the detection period is determined by multiplying Eqs. 2.16 and 2.17 by the spontaneous emission rate Einstein coefficient A_{21}, accounting for the collection volume and detection system, and integrating with respect to time:[44]

$$S_{LIF} = \chi_s f_B N_T \Phi B_{12} I G t_{laser} \left\{ \left[1 - \frac{1 - e^{-rt_{laser}}}{rt_{laser}} \right] + \left[\frac{\left(1 - e^{-rt_{laser}}\right)}{t_{laser}/\tau_{LIF}} \right] \right\} V \frac{\Omega}{4\pi} \eta \tag{2.18}$$

Like Eq. 2.14, this solution assumes that W_{12} is small compared to A_{21} and Q_{21}. However, if the laser irradiance, I, is sufficiently large such that W_{12} and W_{21} are of the same order of magnitude as Q_{21} and A_{21}, then both must be included in the solution. This gives $r = W_{12} + W_{21} + Q_{21} + A_{21}$ during laser excitation. By defining the irradiance at which the fluorescence signal saturates as[42,44] $I_{sat} = (Q_{21} + A_{21})/(B_{12} + B_{21})$ and rearranging r such that $r = \tau_{LIF}^{-1}[I/I_{sat} + 1]$, a more detailed formulation for the fluorescence signal, including effects from laser saturation, is given as:[44]

$$S_{LIF} = \chi_s f_B N_T \Phi B_{12} \frac{I}{1+I/I_{sat}} G t_{laser} \left\{1 + \frac{1-e^{-rt_{laser}}}{rt_{laser}} \left(\frac{I}{I_{sat}}\right)\right\} V \frac{\Omega}{4\pi} \eta \qquad (2.19)$$

When $I \ll I_{sat}$, Eq. 2.19 simplifies to a form similar to that of Eq. 2.16.

2.3 Multi-Level Fluorescence Modeling

In the preceding discussion, a simplified two-level model of fluorescence was put forth, which provides for an understanding of the most basic physical mechanisms and energy transfer processes involved. This basic description allows for the development of a general analytic relation between the fluorescence signal and these mechanisms and processes. However, such a simple description does not account for rotational or vibrational energy transfer occurring between the absorbing species and the surrounding gas mixture. Since each electronic energy level depicted in Fig. 2.1 can have vibrational and rotational fine structure for molecular species, such energy transfer processes result in a redistribution of the populations to various vibrational and rotational states. To account for these processes, analytical models including multiple energy states and a system of population rate equations are used. Discussion of such modeling aspects can be found in Refs. 42-44.

2.4 Translational Temperature

Translational temperature resulting from the random thermal motion of the absorbing species can be determined by measuring the Doppler-broadened width of the absorption line-shape function of Eq. 2.1. If the temperature, pressure, and mole fractions at a particular location are assumed to be constant, then the Boltzmann fraction and fluorescence yield in Eq. 2.15 at that location are also assumed to be constant. If these assumptions are valid, and if the laser line-shape function is known, then the fluorescence signal will be proportional to the overlap integral at a particular frequency. By scanning the laser's spectral frequency across a particular transition, the absorption line-shape function can be obtained.

Once the absorption line-shape is obtained, the contribution of homogeneous broadening mechanisms to the line-shape must be determined to allow for calculation of the Doppler-broadened line width. Homogeneous broadening can include components from Van der Waals broadening and Stark broadening effects,[58] in addition to collisional pressure-broadening effects. In many cases, the Van der Waals and Stark effects can be ignored, resulting in homogeneous

broadening from pressure alone. If the pressure is known, then the component of the line-shape due to homogeneous broadening can be determined. Alternately, if the pressure is sufficiently low, then collisional pressure broadening can be ignored. A fitting algorithm can then be used to determine the contribution of Doppler broadening to the line-shape. This allows for a more accurate temperature calculation as only one parameter, $\Delta\nu_D$, must be iterated upon to fit the line-shape. The translational temperature, T_{trans}, of the absorbing species can then be obtained by modifying Eq. 2.2:

$$T_{trans} = \frac{m}{8\ln(2)k_B}\left(\frac{c\Delta\nu_D}{\nu_0}\right)^2 \tag{2.20}$$

Both single-photon[58-60] and two-photon[61-65] methods have been used to measure translational temperature. The requirement of scanning a laser's frequency to resolve the Doppler-broadened line-shape can limit the time resolution of the temperature measurement such that only average translation temperatures can be obtained.

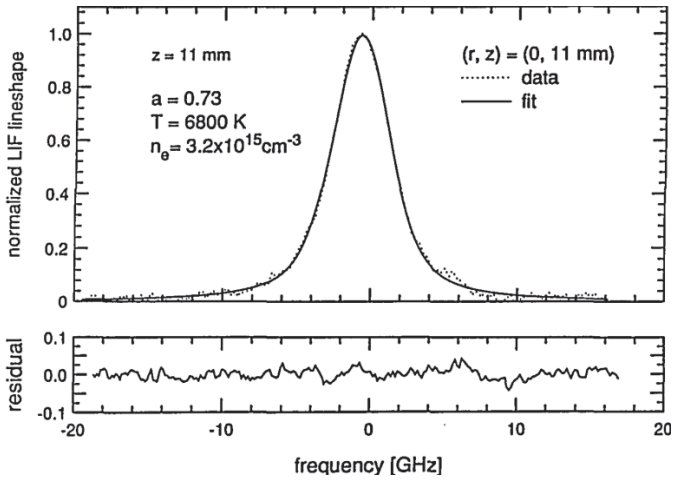

Figure 2.3: Experimental LIF data measured (dotted line, upper plot) in an Argon plasma and corresponding fit of Voigt line-shape (solid line, upper plot) to the experimental data (upper plot) and difference between experimental data and fit (lower plot). Image reprinted from Ref. 58 with permission of the authors and the publisher.

Figure 2.3 shows LIF data (dotted line, upper plot) from Ref. 58 obtained by performing a frequency scan with a semiconductor laser source over an argon metastable transition centered at 810.4 nm. Each frequency scan over the absorption transition took 500 seconds to complete. In the experiment, argon plasma was generated using an inductively-coupled plasma torch. The translation temperature, T, and electron number density, n_e, were obtained by fitting the Voigt line-shape function, which accounted for both Doppler-broadening and several collisional broadening mechanisms, to the experimental LIF data (solid line, upper plot). The lower plot in Fig. 2.3 shows the residual: the difference between the experimental LIF data and the fitted line-shape. An analysis of one of the scans in Ref. 58 gave T_{trans} = 6800±690 K, resulting in a ~10% measurement uncertainty.

2.5 Rotational Temperature

For molecules, the rotational temperature, T_{rot}, can be obtained by exciting two absorption transitions and relating the signal intensities observed from each transition to the rotational temperature through modification of Eq. 2.15. This method was demonstrated in Ref. 66 using a two-photon excitation method to measure rotational temperature at a point in a cold (~300 K)

turbulent flow. For each rotational transition, the population fraction, f_B, is dependent on the rotational energy, F_J, rotational quantum number, J, and rotational temperature, T_{rot}, of the absorbing species. This assumes that excitation occurs in the same vibrational state, v, such that the vibrational energy, G_v, is constant for each probed rotational transition. If χ_s, G, Φ, and t_{det} are assumed to be independent of the rotational state of the absorbing species, then the ratio, R, of fluorescence signals can be simplified to the following relation, similar to that in Refs. 44, 67-70:

$$\frac{S_{LIF,i}}{S_{LIF,j}} = R = C\frac{B_{12,i}E_i}{B_{12,j}E_j}\frac{(2J_i+1)\exp\left[-F_{J,i}/k_BT_{rot}\right]}{(2J_j+1)\exp\left[-F_{J,j}/k_BT_{rot}\right]} \tag{2.21}$$

where the subscripts i and j refer to the particular excited absorption transition, E is the laser energy such that $E = at_{laser}I$, a is the beam cross-sectional area, t_{laser} is the temporal pulse width of the laser, and C is a constant which includes all terms that are independent of the rotational state of the absorbing species. Solving for T_{rot} in Eq. 2.21 yields:

$$T_{rot} = \frac{-\Delta E_{rot}}{k_B \ln\left[CR\frac{B_{12,j}E_j(2J_j+1)}{B_{12,i}E_i(2J_i+1)}\right]} \tag{2.22}$$

Here, $\Delta E_{rot} = (F_{J,i} - F_{J,j})$, and is the difference in energy between the probed rotational levels. To minimize the uncertainty associated with the measured rotational temperature, δT_{rot}, a propagation-of-error analysis can be performed on Eq. 2.21 by computing the derivative of the signal ratio, R, with respect to T_{rot}.[68,71]

$$\frac{\delta T_{rot}}{T_{rot}} = \frac{k_BT_{rot}}{\Delta E_{rot}}\frac{\delta R}{R} \tag{2.23}$$

This analysis suggests that by increasing ΔE_{rot}, and thereby probing two widely separated rotational energy levels, the uncertainty in T_{rot} can be proportionally decreased for a given error in R.[68]

Figure 2.4 shows a mean rotational temperature map of nitric oxide measured in the wake of a 6.35-mm-thick flat plate in a Mach 3 turbulent flow, taken from Ref. 71. The map was obtained by averaging a series of images taken for excitation from rotational levels J = 8.5 and J = 10.5, computing the ratio of the two averaged images, and using a relation similar to that in Eq. 2.22 to compute T_{rot}. In this experiment,

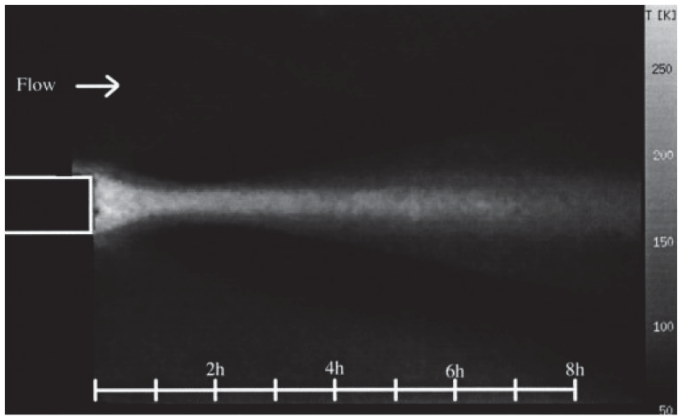

Figure 2.4: Rotational temperature map obtained in the supersonic wake of a flat plate using two-line rotational thermometry. Image reprinted from Ref. 71 with permission from the authors and Springer Science and Business Media.

it was shown that the turbulent nature of the flowfield required excitation of two relatively closely spaced rotational levels (J = 8.5 and 10.5). This requirement arose from the nonlinear relation between R and T_{rot} in Eq. 2.22, which can be heavily influenced by flowfield turbulence.

Figure 2.4 shows a time-averaged temperature measurement obtained using a single laser, which probed the two transitions in separate wind tunnel runs. To obtain instantaneous temperature measurements in a plane using this method, a two-laser, two-camera system can be used, as in Refs. 67-69. In Ref. 68, instantaneous two-line temperature imaging of OH in a shock tube at a nominal pressure of 40.53 kPa and temperature range of 1500-2950 K resulted in temperature measurements with errors of ~20%-25%.

Multi-rotational-line temperature methods also exist and can potentially provide relatively higher sensitivity and dynamic range T_{rot} measurements, particularly at lower temperatures where rotational energy levels are closely spaced.[72] Such methods are appropriate when large variations in T_{rot} are expected, requiring probing of several rotational levels. The rotational temperature is computed by exciting multiple rotational lines and measuring the signal. This measured fluorescence signal, together with the measured laser energy are then substituted into the following relation:[70]

$$\ln\left[\frac{S_{LIF,i}}{B_{12,i}E_i(2J_i+1)}\right] \tag{2.24}$$

A plot of this logarithmic term versus $F_{J,i}$, known as a Boltzmann plot, yields a linear trend with a slope of $-k_B T_{rot}$. Refs. 72-75 used this method to characterize rotational temperatures in arc jet flows. An alternative multi-line approach used in Ref. 76 for measurements in a flame involved fitting a simulated rotational spectrum to experimental data to obtain T_{rot}.

2.6 Vibrational Temperature

The vibrational temperature, T_{vib}, can be measured using an approach similar to that used for rotational temperature. For T_{vib} measurements, a two-line approach can be used. Such an approach is presented in Ref. 77, in which the same rotational levels, $J_i = J_j$, are probed in two different vibrational levels, $v_i \neq v_j$, resulting in nearly constant rotational energies, F_J, but different vibrational energies, G_v. Assuming χ_s, G, Φ, and t_{det} to be independent of the rotational and vibrational levels, the ratio of fluorescence signals, R, can be used to measure vibrational temperature, T_{vib}, in a way analogous to that in Eqs. 2.21 and 2.22.

As with rotational temperature measurements, a multi-vibrational-line temperature measurement method can also be used to infer T_{vib} by modifying the logarithmic term from Eq. 2.24:[70]

$$\ln\left[\frac{S_{LIF,i}}{B_{12,i}E_i(2J_i+1)\exp\left[-F_{J,i}/k_B T_{rot}\right]}\right] \tag{2.25}$$

If the rotational level, J_i, is fixed and the rotational energy, $F_{J,i}$, is kept approximately constant, then the vibrational temperature can be computed independently of rotational temperature.[70] This is done by generating a Boltzmann plot of vibrational energy, $G_{v,i}$, versus this logarithmic term, resulting in a linear relation with a slope equivalent to $-1/(k_B T_{vib})$.

Figure 2.5(a), taken from Ref. 70, shows a Boltzmann plot generated using a relation like that in Eq. 2.25 to infer vibrational temperature. The image data in the experiment was used to measure T_{vib} at a point downstream of a free-piston shock tunnel nozzle on the centerline of the flow. In this experiment, three absorption transitions were selected that had nearly constant rotational energies, F_J, but differing vibrational energies, G_v. In Fig. 5(b), also taken from Ref. 70, the vibrational temperature of NO was observed to be constant with distance downstream of the nozzle, even though the nozzle was conical and the rotational temperature was shown to be decreasing with distance downstream, as the flow expanded. A simple computational model (shown in Fig. 5(b)) was not able to accurately predict the measured vibrational temperature.[70] As shown in Fig. 5(b), T_{vib} = 785±30 K, giving an uncertainty of ~4%.

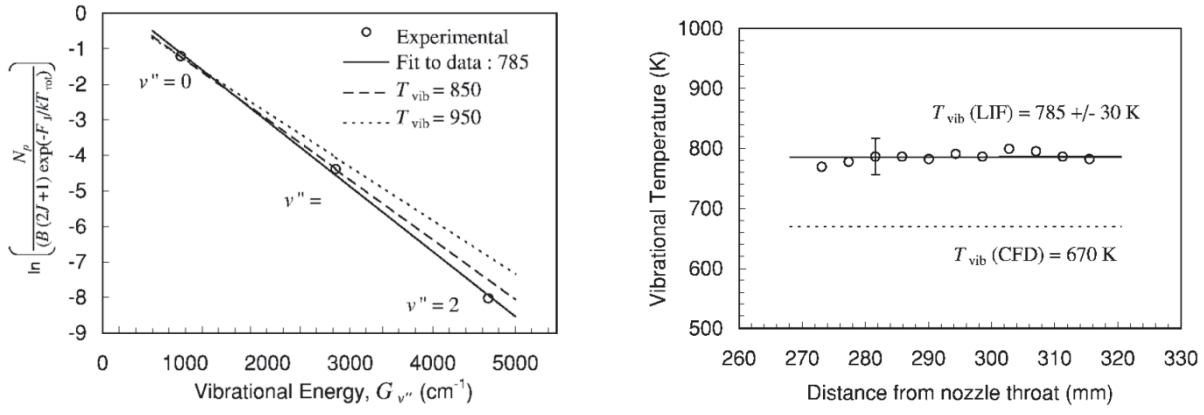

(a) (b)

Figure 2.5: Vibrational temperature measurement obtained by probing multiple vibrational levels and generating (a) a Boltzmann plot and (b) vibrational temperatures plotted as a function of distance downstream. Images taken from Ref. 70 with permission of the authors.

2.7 Species Concentration

Returning to the simplified Eq. 2.14, it is possible to quantify the number density, $\chi_s N_T$, using LIF. However, several factors complicate the interpretation of a LIF signal and its relation to concentration. For instance, Q_{21} in Eq. 2.8 depends on the concentration and temperature of the absorbing species and all other constituent species in the probed mixture. If the temperature of the mixture were unknown, then a separate measurement of temperature would be required to determine both Q_{21} and the temperature-dependent Boltzmann fraction. The measurement system also requires an appropriate absolute intensity calibration to a known reference, which can be further complicated by the collection optics and filters used in such a measurement. The response

of the detection system as a function of S_{LIF} intensity and spectral frequency must also be well understood. The following discussion highlights some of the methods that have been used to provide concentration measurements that address some of these issues.

2.7.1 Saturated LIF

To avoid the complications associated with an unknown quenching rate constant, a relatively high laser irradiance where $I \gg I_{sat}$ can be used to probe the absorbing species.[42] In this instance, the stimulated absorption and emission rates dominate both collisional quenching and spontaneous emission rates; that is, $(W_{12} + W_{21}) \gg (Q_{21} + A_{21})$. The result of this leads to a modified form of Eq. 2.14 where stimulated emission is included and the fluorescence signal is of a form similar to that in Ref. 42:

$$S_{LIF} = \chi_s f_B N_T A_{21} \frac{B_{12}}{B_{12}+B_{21}} t_{det} V \frac{\Omega}{4\pi} \eta \tag{2.26}$$

If A_{21}, B_{12}, and B_{21} are known, then this method can be used to measure concentration if the remaining terms, such as f_B, can be determined. In practice, it is difficult to achieve $I \gg I_{sat}$ because high powered pulsed laser beams are typically Gaussian, both spatially and temporally, so much of the acquired signal can originate from the lower intensity edges of the Gaussian beam, which excite the fluorescence linearly.[42] Further discussion of this method is found in Refs. 42 and 43.

2.7.2 Pre-dissociation LIF

Pre-dissociative fluorescence involves inducing a transition to a level in the excited state, which can then couple to a dissociative state, resulting in dissociation of the molecule into smaller molecules or atoms. Pre-dissociative fluorescence concentration measurements are similar to saturated fluorescence measurements in that the dependence on Q_{21} in Eq. 2.14 can be removed, in this case by exciting the absorbing species to a pre-dissociative state where the pre-dissociation rate, Q_{pre}, is faster than both Q_{21} and A_{21}.[42] A discussion of this mechanism can be found in Refs. 78 and 79 and a general discussion of the method can be found in Refs. 42 and 43. An application of the pre-dissociative technique was presented in Ref. 80 to measure time-averaged OH concentrations in a supersonic hydrogen-air turbulent combusting flow. Concentrations as high as 5.4×10^{16} cm^{-3} with uncertainties of 21% or less were reported.[80]

2.7.3 Short-Pulse LIF

There are two methods of using short laser pulses to quantitatively determine concentration. The first probes the species of interest with a laser pulse having a duration much shorter than the time between collisions with other species. With this method, the concentration can be determined by relating the measured exponential fluorescence decay behavior to the initial signal magnitude during the short-pulse excitation period. While this decay is a function of both A_{21} and Q_{21}, extrapolation of the exponential behavior to initial excitation provides an inferred peak

intensity magnitude, which is assumed to be independent of collisional quenching effects.[43] This independence is assumed since a sufficient number of collisions, required to transfer energy non-radiatively from the excited state, would not yet have occurred. A discussion of this method can be found in Ref. 43. Reference 81 uses a form of this short-pulse method for OH concentration measurements in a turbulent flame.

A second method for measuring concentration involves using a laser pulse that is shorter than or comparable to the fluorescence lifetime but not shorter than the collisional timescales described in Ref. 42. In this approach, the fluorescence lifetime is measured directly, usually using a photomultiplier tube. This short-pulse LIF method can also be used to determine spontaneous emission[82] and collisional quenching[83,84] rate constants when the thermodynamic conditions of the probed mixture are known. Even for unknown conditions, measurement of the fluorescence lifetime allows for the quenching rate to be determined and accounted for. Refs. 85 and 86 use a two-photon LIF technique in which fluorescence lifetime measurements are used to correct for collisional quenching effects in a similar manner. Figure 2.6(a), taken from Ref. 85, shows spectral scans of atomic nitrogen in the NASA Ames Aerodynamic Heating Facility arc jet flow (red data) and laboratory flow reactor (green data). Fluorescence measurements from the flow reactor and a krypton reference cell were used for intensity calibration in order to provide absolute atomic nitrogen number densities. The fluorescence lifetimes observed in the arc jet and flow reactor were used to correct for collisional quenching effects. Figure 2.6(b), also taken from Ref. 85, shows radial atomic nitrogen number density measurements for two air/argon arc jet runs taken 35.6 cm downstream of the nozzle exit. The reported uncertainty in number density was ~12%.[85]

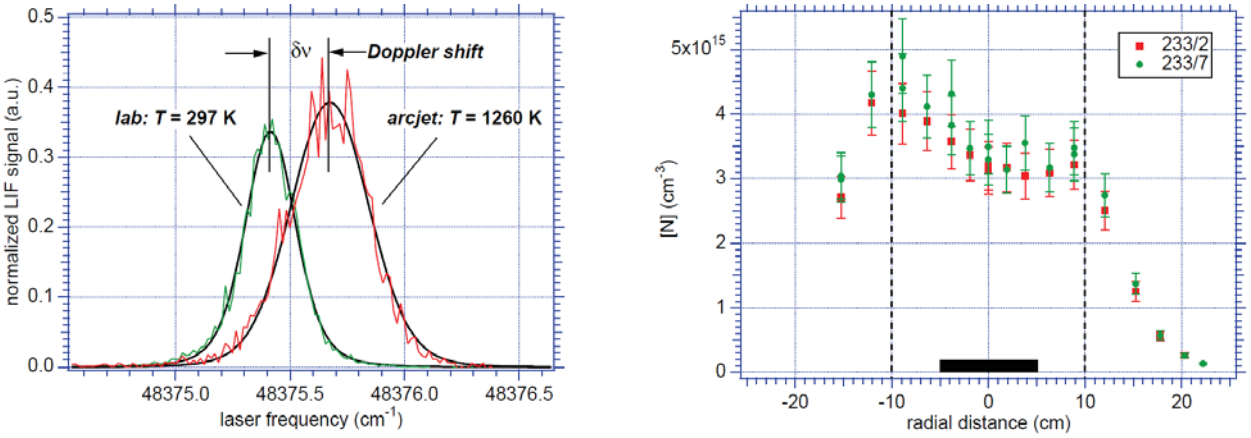

(a) (b)

Figure 2.6: (a) Spectral scans of atomic nitrogen in the NASA Ames Aerodynamic Heating Facility arc jet flow and in a laboratory flow reactor and (b) measured number densities spanning the radial direction of the arc jet 35.6 cm downstream of the nozzle exit. Image taken from Ref. 85 with permission of the authors.

A similar approach is being developed for mole fraction measurements in hypersonic turbulent boundary layers using naphthalene PLIF.[87,88] One benefit of using naphthalene is that it sublimates at slightly elevated temperatures (with respect to room temperature), allowing for the study of scalar transport effects in transitional boundary layers, turbulent boundary layers, and ablating surfaces.

2.7.4 Bi-Directional Beam LIF

If two overlapping, counter-propagating beams are tuned to the same transition, the ratio of fluorescence signals results in the cancellation of all terms in Eq. 2.15 at a point in the flow, with the exception of the spatially dependent laser irradiance. Thus, the spatially varying ratio of fluorescence signals can be equated to the spatially varying ratio of irradiances of the respective beams. The Beer-Lambert law of Eq. 2.5 can then be used to relate irradiance, and therefore fluorescence signals, to number density via the relation:[49]

$$k_s(\nu) = N_s \varphi_s(\nu) \tag{2.27}$$

where $\varphi_s(\nu)$ is the transition cross-section of the absorbing species, describing the absorbing species' interaction with the incident irradiance on a per atom or molecule basis.[45] Combining Eq. 2.27 with Eq. 2.6 allows for a relation between the natural logarithm of the signal ratio and the absorbing species number density to be made:[89]

$$N_s(x) = \frac{1}{2\varphi_{s,0}} \frac{d}{dx} \ln\left[\frac{S_{LIF,1}(x)}{S_{LIF,2}(x)}\right] \tag{2.28}$$

where $S_{LIF,1}(x)$ and $S_{LIF,2}(x)$ are the spatially varying fluorescence signal intensities of the forward- and backward-propagating beams, respectively. In Eq. 2.28, $\varphi_{s,0}$ is the peak transition cross-section, with $\varphi_{s,0} = \varphi_s(\nu_0)$.[45]

This concentration measurement technique was first demonstrated in Ref. 89. The technique only requires that a value for $\varphi_{s,0}$ be known in order to make an absolute concentration measurement of N_s.[89] For total absolute concentration, however, f_B must either be assumed or measured, as from Eq. 2.10, $N_s = \chi_s f_B N_T$. Figure 2.7, taken from Ref. 89, graphically depicts the process of obtaining a concentration of OH in a methane-air flame. In the top plot, the fluorescence intensities are plotted versus position across the flame. The middle plot shows the natural logarithm of the ratio of these two signals with position and the bottom plot shows the calculated absolute OH concentration using Eq. 2.28. Measurements of OH concentration were also made in a plane in Ref. 89 by imaging fluorescence from two counter-propagating laser sheets. Equation 2.28 was applied using each row of pixels to compute signal ratios. Single-shot imaging of a hydrogen/air/oxygen flame allowed for calculation of means and standard deviations of OH concentration. Using 10 images for each laser sheet direction (20 total images), Figure 2.7 of Ref. 89 showed a mean peak OH concentration of ~8.8x10^{14} cm^{-1} with a standard deviation of ~±1.7x10^{14} cm^{-1}, which is ~19.7% of the mean.

2.7.5 Combined LIF/Rayleigh/Raman

In reacting flows, flows undergoing transition-to-turbulence, and turbulent flows, the time-varying nature of flow properties makes it difficult to ascertain concentration. By making simultaneous time-resolved measurements of temperature and major species concentrations, the thermodynamic-dependent parameters in Eq. 2.15 (Boltzmann fraction, overlap integral, and fluorescence yield) can be determined, and a direct relation between concentration and fluorescence signal established. A combined fluorescence, Rayleigh scattering, and Raman scattering measurement technique was used for this purpose in Ref. 90. In that experiment, the Raman scattering was used to measure instantaneous concentrations for major species (O_2, N_2, H_2O, and H_2) in a turbulent hydrogen jet flame. This allowed for the mole fractions of the collision partners, χ_i, in Eq. 2.8 to be calculated. The combined Rayleigh/Raman scattering measurements were then used to measure temperature. The temperature-dependent collisional cross-sections and relative velocity in Eq. 2.8 could then be calculated, and the collisional quenching rate, Q_{21}, determined. The temperature-dependent absorption line-shape and Boltzmann fraction could also be determined from the temperature measurement. The additional measurement of laser energy then provided for a direct relation between NO fluorescence signal and concentration to be established. In Ref. 91, this technique was used to make concentration measurements of CO in turbulent premixed and stratified CH_4/air flames. A stated CO concentration accuracy and precision (single standard deviation) of 10% and 4.5%, respectively, were given.[91]

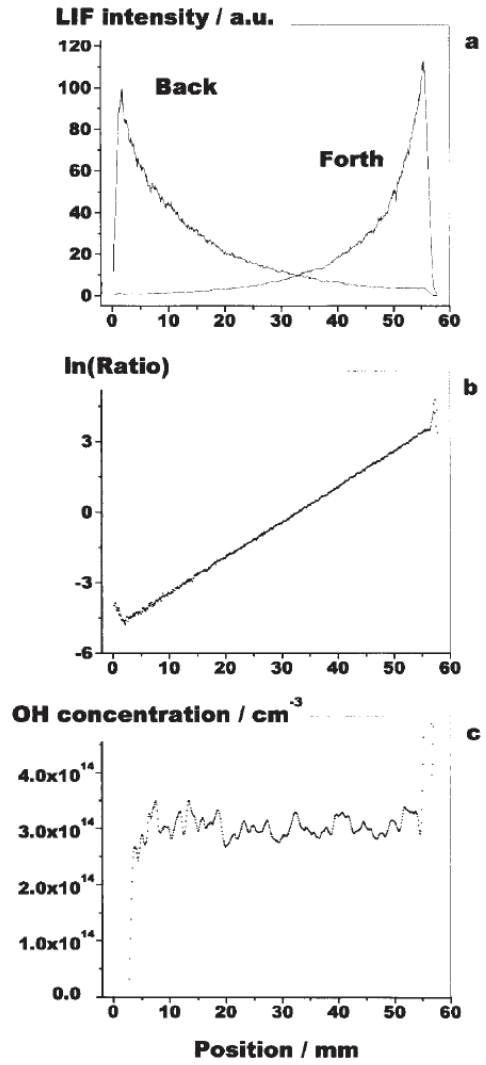

Figure 2.7: Graphical depiction of methodology used to measure concentration using bi-directional beam LIF. Top plot shows spatially varying fluorescence signals, middle plot shows natural logarithm of ratio of these signals, and bottom plot shows OH concentration calculated using Eq. 2.28. Image reprinted from Ref. 89 with permission of the authors and Springer Science and Business Media.

2.8 Doppler-Based Velocimetry

The Doppler Effect can be used to determine flow velocities for atomic and molecular species. The translational motion of the absorbing species in the direction of the excitation laser's propagation, described by a velocity component U, results in a shift of the absorption line-shape function away from its transition center frequency, ν_0, according to:[49]

$$\Delta\nu = \frac{U}{c}\nu_0 \tag{2.29}$$

This velocity-dependent frequency shift of the absorption line-shape function is implicit in the overlap integral, G, and thus, its effect on fluorescence signal can be seen through the dependence of G on the velocity component, U, in Eq. 2.15. When a component of translational motion of the absorbing species opposes the laser's direction of propagation, corresponding to the negative $(-)$ solution of Eq. 2.29, the incident laser radiation appears to be at a higher frequency from the perspective of the gas. Hence, as the laser's frequency is scanned over the absorption transition, Y_ν, the measured intensity of fluorescence corresponding to this profile is shifted toward a lower frequency, or red-shifted. The converse is true when motion is in the same direction as the laser's propagation, corresponding to the positive $(+)$ solution of Eq. 2.29, where the absorption profile is shifted toward a higher frequency, or blue-shifted.

In one implementation, velocity component measurements can be made by scanning the laser over an absorption transition in both the measurement volume and a reference cell. In this case, the Doppler shift between the absorption profiles is used to compute an average velocity according to Eq. 2.29. Examples of such measurements include those in an arcjet,[59,60,64,92] supersonic underexpanded jets,[93-97] shock tunnel,[98,99] and non-reacting supersonic flow with a rearward-facing step.[100-102] Such measurements require that the flowfield be relatively steady since shot-to-shot fluctuations in fluorescence intensity from thermodynamic and fluid dynamic variations can affect the measured line-shape. The velocity measurements can also be complicated by a frequency shift in the line-shape function resulting from collisional effects (pressure). In compressible flows, the pressure field can vary significantly, and hence the collisional shift in the line-shape function can likewise vary. Absorption of laser energy can also result in an apparent frequency shift in the line-shape function. Recall that the line-shape

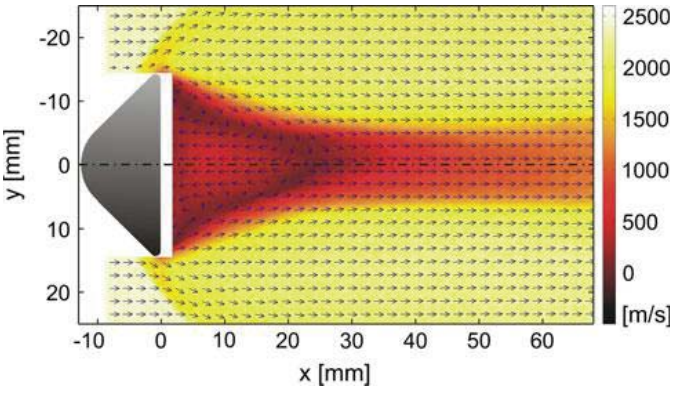

Figure 2.8: Two-component velocity measurement using fluorescence-based Doppler velocimetry technique. Vectors denote flow direction and color map represents magnitude. Image reprinted from Ref. 99 with permission of the authors and Springer Science and Business Media.

function must be inferred from the overlap integral, G, which represents the convolution of the absorption line-shape and laser spectral line-shape. If absorption is significant, then irradiance will vary spatially according to Eq. 2.6, resulting in a spatially varying overlap integral. An analysis of how absorption affects the line-shape frequency shift is presented in Ref. 99. If flow symmetry is assumed, then the frequency shift due to pressure can be estimated.[98] Flow symmetry can also be used in the application of Eq. 2.6 to correct for the frequency shift resulting from absorption.[60] Alternatively, if two counter-propagating laser beams are used, these frequency shift effects can be completely removed. The use of counter-propagating beams results in two excitation peaks, separated in frequency by twice the velocity-induced Doppler shift. The need for a reference cell measurement to ascertain velocity can also be removed, as a counter-propagating beam approach is self-referencing.[95,103,104]

Figure 2.8 in Ref. 99 shows a two-component velocity measurement about a heat shield model taken in a hypersonic free-piston shock tunnel. In this experiment, laser sheets were directed in both the radial (vertical) and axial (horizontal) directions so that measurements of the Doppler-shifted absorption profiles for the respective directions could be obtained and compared with measurements from a static reference cell to infer velocities. An estimation of velocity errors incurred from the frequency shifts due to absorption and collisional effects was also performed. In Ref. 99, three separate absorption transitions were probed to measure two different velocity components, with one transition being used for both components. This resulted in a measured axial freestream velocity of 2394±68 m/s and a measured radial velocity of 53±50 m/s, giving respective uncertainties of ~2.8% and ~94.3%.[99]

Another form of the fluorescence-based Doppler velocity measurement is a fixed frequency method, which can allow for an instantaneous velocity component measurement. With the fixed frequency technique, a narrow linewidth laser is tuned off the absorption profile peak to a point where the slope of the profile is maximum, as described in Refs. 105 and 106. Assuming that the absorption profile is approximately linear in the region of maximum slope, the measured signal intensity can be related to the Doppler shift of the profile. This fixed frequency Doppler velocimetry technique has been applied to a free jet,[107] supersonic underexpanded jet,[108] and reacting supersonic flow.[109] The stated random and systematic errors in Ref. 108, when added in quadrature, gave a total uncertainty of ~12%. In Ref. 109, the stated lowest time-averaged and single-shot uncertainties achieved were ~3% and ~15%, respectively, for a 1600 m/s velocity range.

2.9 Flow-Tagging Velocimetry

Another technique by which velocity can be measured using fluorescence is flow-tagging velocimetry. Fluorescence-based flow-tagging velocimetry is a time-of-flight technique that involves laser excitation—or tagging—of the gas along a line, series of lines, or grid pattern. With this form of velocimetry, the species of interest in the gas absorbs the incident radiation from a laser source, which induces either of the following: 1) fluorescence, 2) a reaction that

forms a product that then emits a photon via fluorescence, or 3) a reaction that forms a product that can then be probed with another laser source to induce fluorescence. Images of the fluorescence pattern are acquired at two time delays, with velocity computed by measuring the displacement of the tagged molecules between images. Typically, a line or series of lines can be used to measure a single-component of velocity while a crossed grid pattern can be used to measure two-components. Two general fluorescence-based methods of flow-tagging velocimetry are discussed here; one that requires a single laser source and another that requires multiple laser sources. The main advantage of flow-tagging velocimetry, as compared to most Doppler-based methods (which are time averaged), is that it can make instantaneous (single-shot) measurements with fast time resolutions (as short as a few hundred nanoseconds). A disadvantage, however, is that flow-tagging velocimetry cannot provide full velocity field information. A broader discussion of molecular-tagging velocimetry, which relies on molecular tracers for flow-tagging, is provided in Ref. 110.

2.9.1 Single-laser methods

The first method involves either direct or indirect excitation of fluorescence with a single laser source. The first application of this method to a gaseous flow involved excitation of phosphorescence of biacetyl molecules, as described in Ref. 111. If this method is used, the fluorescence lifetime of the tagged molecules must be long enough so that advection provides for measurable displacements with tagged regions having signal intensities that are still above the detection limit of the imaging system at the time the second image is acquired. Typical experiments involve capturing a reference image acquired during the tagging process, or a relatively short time thereafter. If a single-framing camera is used, such as in Ref. 112, a single reference image or set of reference images is acquired. The timing of the single-frame camera is then delayed and a subsequent image or set of images is then acquired. If a two-camera system or dual-framing camera is used, such as in Ref. 113, the delayed image is acquired in sequence after the reference image. The velocity is computed by measuring the displacement of the tagged molecules that occurs in the time between when the reference and delayed images were acquired. The form of this technique relying on direct excitation of fluorescence for flow tagging has been applied to the study of supersonic jets,[114-120] hypersonic boundary layers,[112,113,121,122] and arcjet flowfields.[60]

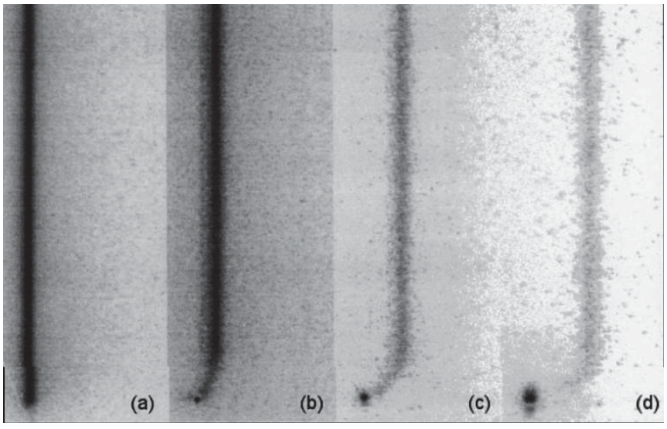

Figure 2.9: Single-line excitation of nitric oxide fluorescence used to study hypersonic boundary layer flow over a flat plate. Images, from left to right, correspond to camera delay settings of 0 ns, 250 ns, 500 ns, and 750 ns. Image reprinted from Ref. 112 with permission of the authors.

Figure 2.9, taken from Ref. 112, shows images from tagging a single line of nitric oxide using direct excitation of fluorescence within a flat plate hypersonic laminar boundary layer. In this Figure, the left-most image corresponds to the reference image, while the remaining images, from left to right, correspond to delayed images taken at 250 ns, 500 ns, and 750 ns after tagging, respectively. Measurements of freestream velocity, spatially averaged from a point just above the velocity boundary layer (3 mm) to 15 mm above the flat plate, resulted in a mean of 3,035±100 m/s at 90% confidence, giving an uncertainty of 3.3% of the mean.[112] Single-shot uncertainty estimates for a 3,000 m/s freestream flow and for camera delay settings of 250 ns, 500 ns, and 750 ns were 4.6%, 3.5%, and 3.5%, respectively.[112]

An indirect excitation scheme, as described in Refs. 123-125, relies on photodissociation of molecular nitrogen for flow tagging. The technique uses a femtosecond laser pulse to dissociate molecular nitrogen into two nitrogen atoms, which then recombine after a collision, forming molecular nitrogen in an intermediate state. A subsequent collision brings the molecular nitrogen to an excited electronic B state, which then emits a photon via fluorescence upon transitioning to the excited electronic A state. Ref. 125 provides a description of this process. One benefit of this indirect technique, known as Femtosecond Laser Electronic Excitation Tagging (FLEET), is that the recombination rate of dissociated atomic nitrogen allows for a much longer fluorescence lifetime. This would allow displacements to be measured over greater time scales, providing for accurate measurements of velocity in low-speed flow regions, such as in a hypersonic wake flow. Additionally, the technique relies on molecular nitrogen for tagging, which is present in most hypersonic facilities.

2.9.2 Multi-laser methods

A second method of fluorescence-based flow-tagging velocimetry involves writing a line, series of lines, or grid pattern into the flowfield by one of several laser-based mechanisms. This pattern can then be interrogated, or read, by subsequent laser pulses to induce fluorescence, allowing for the determination of velocity through measurement of the displacement of the pattern. Such techniques usually involve two or three different lasers and are therefore more time consuming to set up and more difficult to execute.

One mechanism by which a pattern can be written into the flowfield is via ionization of the absorbing species, known as Laser Enhanced Ionization (LEI) flow tagging. The tagging process is accomplished by promoting the species (such as sodium in Refs. 126-128) to a higher energy state via laser excitation near the ionization limit. Collisions then result in the ionization of the species, with the tagging pattern corresponding to the ionized regions. Subsequent laser pulses are used to induce fluorescence of the absorbing species in regions that have not been photo-ionized. Supersonic measurements of velocity in a shock tube were performed using LEI flow-tagging in Refs. 126 and 127, and hypersonic velocity measurements in an expansion tube were performed in Ref. 128.

A second mechanism that can be used to write a pattern into the flowfield is by vibrational excitation of molecular oxygen via Raman pumping. This is followed by reading the pattern of the vibrationally-excited oxygen by inducing fluorescence. The technique, known as Raman Excitation and Laser-Induced Electronic Fluorescence (RELIEF),[129] is advantageous as it relies on the flow-tagging of oxygen which is a common working gas of most hypersonic facilities. This technique has been used to characterize turbulence in a free jet[130] and underexpanded jet.[131] The RELIEF technique, however, is limited to temperatures below 750 K. Above this temperature, a significant fraction of oxygen molecules are vibrationally excited, making it difficult to distinguish the tagged molecules from the background.[132]

Yet another mechanism involves using one laser to photo-dissociate a molecular species. This results in the formation of a product species for which a second laser can be used to read the location of the written pattern by exciting laser-induced fluorescence in the product species. The formation of the product species typically occurs through one or more reactions. A list of partner species used in the writing and reading process include: H_2O-OH,[133-139] N_2O-NO,[140] O_2-O_3,[141,142] N_2/O_2-NO,[143-146] and NO_2-NO.[116,147-154]

Figures 10(a) and 10(b), taken from Ref. 151, show images of vibrationally excited NO fluorescence in a grid pattern formed via photodissociation of NO_2 in a mixture containing 6.3% NO_2 in N_2. The images were taken in a supersonic underexpanded jet 400 ns (Fig. 2.10(a)) and 800 ns (Fig. 2.10b) after the pattern was written into the flow with a two-dimensional array of 355 nm beams. Two components of velocity were obtained by relating the displacement of the grid in the left image to a grid imaged in a stationary gas. The upper half of Fig. 2.10(c), taken from Ref. 151, shows measured streamwise velocities compared with computation, shown in the lower half of Fig. 2.10(c). The use of two pulsed dye lasers in this experiment permitted the excitation of both a low (J = 1.5) and high (J = 8.5) rotational level within the same vibrationally excited (v = 1) NO state. The fluorescence images corresponding to the low-J (Fig. 2.10(a)) and high-J (Fig. 2.10(b)) rotational levels also allowed for measurement of the rotational temperature by using a calculation similar to that presented in Eq. 2.22. The top half of Fig. 2.10(d), from

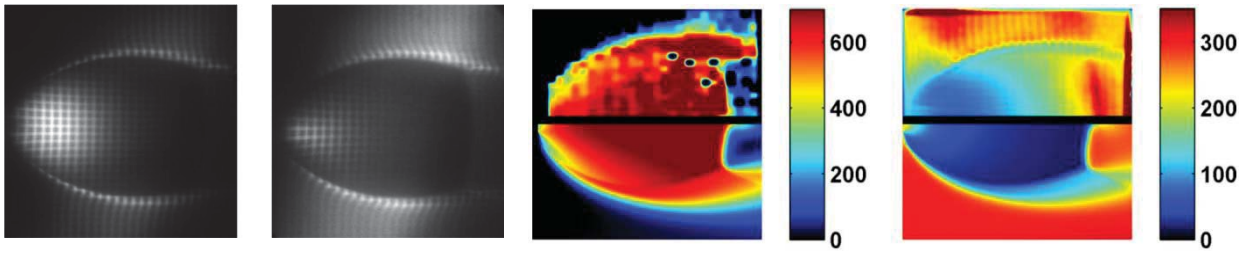

(a) (b) (c) (d)

Figure 2.10: Flow-tagging images of vibrationally excited NO fluorescence obtained (a) 400 ns and (b) 800 ns after photodissociation of NO_2. The two-dimensional grid pattern allows for calculation of two velocity components. Measured (c, top) and computed (c, bottom) streamwise velocity maps. Measured (d, top) and computed (d, bottom) rotational temperature map. Image reprinted from Ref. 151 with permission of the authors and the publisher.

Ref. 151, shows measured rotational temperature compared with computation, shown in the lower half of Fig. 2.10(d). Stated root-mean-square (RMS) uncertainties in the velocity measurement were ~5% with high signal-to-noise.[151] The stated RMS uncertainties in rotational temperature ranged from 9% to 35% prior to the Mach disk.[151]

NO_2-NO flow tagging velocimetry has also been used to study boundary layer transition on a flat plate in a Mach 10 wind tunnel.[153,154] Pure NO_2 was seeded into the boundary layer through a spanwise slot located downstream of the sharp leading edge. The angle of attack of the flat plate was 20 degrees, reducing the edge Mach number to about 4.2. Parallel focused beams of 355 nm light oriented normal to the surface of the flat plate (and in a plane parallel with the streamwise direction of the flow) dissociated the NO_2, creating NO. After a 40 ns delay, the NO was probed by a 226 nm laser, at which time the camera acquired an image. One microsecond later, a second 226 nm laser probed the NO and the second image was acquired with the same camera. The two images were compared to compute velocity profiles. Figure 2.11 shows the resulting velocity profiles for two cases, one with no trip (i.e. tripping element, a protuberance designed to trip the flow from laminar to turbulent) and one with a 1-mm tall cylindrical trip, where the measurements were made downstream of, and on the centerline of, the trip. (The laminar boundary layer thickness was also approximately 1 mm thick.) The figure shows mean profiles (black, top two charts) as well as profiles of the fluctuating component of velocity, u' (red, bottom two charts). For the case of no trip, the velocity profiles compare well with a compressible Blasius solution (shown in light grey). When the trip is present, the measured mean profiles depart from the laminar solution, showing a profile that is more full than the laminar profile near the plate surface with a pronounced velocity deficit near the edge of the profile. The fluctuating streamwise velocity increases by a factor of three, up to 250 m/s, between the two cases, with the fluctuations highest in the wake of the trip. The single-shot measurement precision was 15-25 m/s, which was 1-2% of the maximum velocity in the boundary layer. The accuracy was estimated to be 5-15 m/s.[153]

2.10 Advantages and Limitations of Laser-induced Fluorescence

The time scales associated with inducing fluorescence via laser excitation are typically a few hundred nanoseconds, which is much shorter than hypersonic flow time scales, therefore providing sufficient temporal resolution for high-speed transition-to-turbulence measurements. The availability of pulsed lasers capable of picosecond and femtosecond excitation allow for fluorescence measurements with time scales much less than those associated with collision and reaction time scales. Recently developed kHz- and MHz-rate pulsed laser systems have allowed image sequences consisting of tens to thousands[155] of images to be acquired, providing time-resolved information pertaining to high-speed fluid dynamic behavior. Both fluorescence-based velocimetry[150] and visualization[156, 157] experiments in hypersonic flow fields have been performed with these types of laser systems. The spatial resolution of a LIF technique is also sufficient for many applications, and higher than other techniques such as Raman or CARS, with laser sheet thicknesses typically in the range of 0.1 to 1 mm and magnifications of tens of pixels

per mm, depending on the experimental setup. Fluorescence-based measurements are more sensitive than other techniques (for example Raman spectroscopy) with sensitivity on the order of parts-per-million or better.[42]

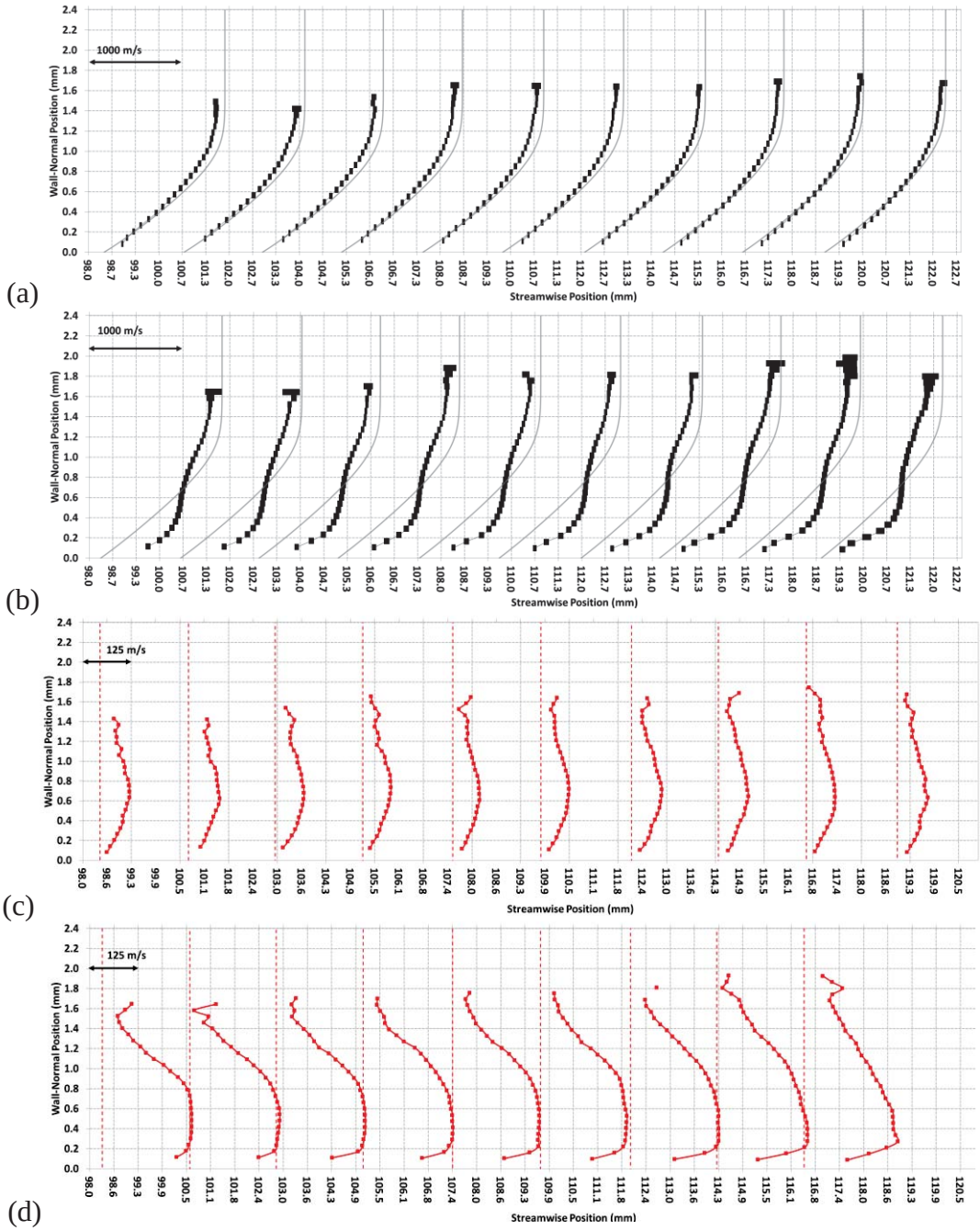

Figure 2.11: Streamwise velocity profiles on a flat plate in a Mach 10 facility for the case of no trip (a) and a k = 1 mm tall, 4 mm diameter cylinder trip (b) and the fluctuating streamwise velocity for no trip (c) and a k = 1 mm tall, 4 mm diameter cylinder trip (d). Images reprinted from Ref. 154 with permission of the authors.

Additionally, a wide range of species including intermediate combustion species can be probed using fluorescence techniques. Reference 43 provides an extensive listing of many species that have been detected using LIF and other methods. Another advantage of LIF is that it is readily extended to planar or volumetric measurement (see Refs. 158 and 159).

Several factors complicate acquisition and interpretation of LIF signals, complicating quantitative measurements. Quenching of the fluorescence, which prevents easy quantification of signal intensities, was discussed extensively above. Absorption of laser energy as the laser light passes through the flowfield can limit the effectiveness of fluorescence-based measurements, as the energy will decrease in an exponential manner over a given spatial path length according to the Beer-Lambert relations in Eqs. 2.5 and 2.6. This makes quantitative measurements difficult, as the laser energy at a particular location may not be easily determined. Absorption can be significant when the concentration of the absorbing ground state population is high, the transition cross-section is relatively large, the Einstein B coefficient for stimulated absorption is relatively large, and/or the path length through which the laser radiation passes is relatively long. To avoid strong absorption, a transition may be selected for which the population is small based on analysis of the Boltzmann fraction, as was done for PLIF visualization measurements in a hypersonic shock tunnel described in Ref. 160. Absorption can also limit measurement capabilities when fluorescence from the probed volume is re-absorbed by the species of interest. This effect, known as *radiative trapping*, occurs when fluorescence emission at frequencies readily absorbed by highly populated states must pass through gas containing these potential absorbers before reaching the imaging system. Measurements in a non-uniform or turbulent mixture are especially susceptible to errors associated with absorption and radiative trapping effects, as the absorption coefficient is a spatially- and temporally-varying property. A discussion of these issues, and some methods used to circumvent them, is provided in Ref. 42.

Another disadvantage of LIF is that it usually probes only a single species at a time, compared to Raman or CARS, which can interrogate many species simultaneously. However, the fact that PLIF can measure spatial distributions of species can compensate for the single-species capability in some applications.

Consideration must also be given to the optical access of the test facility. Since much of the work described in this discussion requires fluorescence excitation using laser frequencies in the UV portion of the electromagnetic spectrum, the window material used in hypersonic facilities must be capable of transmitting such frequencies with minimal absorption. Also, typically two or three windows are required for LIF or PLIF applications. The laser (beam or sheet) is typically brought in from one window and observed through another window at right angles to the first window. A third window can allow the laser to leave the test section, reducing scattered light, and allowing the quantification of absorption of the laser beam/sheet in some applications. These windows are typically relatively large compared to those required for CARS or diode laser absorption measurements. When short-pulse LIF experiments are performed, the inverse relationship between the pulse temporal width and spectral width (which for a Gaussian pulse is

$\tau_{laser} = 0.44/\Delta\nu)$[45] can result in distortion of the temporal characteristics of the pulse. This is because the refractive properties of the optical windows of the test facility affect the speed with which the frequency components of the short pulse pass through the window material. Reference 45 discusses issues related to short pulse excitation and interaction with optical components.

3. Rayleigh and Raman Scattering

3.1 Introduction

When a light beam passes through a gaseous medium, it can interact with the gas molecules or particles in the gas, thereby scattering light away from the path of the incident beam. *Elastic* scattering occurs if no energy is gained or lost to the medium. If energy is either absorbed or lost by the medium, the scattering is *inelastic*. Light scatter from particles that have a diameter, *d*, on the order of or larger than the light wavelength, λ, is termed Mie scattering. Scattering for which $d << \lambda$ is known as *spontaneous Rayleigh scattering* if elastic and *spontaneous Raman scattering* if inelastic. These processes are shown schematically in Figs. 3.1 and 3.2. Represented on the energy level diagram in Fig. 3.1, a photon excites a molecule from an originating state, 1, to a 'virtual' state, 2, from which the scattered photon is emitted. The virtual state, represented by a dashed line, is not an actual resonant state of the molecule. Instead, it indicates a non-resonant, short-lived state in which the electron distribution of the molecule is distorted. This virtual state immediately relaxes to the originating state (in the case of Rayleigh scattering) or another state (in the case of Raman scattering). Relaxation to a higher lying (e.g. vibrational) state than the originating state is termed *Stokes Raman* scattering. In this case, the molecule absorbs a quantum of energy through this process. In *anti-Stokes Raman* scattering the molecule imparts a quantum of energy to the scattered photon so that the scattered photon has higher energy than the incident photon. In this case, the originating state must not have been a ground state.

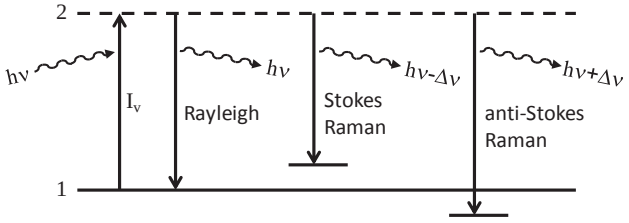

Figure 3.1. Energy level diagram indicating incident radiation, Rayleigh scattering and Raman scattering.

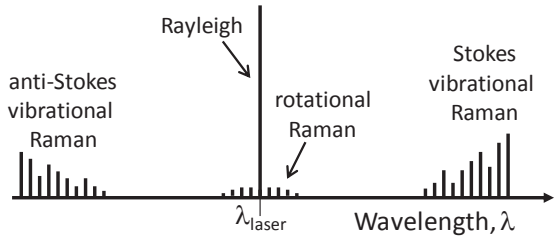

Figure 3.2. Notional Raman/Rayleigh spectra.

Figure 3.2 shows notional Raman/Rayleigh spectra, not drawn to scale. Rayleigh scattering is shown at the laser's wavelength. Discrete pure rotational Raman lines, associated with rotational quanta imparted to or subtracted from the incident laser frequency, are shown on opposite sides of the Rayleigh peak. Vibrational Raman bands are located further away, spectrally shifted towards the red (Stokes) and the blue (anti-Stokes). The vibrational Raman bands show rotational fine structure. Raman scattering is much

weaker than Rayleigh scattering. Raman scattering is typically three orders of magnitude smaller than Rayleigh scattering for most gases of interest to supersonic and hypersonic flows.[42]

3.2 Theory of spontaneous Rayleigh and Raman scattering

Comprehensive reviews of the theory and application of Rayleigh and Raman scattering have been given by others.[42,43,161,162] Herein we provide a brief introduction and overview. Later sections will show how this theory is applied to measure thermodynamic properties. An electromagnetic wave incident upon a molecule perturbs the molecule's electron cloud, making it oscillate at the same frequency as the incident wave. These oscillations cause a periodic charge separation within the molecule, known as an induced dipole moment. Oscillating dipole moments act like antennas, emitting radiation. As described in more detail by Baldwin,[163] if these oscillations are in-phase, the emission adds constructively, producing a coherent beam. If out-of-phase (for example, in the direction orthogonal to the beam), the emitted light interferes destructively and the radiation cancels. For a monochromatic plane wave passing through a gas, the constructive interference occurs only in the forward direction. The resulting emitted coherent light is perfectly in-phase with and indistinguishable from the incident wave. In a gas composed of a finite number of molecules, the destructive interference at other angles is not fully complete because of statistical variations in the number of particles located in different wavelength-sized volumes of the gas.163,[164] That is, there are not exactly the same number of particles in each wavelength sized volume, which would be required to cancel out the radiation perfectly. This statistical variation in the number density then leads to Rayleigh and Raman scattering. Rayleigh and Raman increase significantly in intensity at shorter wavelengths: both scale approximately as $1/\lambda^4$.[42]

The radiant intensity, I^{Ω}, which is the scattered power per unit solid angle, is proportional to the square of the induced dipole moment. The induced dipole moment, $\vec{p}$, is given by:[42]

$$\vec{p} = \varepsilon_0 \alpha \vec{E} \tag{3.1}$$

where ε_0 is the permittivity of free space, α is the molecular polarizability and $\vec{E}$ is the incident electric field given by $\vec{E} = \overrightarrow{E_0}\cos(\omega_0 t)$, where $\overrightarrow{E_0}$ is the amplitude of the electric field, ω_0 is the frequency of the laser light and t is time.

The polarizability of a molecule depends on its internal structure and varies with time during vibrational oscillations at the natural frequency of the molecule, ω_v, vibrating in the direction of its normal spatial coordinate, Q. The polarizability can be approximated with a Taylor series expansion:

$$\alpha = \alpha_0 + \left(\frac{\partial \alpha}{\partial Q}\right)_0 dQ \tag{3.2}$$

where the small physical displacement, dQ, of the atoms about their equilibrium positions (denoted by the subscript 0) during vibrations is:

$$dQ = Q_0 \cos(\omega_v t) \tag{3.3}$$

Combining Eqs. (3.1)-(3.3):

$$\vec{p} = \left[\alpha_0 + \left(\frac{\partial \alpha}{\partial Q}\right)_0 Q_0 \cos(\omega_v t)\right] \varepsilon_0 \overrightarrow{E_0} \cos(\omega_0 t) \tag{3.4}$$

Expanding and using a trigonometric identity: [42]

$$\vec{p} = \alpha_0 \varepsilon_0 \overrightarrow{E_0} \cos(\omega_0 t) + \tfrac{1}{2}\left(\frac{\partial \alpha}{\partial Q}\right)_0 \varepsilon_0 Q_0 \overrightarrow{E_0}[\cos(\omega_0 - \omega_v)t + \cos(\omega_0 + \omega_v)t] \tag{3.5}$$

The first term on the right side of Eq. (3.5) describes Rayleigh scattering at a frequency corresponding to the incident laser's wavelength. The second term indicates Raman scattering which is shifted from the Rayleigh scattering by $\pm\omega_v$ resulting in upshifted (anti-Stokes) and downshifted (Stokes) Raman scattering. While significant theory has been developed to describe the physics of Raman and Rayleigh scattering, the strengths of the scattering for different gases is generally measured and reported as a temperature-independent differential cross section: [42]

$$\left(\frac{\partial \sigma}{\partial \Omega}\right)_{zz} \equiv \frac{I_{zz}^{\Omega}}{NI} \tag{3.6}$$

which can be rearranged as:

$$I_{zz}^{\Omega} = \left(\frac{\partial \sigma}{\partial \Omega}\right)_{zz} NI \tag{3.7}$$

where the subscript *zz* refers to a polarization in the z (vertical) direction caused by an incident electric field oriented in the *z* direction, *N* is the number density of the gas and *I* is the laser irradiance. [42] The differential cross sections vary by process (Rayleigh vs. Raman), by molecule, and vary with the laser wavelength but are independent of pressure and temperature.

Rayleigh scattering from different molecules cannot be distinguished spectrally, so it is not usually used to detect individual species. Under circumstances where the composition is fixed or known, or limited to vary under controlled conditions,[165,166] Rayleigh scattering can be used to measure the gas density, ρ. As discussed further below, the Rayleigh scattering cross section varies from molecule to molecule, with some hydrocarbon species having cross sections more than an order of magnitude larger than N_2. The cross section for a mixture of gases is equal to the mole-fraction-weighted average of the individual cross sections. If the composition can be estimated or measured, for example by Raman scattering,[167] then the effective cross section for the gas mixture can be determined, allowing the density to be determined from the measured Rayleigh scattering. Under conditions where the pressure and composition are known or can be determined and where the perfect gas law applies, the gas temperature can be inferred from the

measured density.[42] Such measurements can suffer from interference from Mie scattering from particles and laser scattered light.[42] To avoid Mie interferences, the gases can be filtered to remove particles. Careful experimental design and blackening of surfaces can minimize scattered laser light.

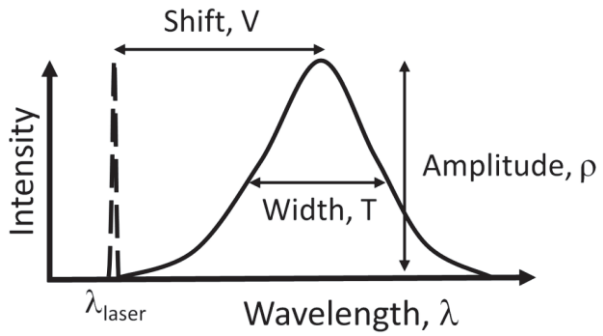

Figure 3.3. Notional sketch of spectrally dispersed Rayleigh scattered light (solid line) which has been Doppler shifted from the incident laser light (dashed).

Spectral analysis of Rayleigh scattering yields additional parameters that can be measured. Figure 3.3 shows a schematic of the dispersed Rayleigh scattered light (solid line), separated from the incident laser light (dashed line). The spectral shift of the Rayleigh from the laser is caused by the Doppler shift of the gas relative to the incident light beam and depends on the detection angle. The width of the Rayleigh spectrum depends, in part, on the gas temperature. The amplitude of the scattering, as described above, depends on the gas density (and composition). Thus, in principle, by spectrally dispersing the Rayleigh scattered light, the temperature, velocity and density of a gas can be measured simultaneously. These effects are detailed below with examples given.

Revisiting Eq. (3.5), notice that for Raman scattering to occur, $\left(\frac{\partial \alpha}{\partial Q}\right)_0$ must be nonzero. This happens when a molecule exhibits a *change* in its polarizability with vibrational displacement. For example, as the atoms in the N_2 molecule vibrate, they become less polarizable as the atoms approach each other (charges exhibiting more force because they are closer to each other) and more polarizable when further apart (charges more weakly interacting). This results in a nonzero $\left(\frac{\partial \alpha}{\partial Q}\right)_0$. Such vibrations are *Raman active.* On the other hand, some vibrational modes do not change the molecule's polarizability, for example the asymmetric stretch of CO_2 has the following vibration pattern: O→ ← C O→. Such modes have $\left(\frac{\partial \alpha}{\partial Q}\right)_0 = 0$ and are termed *Raman inactive.* Further quantum mechanical selection rules and molecular structure considerations (atomic mass, bond length, moment of inertia, etc.) determine the shape and structure of the Raman spectra. [42] Since the frequency of Raman spectra depend strongly on the individual species' molecular structure (each vibrational resonance occurring at a different energy), Raman spectra from different molecules appear spectrally separated when they are dispersed, typically using a grating-based spectrometer equipped with a camera to acquire the spectra. Because Raman scattering is species-specific, it can be used to measure individual species concentrations, where in Eq. (3.6), *N* is the species being detected and the differential cross section is that of the individual species.

3.3 Advantages and Disadvantaged of Rayleigh and Raman Scattering

Rayleigh and Raman scattering have many inherent advantages compared to other measurement techniques. Both use just a single laser and the laser need not be resonant with any particular molecular resonance as in absorption or laser induced fluorescence (LIF). This allows high-powered, fixed frequency lasers to be used for Rayleigh or Raman. Since they are linear laser techniques involving only a single excitation beam, Raman and Rayleigh are relatively easy to set up and understand, and the data are, in general, easier to analyze than nonlinear techniques like coherent anti-Stokes Raman spectroscopy (CARS). Neither Raman nor Rayleigh is sensitive to collisional quenching, a phenomenon which complicates the interpretation of LIF signals. Absolute intensity calibration of both techniques is relatively straight forward and easily performed. Raman and Rayleigh can be performed simultaneously using the same laser to measure species concentrations (Raman), temperature (Raman and/or Rayleigh), density (Raman and/or Rayleigh) and velocity (Rayleigh).

The major disadvantage of Raman and Rayleigh scattering is the low signal intensity. The low signal from Raman scattering generally prevents minor species (less than a few percent by mole fraction) from being detected using this technique. Because the signals are so low, large (low *f*-number) collection optics are usually used. Ideally, the detection optics need to be placed close to the measurement region and, in ducted flows, large windows are required. Hypersonic and combusting flows can sometimes be luminous. Natural luminosity, like spontaneous Rayleigh and Raman scattering, emits light in all directions. In order to improve the signal-to-noise ratio, temporal, spatial, and spectral filtering can be used to collect the desired radiation and block unwanted natural luminosity. For example, gated detection of pulsed signals (or lock-in detection of continuous signals) can be used.

3.4 Translational Temperature, Velocity, and Density Measurements

The gas temperature and velocity can be determined from the Rayleigh spectrum by resolving the Doppler broadening and Doppler shift, respectively. The Rayleigh scattering linewidth is typically in the range of 1-6 GHz (0.03-0.17 cm^{-1}) for supersonic and hypersonic flow experiments in the range of a few hundred to a few thousand kelvins, depending on the temperature and angle of incidence of detection and collection of the light (see Ref. 161 for detailed information about the Rayleigh scattering lineshape and angular dependence). A high-resolution laser can be used so that the broadening caused by the laser's lineshape is negligible compared to this Doppler broadening. For example, injection seeded, pulsed Nd:YAG lasers typically have linewidths of about 0.1 GHz (0.004 cm^{-1}) while continuous sources can have linewidths that are orders of magnitude smaller. To spectrally resolve Rayleigh scattering, a high-spectral-resolution instrument is required. Two methods are typically used: gas vapor cells and Fabry-Perot etalons.

A gaseous cell filled with iodine vapor can be used in combination with excitation in the visible wavelength range, where I_2 has many absorption lines, by placing a low-pressure gas cell containing crystalline iodine and I_2 vapor in front of a detector or camera. The diameter of the cell should be larger than the diameter of the collection lens. The cell length, pressure and temperature of the I_2 cell are chosen to control the I_2 gas concentration and spectral line shape and therefore the absorption magnitude and profile. Attenuation of transmitted light by a factor of 10^5 can be achieved using high-resolution cw lasers, though it is more difficult to achieve attenuations greater than ~10^3 with off-the-shelf injection-seeded, pulsed Nd:YAG lasers.[168] The absorptions can be used to reject spurious scattered laser light, while passing the pressure- and Doppler-broadened and Doppler-shifted Rayleigh scattering, allowing background-scatter-free density measurements. These sharp absorption features can also be used for temperature and velocity measurements by using the steep edge of the absorption spectral profile to provide spectral resolution. Since the absorption spectrum of the gas filter is well known, if the laser frequency is scanned across the filter, then the Doppler-broadened and Doppler-shifted Rayleigh-scattered light will transmit through the filter, being acquired by the camera. Each pixel on the camera will then have obtained a convolution of the Rayleigh-scattered light with the absorption spectrum. These spectra can then be deconvolved to determine the gas temperature through the thermal broadening and gas velocity through the observed Doppler shift. Miles et al.[161] demonstrated this approach in a Mach 2 pressure-matched jet flow, shown in Fig. 3.4. Variations of this technique can provide both time-averaged and single-shot measurements. For single-shot measurements, the dynamic range of velocities that can be measured is limited, although by increasing the gas cell buffer gas pressure, the dynamic range has been increased by Elliot et al,. who made single-shot measurements with ~9% uncertainty over a velocity range from 200 to 600 m/s.[169,170]

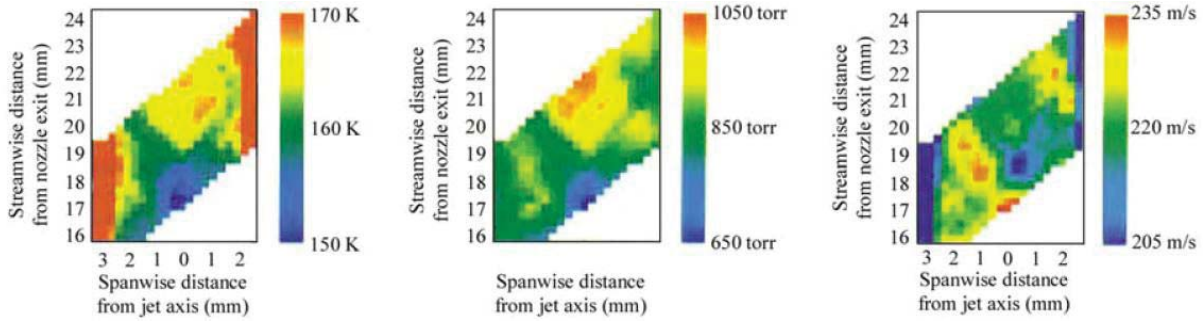

Figure 3.4. Temperature (left), pressure (center) and velocity (right) measured in a Mach 2 supersonic jet flow using Rayleigh scattering observed through a gas vapor cell using a frequency-scanned, injection-seeded Nd:YAG laser.[161]

By using a Fabry-Perot etalon, single-shot Rayleigh spectra can be obtained, allowing instantaneous (in ~100 ns) and simultaneous measurement of temperature, density and velocity. A Fabry-Perot etalon consists of two planar, reflective surfaces that cause interference, dispersing the transmitted light spatially, so that in the focal plane of the etalon, the spectrum of

the light is separated spatially and can be resolved spectrally. Two different strategies have been developed to acquire these spectra. The first uses a CCD camera in the focal plane of the etalon to capture the dispersed spectrum.[171-174] The second method uses spatial masks or mirrors to direct the Rayleigh-scattered light to single-point detectors such as photo-multiplier tubes (PMTs).[175,176] Typically, CCD cameras read out more slowly than single-point detectors such as PMTs, so using PMTs generally results in higher-speed detection. Measurement rates up to 32 kHz have been reported using this approach.[176] However, using a CCD camera offers several measurement advantages, described below.

Figure 3.5 shows one such example of CCD-based detection of Rayleigh-scattered light from Bivolaru et al.[173] A pulsed Nd:YAG laser is focused into a heated Mach 1.6 jet flow. The Rayleigh-scattered light is collected at right angles by a lens system which down-collimates the collected light and passes it through a solid etalon. The etalon-processed light is then focused on an electron-multiplying charged-coupled device camera (EMCCD) where the interference fringes are realized. This image is called an interferogram. An optical fiber (OF) directs some of the spectrally narrow laser light into the optical path so that a circular reference fringe will appear in the interferogram, as in Fig. 3.6(a). The pair of oval patterns located in the white rectangle show Doppler-shifted, Doppler-broadened, Rayleigh-scattered light collected by the lenses and dispersed by the etalon. A similar pattern is shown on the left side of the interferogram. These four oval patterns originate from four different spatial locations a few mm apart in the flow, thus resulting in four simultaneous, spatially-separated measurements. The gas velocity, $\boldsymbol{V}$, and the Doppler shift, Δf , are related by: $\Delta f = ((\boldsymbol{k_s}-\boldsymbol{k_o})\cdot \boldsymbol{V})/\lambda$, where λ is the wavelength of the incident light, $\boldsymbol{k_o}$ is the wave vector of the incident light and $\boldsymbol{k_s}$ is the wave vector of the collected light. (The wave vector points in the direction of light propagation and has a magnitude of $2\pi/\lambda$.) In the vector diagram shown in Fig. 3.5, $\boldsymbol{k_{o1}}$ is the wave vector of the incident light and $\boldsymbol{k_{s1}}$ is the wave vector of the collected light. The observed Doppler shift measures the velocity component V_1 in the direction defined by $\boldsymbol{k_{s1}} - \boldsymbol{k_{o1}}$, which bisects the angle β between the laser and collection wave vectors. Similarly, a mirror M_r reflects this incident beam back through the lens, L_2, and into the measurement volume with wave vector $\boldsymbol{k_{o2}}$ resulting in collected Rayleigh signal having a wave vector $\boldsymbol{k_{s2}}$. This signal is sensitive to the velocity component V_2. The reflected beam was slightly misaligned in the downward direction so that the two measurements would be spatially separated on the interferogram, shown in Fig. 3.6(a). Furthermore, the geometry of this experiment was constructed so that the V_1 would be orthogonal to the jet axis, measuring a radial velocity component while V_2 was parallel to the jet axis, measuring the axial velocity component. In Fig. 3.6(a), four spatially separated measurements of axial velocity are collected in the bottom half of the interferogram while four measurements of radial velocity are collected in the top half. Figure 3.6(b) shows the two boxed peaks after they have been processed to linearize the interferograms and to bin the data into single spectra.[172,173] These spectra were fitted with Gaussians to determine the Doppler shift and broadening associated with Rayleigh scattering, relative to the reference peaks. Subsequent

work by this team and others has been able to simultaneously determine the gas velocity, temperature and density from similar spectra.[177,178]

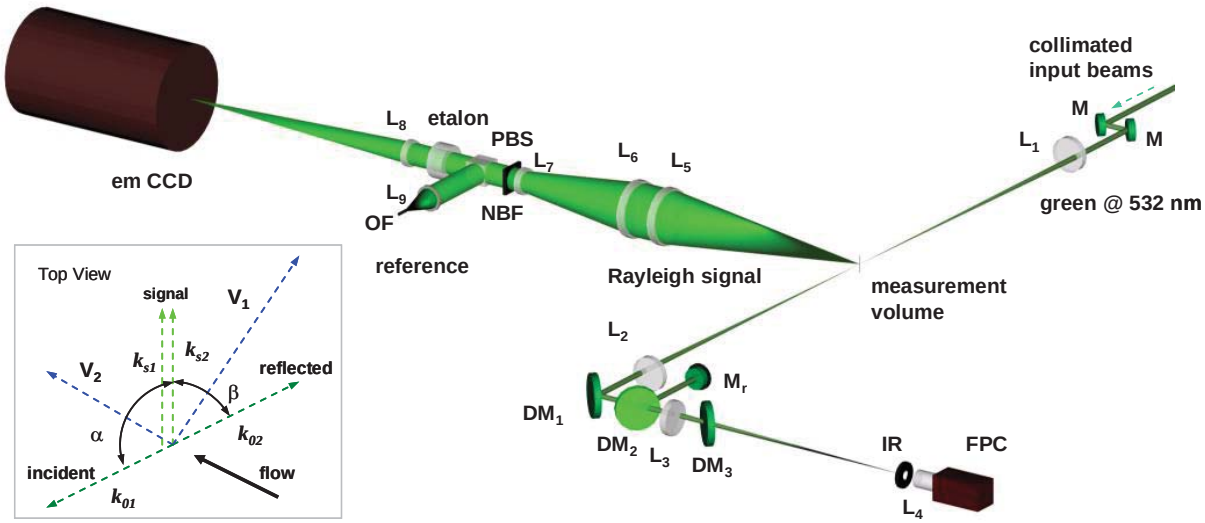

Figure 3.5. Two-component interferometric Rayleigh scattering system from Ref. 173. Mirrors are denoted by M, dichroic mirrors by DM and lenses by L. PBS is a polarizing beam splitter while NBF is a narrowband filter. IR is an iris and FPC is a focal plane camera used to monitor the beam alignment. In this experiment, the dichroic mirrors were required to filter out other laser beams associated with a dual-pump CARS measurement that was being performed simultaneously. Reprinted with permission of the authors.

In Ref. 173, Bivolaru et al. reported velocity measurements with a precision of ~40 m/s in a flow with ~1200 m/s, or about 3% of the maximum velocity. The dynamic range of the instrument was ~3000 m/s. (The dynamic range is mainly determined by the thickness of the etalon, which sets the free spectral range, or fringe-to-fringe spectral separation.) Thus, expressed as a percentage of the dynamic range of the instrument, the measurement precision is ~1%. To obtain more precise measurements at lower temperatures, the experiment can be designed to use higher spectral resolution.

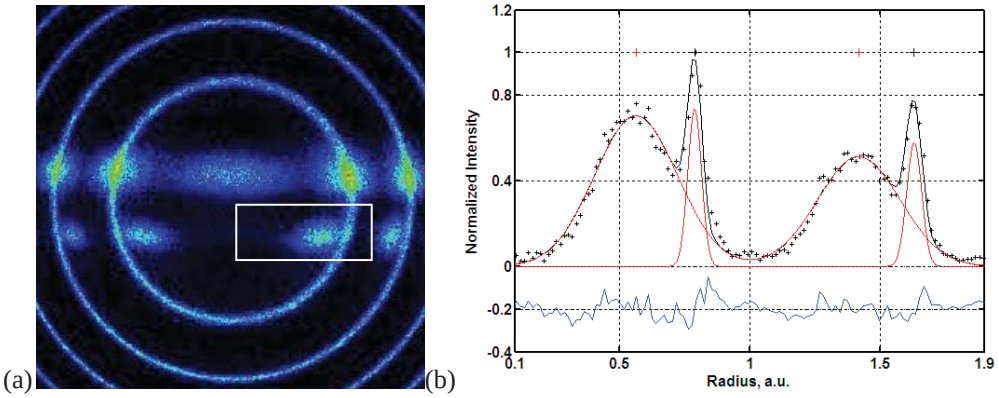

Figure 3.6. (a) Fabry-Perot interferogram of Rayleigh-scattered light obtained by laser beams from two different directions as well as laser-light, resulting in the circular pattern. (b) the linearized Rayleigh-scattered spectrum obtained from the boxed region in (a), showing best fits to the reference and Doppler-shifted light.[173] Reprinted with permission of the authors.

The use of the camera-based approach has some advantages over the PMT-based approach. First, it can tolerate (and in fact, benefits from) scattering from stationary surfaces in the flow. Such scattering, as long as it is not too large, provides a reference frequency to determine the Doppler shift. Second, having a laser frequency reference in each interferogram makes the system insensitive to variations in the etalon transmission spectrum or the laser wavelength. In typical PMT-based experiments, the etalon must be temperature controlled, vibration isolated (if it is an air spaced etalon) and the laser frequency must be carefully controlled. Uncontrolled drift in either the etalon or laser would result directly in a systematic error in the PMT-based approach while it is automatically corrected in the CCD-based approach. A third advantage of the CCD-based approach is that it is somewhat more tolerant of scattering from clusters and particles in the flow, lessening the need for gases to be filtered. Scattered light from particles typically appears in CCD-based interferograms as spatially distinct, circular artifacts. These can sometimes be removed by image processing. However, if the scattering is too large either spatially or in intensity, it can corrupt the measurement; even in this case, other spatial locations in the flow may yield measurements from the same interferogram. As shown in Fig. 3.6, the CCD-based detection allows multiple spatial points to be measured simultaneously, allowing measurements at adjacent spatial locations to be correlated. Furthermore, with CCD-based detection, it is straightforward to measure multiple velocity components with the same instrument, also shown in Fig. 3.6. Finally, CCD-based detection has often been combined with pulsed-laser excitation, which has two benefits: it makes the measurement instantaneous, occurring in ~10 ns, and the signal intensity is much higher, allowing measurement in much lower density flows, such as atmospheric-pressure flames and low-pressure gas flows. Instantaneous measurements at 1/5 of atmospheric density or lower are possible with this approach.[173]

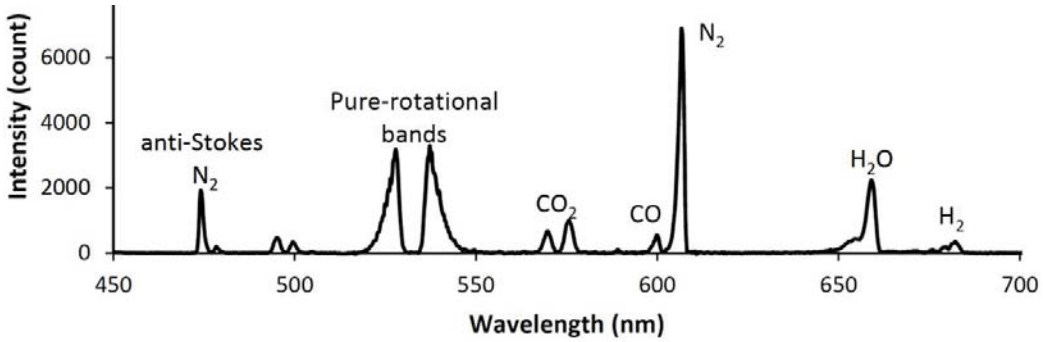

Figure 3.7. Five-hundred-pulse-average Raman spectrum in a high-pressure CH_4 air flame. The excitation laser wavelength was 532 nm. A 532 nm filter blocks Mie, Rayleigh and spurious laser scattering as well as some of the low-rotational-quantum-number rotational Raman lines. A subframe burst gating (SBG) technique was also used to subtract background emission from this spectrum.[179] Figure courtesy of and with permission of J. Kojima, NASA Glenn Research Center.

3.5 Rotational and Vibrational Temperature Measurements

Raman scattering is sensitive to individual molecular rotational and vibrational transitions. Since the population of these lines depends on (actually defines) the temperature, it is possible to measure rotational and vibrational temperatures from spontaneous Raman spectra. Figure 3.7 shows a typical Raman spectrum obtained in a hydrocarbon-air flame at high pressure.[180] A pulse-stretcher was used to extend the duration of the 500-mJ, 532-nm pulse by nearly a factor of 10, thereby lowering the peak laser power to avoid laser-induced breakdown while maintaining high pulse energy to yield a sufficiently high signal-to-noise ratio.[180] This spectrum shows many temperature and concentration dependent features. The relative heights and shapes of the different bands depend on temperature and gas concentration. Modeling, calibration and analysis of such Raman spectra can yield rotational and vibrational temperatures as well as concentrations. Several different strategies for temperature measurement based on spontaneous Raman scattering exist. Rotational temperatures can be measured from pure-rotational Raman scattering either using high-resolution or low-resolution detection, as indicated in Fig. 3.8.[181] The advantage of low-resolution detection is that the spectrum can be acquired simultaneously with the same instrument used to acquire multi-species spectra like that shown in Fig. 3.7. A disadvantage of this low-resolution technique is that many different species have similar pure rotational Raman shifts, so they overlap in the same spectral region close the excitation laser. Such interferences from different species can lead to measurement errors. This technique works over a wide temperature range, including at room temperature. Alternately, rotational temperatures could be determined by resolving the rotational-vibrational Raman scattering, typically of N_2,[182] as is often done for CARS.[183] When flows are in rotational-vibrational equilibrium, it is more common to measure the temperature using vibrational bands, as described below, because they result in higher signal-to-noise ratios and consequently, more precise temperature measurements.

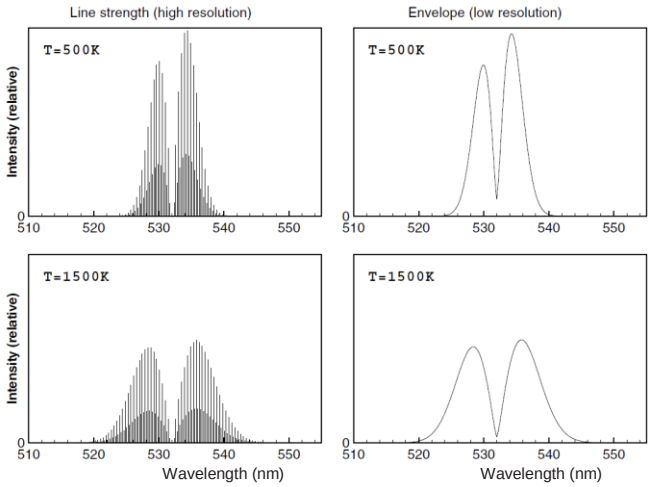

Figure 3.8. Theoretical calculation of the pure rotational Raman spectra of N_2 at two different temperatures and two different spectral resolutions, adapted from Ref. 181. © IOP Publishing. Reproduced with permission of the authors and of IOP Publishing. All rights reserved.

Vibrational temperatures can be measured from the relative heights of different vibrational Raman bands. A commonly used method compares the ratio of the Stokes to anti-Stokes (S-AS) vibrational Raman bands of N_2. [42, 184 - 186] N_2 is often used because it is present in high concentration in many supersonic, hypersonic and combusting flows, resulting in adequate

signal-to-noise ratio. Also, N_2 is used because it is relatively well understood and well resolved spectrally from other species. Recall from Fig. 3.1 that the anti-Stokes scattering originates from an excited vibrational state whereas the Stokes scattering can originate from the ground vibrational state. Thus, the integrated intensity of the anti-Stokes N_2 spectrum at 473 nm in Fig. 3.7 can be compared to the Stokes scattering at 607 nm to determine the temperature. This ratio is a monotonic function of temperature. Since this method integrates the signal intensity in the two different bands, it improves the signal-to-noise ratio, allowing single-shot determination of temperature. Single shot precisions of ~20% of the measured temperature have been obtained at several points along a line using this method.[184] This technique becomes insensitive to temperature below about 700 K because the low population in the excited vibrational state causes low signal-to-noise ratio. [42]

A second method of measuring the vibrational temperature is to spectrally resolve the different vibrational bands of a molecule such as N_2, though the individual rotational lines need not be resolved. The relative heights of the vibrational levels can be plotted on a Boltzmann plot or can be fitted spectrally to determine the vibrational temperature.[187] For example, Sharma and coworkers[187] used a KrF excimer laser operating at 248 nm to generate spontaneous Raman scattering in the Electric Arc Shock Tube (EAST) facility at NASA Ames Research Center. The EAST facility, normally operated as a shock tube, was fitted with a two-dimensional converging-diverging nozzle so that a shock reflection generated a high pressure (100 atm), high temperature (5600 K) reservoir of N_2 gas that expanded through the nozzle. The sudden expansion through the nozzle results in vibrational-rotational nonequilibrium, which was monitored with Raman scattering. Measurements were performed at different distances downstream to study the evolution of the vibrational relaxation. Figure 3.9 shows a sample spectrum generated and spectrally fit to determine the rotational and vibrational temperatures. The vibrational temperatures were then plotted versus distance downstream in the flow so that different vibrational relaxation models could be tested.[187] Though not explicitly stated in the paper, the temperature measurement precision appears to be about 5%.

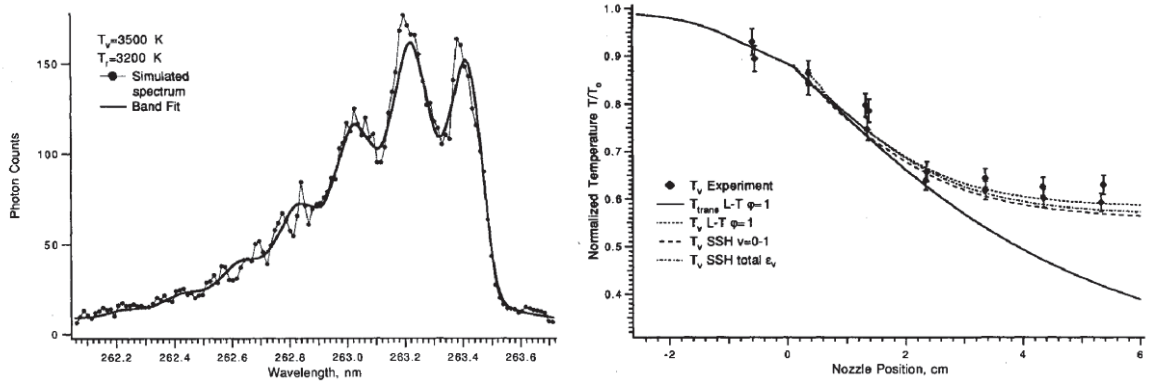

Figure 3.9. An experimental Raman spectrum of N_2, fitted for rotational and vibrational temperature (left), and resulting vibrational temperatures measured as a function of distance downstream of the nozzle (right), adapted from Ref. 187 with permission of the authors.

3.6 Species Concentration Measurement

Rayleigh scattering has been used in some specialized experiments for determining species concentration. For example, the Rayleigh scattering cross section for propane is 13.5 times larger than for air, allowing mixing to be quantified in propane/air jets.[188] However, *Raman* scattering is much more commonly used to measure species concentrations. Sandia National Laboratories have extensively used Raman scattering for major-species concentration measurements (along with Rayleigh and LIF measurements for temperature and minor-species concentration measurements, respectively).[91] This system uses a series of four frequency-doubled Nd:YAG lasers to produce temporally-stretched 1.8 Joule pulses which are focused to a 0.22 mm ($1/e^2$) diameter spot size. A separate laser excites LIF of CO. An imaging system directs the collected Raman/Rayleigh/LIF scattered light into the optical analysis system shown in the bottom-right panel of Fig. 3.10. The system contains two mechanical chopper wheels (one "slow" and one "fast") which are synchronized with the laser to transmit the signals while rejecting flow luminosity. It also has a transmission grating and multiple lenses, beam splitters and cooled (low noise) CCD cameras. This system images a 6-mm-long segment of the Rayleigh, Raman and LIF probe volume, allowing concentrations and temperature to be obtained along a line. The spatial resolution for the Raman measurements was ~10 pixels / mm along the 6-mm-long probe volume, though the actual spatial resolution was slightly worse due to optical distortions from the flame.[91]

A sample of the resulting concentration measurements are shown in Fig. 3.10. Raman has been used to measure N_2, O_2, CH_4, CO_2, H_2O and H_2 while CO was measured with two-photon LIF excited at 230.1 nm. Temperature was measured from the intensity of the Rayleigh-scattered light, using the ideal gas law to convert density to temperature as described above. The data are graphed versus temperature to show the correlation of species with temperature and to allow comparison with an unstrained flame calculation, shown in blue. The individual (red) data points correspond to different single pulses of the laser. Thus, these measurements are 'single shot' having been obtained with flow freezing (~100 ns) time resolution. Data such as these have been acquired at many locations in a variety of different flames, allowing the development of a large database of turbulent flames. The accuracy of the Raman concentration measurements varies from 2% to 10% of the measured concentration, while the precision (based on one standard deviation) varies from 0.7% to 7.5% depending on the species. The accuracy of the temperature measurement, based on Rayleigh scattering signal intensity, was reported to be 2% with a 1-σ precision of 0.75%.

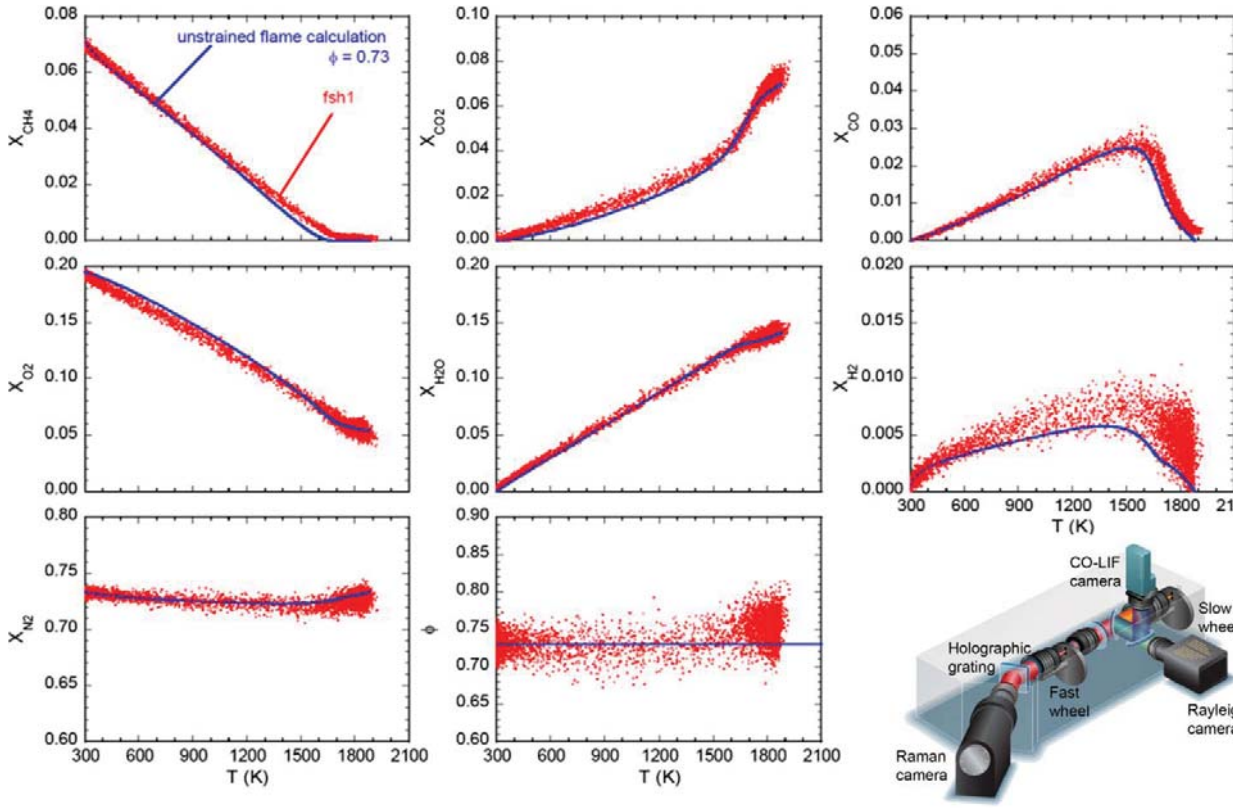

Figure 3.10. Scatter plots of mole fraction and equivalence ratio (ϕ) data at one location in an atmospheric pressure, methane-air flame compared with a calculation, and a schematic of the optical components associated with the collection and analysis of light from the Sandia Raman/Rayleigh/LIF imaging system (bottom right). Adapted from Ref. 91 with permission of the authors and the The Combustion Institute.

4. Coherent Anti-Stokes Raman Spectroscopy

4.1 Introduction

Comprehensive reviews of the theory and application of Coherent anti-Stokes Raman spectroscopy, often called coherent anti-Stokes Raman *scattering*, or CARS, in a gas have been given by others. [42,43] Herein we provide a brief introduction and overview. CARS is a non-linear optical process in which three laser beams interact with the gas generating a fourth, laser-like signal beam. The energy level diagram of this process (each arrow represents a change in state due to photon absorption, an up arrow, or emission, a down arrow, and the length of the arrow is proportional to energy change or, equivalently, photon frequency) is shown in Fig. 4.1 The pump beam and the lower frequency

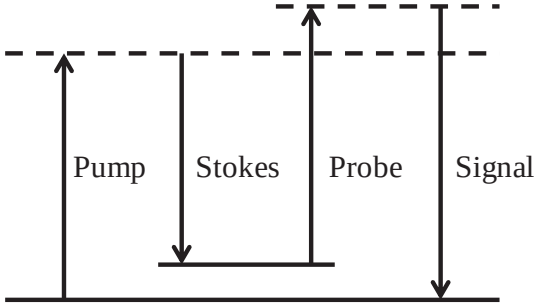

Figure 4.1. Energy level diagram showing the CARS process

Stokes beam interact with the gas, a pump frequency photon is absorbed and a Stokes frequency photon is emitted coherently with the Stokes beam, and the gas is excited to a higher energy state via a state that in most CARS setups is a virtual state (although it could also be a real state). The difference between the frequencies of the upper and lower state, $\omega_{pump} - \omega_{Stokes}$, is called the Raman shift. A probe beam photon is coherently scattered from this excited state, shifted up in frequency by the Raman shift to form part of the signal beam, and the gas molecule returns to its original state. Total momentum as well as energy is conserved. Therefore, the momentum of the scattered photons equals that of the incident photons, leading to the following equation:

$$\overrightarrow{k_{pump}} + \overrightarrow{k_{probe}} = \overrightarrow{k_{Stokes}} + \overrightarrow{k_{signal}} \tag{4.1}$$

Since the *k*'s are the wave vectors (length proportional to photon frequency with direction the same as that of the beam), this equation allows the direction of the signal beam to be found from the directions of the pump, Stokes, and probe beams.

A physical interpretation of this process is that the interaction of the pump and Stokes beams establishes a optical fringe pattern in the gas. If the pump and Stokes frequencies are the same, as with a related technique called degenerate four-wave mixing (DFWM), this fringe pattern is stationary. In CARS, the frequencies are different and the fringe pattern moves across the interaction region, modulating the intensity at any particular point at the beat frequency, i.e., the Raman shift frequency. This moving fringe pattern excites a polarization response in the gas which acts as a moving grating from which a probe beam photon is scattered, in a manner similar to Bragg scattering, to form the signal beam photon. Since the grating is moving, the frequency of the signal photon is shifted relative to the probe photon by the Raman shift frequency. (An analogous effect occurs in an acousto-optical modulator where acoustical waves in a solid material, such as glass, form a moving grating of varying index of refraction, and incident laser light is coherently or Bragg scattered from this volumetric "grating" with its frequency shifted by the acoustical frequency.[189])

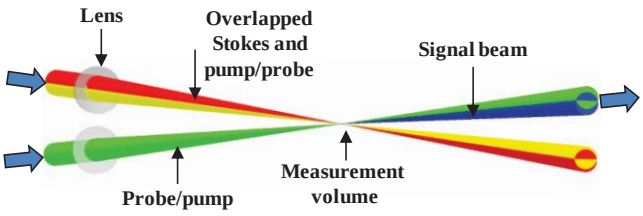

Figure 4.2. Planar BOXCARS beam geometry

If the pump, probe, and Stokes lasers are all single frequencies, then the signal is also at a single frequency, as indicated in Fig. 4.1. If the pump and/or Stokes lasers are broadband lasers, while the probe is single frequency, then the signal is broadband also, and contains a spectrum that reflects the variation of CARS susceptibility of the molecules in the probe volume as a function of Raman shift. In many broadband CARS setups, the probe and pump frequencies are the same (derived from the same laser source). In the dual-pump CARS technique, [42,190] pump and probe frequencies are different and these two laser beams have interchangeable roles (each beam performs the role of pump in one CARS process and probe in a second CARS process). The signal is thus the coherent superposition of the signal from the two processes, generated over two different ranges of Raman shift. When the desired

Raman shift is small, as in rotational CARS (i.e., when the transitions probed are pure rotational transitions, which differ by relatively small quanta of energy and are thus relatively closely spaced spectrally), the pump and Stokes beams can be derived from the same broadband laser while the probe beam is single frequency (dual-broadband CARS). [42]

Since CARS is a non-linear process (see Section 1.2) it requires high irradiance levels. Consequently, CARS signal in a gas is typically generated by focusing pump, Stokes, and probe beams, and overlapping them at their common focus. If the beams are initially separate and crossed at the common focus, the arrangement is called BOXCARS; if they lie in a plane (Fig. 4.2), it is called planar BOXCARS. In this arrangement the measurement volume is the small region of overlap of all three beams.

4.2 CARS Theory[42,43 ,189]

CARS, like Raman and Rayleigh scattering, arises because of time-varying polarization induced in the gas in the presence of electromagnetic radiation. CARS, specifically, arises due to the third order susceptibility, χ_{CARS}, for which the induced polarization is described as follows:

$$P^{(3)}\left(\omega_{signal}\right) = \epsilon_0 \chi_{CARS} E(\omega_{pump}) E(\omega_{Stokes}) E(\omega_{probe}) \tag{4.2}$$

The *E*'s are the complex electrical field amplitudes. This equation can be substituted into the wave equation relating the electrical field to the induced polarization and solved by integration along the direction of the signal beam. The CARS irradiance is thus:

$$I_{signal} \propto I_{pump} I_{Stokes} I_{probe} |\chi_{CARS}|^2 L^2 \tag{4.3}$$

L is the length of the measurement volume, i.e., the length of the region along which the pump, Stokes, and probe beams all overlap. Rigorous calculations of the CARS susceptibility require quantum mechanical treatments, but classical derivations are simpler to understand. The gas is modeled as a simple harmonic oscillator in which the variation of the normal coordinate, *Q* (intermolecular spacing in the case of vibrational states), with time is described by a second order linear ordinary differential equation, with a time-dependent forcing function proportional to the average over an optical cycle of the square of the electrical field. (Thus, the forcing term oscillates at the Raman shift frequency.) The constant of proportionality in the forcing term is proportional to $\left(\frac{\partial \alpha}{\partial Q}\right)_0$, and consequently to the Raman scattering cross section, where α is the optical polarizability of the molecule. The CARS susceptibility is found by solving for the time dependence of the normal coordinate, combining with Eqs. (4.1) and (4.2) for the polarization (from the chapter on Rayleigh and Raman scattering), and comparing with Eq. (4.2):

$$\chi_{CARS} \propto \frac{N\left(\frac{\partial \sigma}{\partial \Omega}\right)}{\Delta\omega\left(2-\frac{\Delta\omega}{\omega_v}\right)+i\left(1-\frac{\Delta\omega}{\omega_v}\right)\Gamma} \tag{4.4}$$

The susceptibility is proportional to the molecule number density, *N*, and the differential Raman cross section, $\left(\frac{\partial\sigma}{\partial\Omega}\right)$, and reaches a peak where the detuning, $\Delta\omega \equiv \omega_v - \left(\omega_{pump} - \omega_{Stokes}\right)$, approaches zero. The damping coefficient, Γ, determines the line width. A quantum-mechanical treatment yields the following equation:

$$\chi_{CARS} = \sum_j \frac{K_j \Gamma_j}{2\Delta\omega_j - i\Gamma_j} + \chi_{nr} \text{ where } K_j \propto N\Delta_j \left(\frac{\partial\sigma}{\partial\Omega}\right)_j \tag{4.5}$$

The index *j* refers to a particular transition and Δ_j is the fractional difference in the population of the two states of the gas between which a transition is taking place (the two real levels in the energy level diagram of Fig. 4.1); χ_{nr} is the non-resonant susceptibility, a nearly constant term for the CARS process in which all the states in Fig. 4.1, other than the ground state, are virtual states. The (real part of the) line shape in Eqn. (5) is a Lorentz function with full-width at half maximum equal to Γ_j. This line shape is the same as the (complex conjugate of the) line shape for the classical solution when the detuning is small relative to the vibrational frequency. The line width depends inversely upon the lifetimes of the two states involved in the transition, which depend upon the rate of collisions between molecules (collisional broadening). Light emitted by molecules in motion is observed at a slightly different frequency by a stationary observer by an amount proportional to the velocity component towards the observer. This effect, when averaged over many molecules travelling in different directions, results in Doppler broadening. Since the distribution of molecular velocity components about the bulk mean in a gas in equilibrium is Gaussian, the line shape becomes a Voigt profile, a convolution between Gaussian and Lorentzian functions. At pressures much above atmospheric, additional line narrowing effects occur.

Since the CARS signal is proportional to $|\chi_{CARS}|^2$, a CARS spectrum reflects the populations of the molecular energy states involved in the transitions. Since these populations, in equilibrium, are related via the Boltzmann equation to the temperature, CARS can measure temperature. Integrated CARS signal is also strongly dependent upon number density and, in principle, could be used to measure density. This is not typically done because of experimental difficulties in maintaining a consistent geometry of the laser beams at the beam intersection. Small uncontrolled motions of the beams due to refraction in inhomogeneous gas fields, movements of the optical system, variation in the quality of the laser beams, etc., cause changes in signal intensity, and calibrations fail. However, where two gas species are resonant in a spectrum, the ratio of the population of one species to another may be found from the shape of the spectrum. Where only one species present is resonant, but χ_{nr} is known, the fraction of that species may be found from the relative amplitude of the resonant signal to the non-resonant "background"; however, χ_{nr} depends on the number density of all species present. If all species but one are resonant in the spectrum then the composition can be fully determined by reference to the non-resonant background.[191] Use of CARS as a diagnostic tool requires comparison of experimental and theoretical spectra.[192] Calculation of theoretical spectra is quite complex and

numerically time-consuming: after computation of theoretical susceptibility, spectra must be convolved with laser line shapes and instrument probe function.[193]

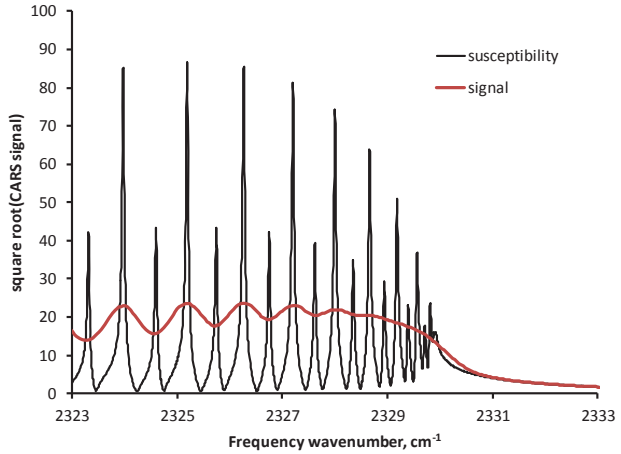

Figure 4.3. CARS N_2 Q-branch susceptibility and spectrum near bandhead at 1 atm., 1400 K.

Nitrogen is a very useful species for measurement of temperature since it is usually present in fuel-air combustion or hypersonic flows, and is readily probed by CARS. The band head of the N_2 Q branch is located at a Raman shift of 2330 cm^{-1} (units of inverse wavelength, proportional to frequency divided by the speed of light), and is readily accessible using available lasers. The Q branch occurs as a result of transitions between adjacent vibrational states ($\Delta v=+1$, where v is the vibrational quantum number) with no change in the rotational state ($\Delta J=0$, where J is the rotational quantum number). Figure 4.3 shows a portion of the N_2 Q-branch spectrum near the band head. Transitions are between v=0 and v=1and each peak corresponds to a different J value. Since rotation of the molecules affects the energy associated with a given vibrational state, the energy difference between v=0 and v=1 (at given rotational level) is a function of the rotational level. Two spectra are shown in this figure – the first is the CARS susceptibility and the second is a computed typical broadband CARS spectrum formed by convolution of typical laser line shapes and a typical instrument function with the susceptibility.[193] As may be seen, line shapes are typically not fully resolved in experiments.

Figure 4.4 shows the sensitivity of the signal spectrum to (a) temperature and (b) concentration. The calculations are for (a) air and (b) either air (79% N_2) or 10% N_2, 21% O_2, 69% H_2O, with a pressure of 1 atmosphere. The CARS signal strength varies strongly with temperature, partly through the effect of temperature on density (N) via the N^2 dependence of the CARS susceptibility. By using the Sandia CARSFT code,[192] the pressure and temperature dependence at moderate to high pressures was determined to be proportional to[194] $p^2T^{-3.5}$. However, the shape of the spectrum also changes. At low temperature, only one vibrational band is present, associated with v=0 to v=1 transitions, and is relatively narrow (because fewer J levels are occupied). At the higher temperatures, "hot" bands are present also, associated with v=1 to v=2 and v=2 to v=3 transitions, and more J levels are populated. As the fraction of N_2 is reduced, the amplitude of the band structure becomes smaller relative to the non-resonant background, and sensitivity to N_2 is lost for concentrations less than a few percent. This lack of sensitivity below a few percent is typical and prevents measurement of minor species, although a number of CARS techniques, for example *resonance* CARS (e.g., Ref. 195), have been developed to circumvent this limitation.

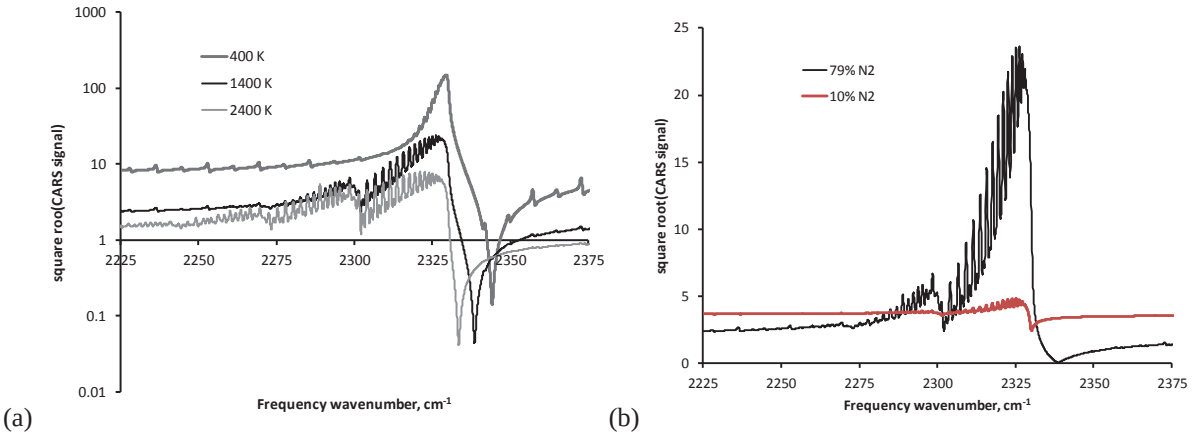

Figure 4.4. Effects of (a) temperature and (b) concentration on the CARS N_2 Q-branch spectrum.

4.3 Ultrafast CARS

Ultra-fast techniques have been surveyed by Roy et al.[196] The CARS technique as described above is a steady-state process involving the mixing of four beams simultaneously present. For given laser energy available in the pump, probe, and Stokes laser beams, the energy in the signal beam is proportional to t^{-2}, where t is the time over which the measurement is made. Nanosecond (ns= 10^{-9} s) CARS is performed with Q-switch pulsed lasers where the pulse energy is distributed over 5 ns to 10 ns, at a pulse rate on the order of 10 Hz. There are many 10's or 100's of thousands of Raman frequency cycles during each laser pulse, so that CARS is effectively a steady-state process. However, with the advent of femtosecond (fs= 10^{-15} s) lasers (e.g., titanium-sapphire), very short pulse widths of order 10^{-14} seconds are possible at high pulse repetition rate (1 kHz or more), and the pulse width is less than the period of a Raman cycle. Due to the t^{-2} scaling, strong signal energy is available with modest pulse energy.

The theory of fs CARS is different from ns CARS since a steady state problem is replaced with an impulsively initiated, time-dependant one.[197] First, a polarization grating is established in the gas by the interaction of pump and Stokes beams. This grating evolves in time through rotational-vibrational relaxation and then, after some delay (typically up to several hundred picoseconds in measurement applications), a signal is generated by scattering the probe pulse off the grating. By making measurements at different probe delays the relaxation of the grating, which carries with it an imprint of the vibrational and rotational state of the probed molecules, may be observed. "Chirping" techniques have been developed where the probe beam is broadened both temporally and spectrally in such a way that the frequency of the probe varies with time. The temporal relaxation is thus mapped into frequency space, obtained in a single laser pulse, and may be analyzed with an optical spectrometer.[198]

Picosecond (ps = 10^{-12} s) CARS employs mode-locked solid state lasers with pulse lengths on the order of 10 ps and has characteristics of both ns and fs CARS. As with fs CARS, generation of the grating by the pump and Stokes beams, and scattering of the probe to form the

signal, are typically separate steps. However, the probe pulse is still relatively long compared with the Raman cycle period, and the signal contains an optical spectrum similar to that of ns CARS.[199] An advantage of ps CARS over ns CARS is that the ps pulses required to obtain adequate signal-to-noise ratio CARS spectra are better suited to pass through commercially available optical fibers without damaging the fibers.[200] Both fs and ps CARS have the potential advantages over ns CARS of much higher data (pulse) rates and the absence, when the probe is delayed relative to the pump-Stokes laser pulses, of non-resonant background effects. Another advantage of fs CARS is simpler theoretical modeling, since few or no collisions occur in the time of the measurement (negligible collisional effects).[196]

4.4 Advantages and Disadvantages of CARS for probing Supersonic and Hypersonic Flow

In hypersonic propulsion systems (scramjets), flow velocities are supersonic in inlets and nozzles, and may be supersonic or a mixture of subsonic and supersonic in the combustors. In combustors, pressures are roughly one atmosphere while temperatures are similar to those of low speed combustion. Thermal non-equilibrium (not typically present in low speed combustion) as well as chemical non-equilibrium can be present due to the short flow through time (on the order of milliseconds). CARS has several advantages in this application. The signal comes as a laser beam, which means that it can be collected through a relatively small aperture and may be separated from non-coherent interferences by spatial filtering. This is particularly useful in an engine combustor where there may be emission from the gases and thermal radiation from the wall, and where, for structural reasons, it may not be possible to incorporate large windows. CARS measurements are spatially and temporally resolved, with ~1.5 mm long and 50 μm diameter measurement volume, and a 10 ns time scale. CARS is able to non-intrusively measure local temperature and composition. Since the Q-branch spectrum reflects the rotational-vibrational state of the molecule, the populations of these states may be directly determined, which is useful when thermal equilibrium (and therefore a single "temperature") does not exist.

CARS has been used much less frequently in hypersonic freestreams, where temperatures and pressures can be very low. Due to the previously-mentioned $p^2T^{-3.5}$ scaling of the CARS signal, the signal to noise ratio may be low. At low temperatures only the vibrational ground state and far fewer rotational states of molecules are populated. Vibrational CARS (e.g., of the N_2 Q-branch) then depends upon measuring high resolution spectra of the rotational structure of the "cold" band near the band head, which depends upon the pressure-dependent collisional effects on line shape, as well as temperature. Measurements of both pressure and temperature, at pressures down to about 0.1 atm., have been made in an underexpanded supersonic jet using this approach.[201] If the v>0 bands are populated at low rotational temperature (vibrational non-equilibrium), this can be easily measured. Alternatively, pure rotational CARS ($\Delta v=0$, $\Delta J=\pm 2$) is sometimes used at low temperatures since the lines have greater separation than in the Q-branch, but no information on the vibrational state is obtained.[202]

CARS has some disadvantages compared to other measurement techniques. It typically measures at only a single point, and so does not typically provide simultaneous information at multiple spatial locations. Instead, the probe volume is typically scanned around the flow allowing time-averaged spatial properties to be measured. The data rate is low in ns systems (order 10 Hz) so that in pulsed hypersonic facilities only one single measurement is obtained per facility run. Also, its ~1.5 mm long probe volume can be too large in certain applications where it is desired to resolve small length scales such as shock waves, shear layers or turbulent eddies. CARS requires optical access on two sides of the flow, which may limit application in some facilities. The experimental setup for CARS, involving two or three pulsed laser systems along with large spectrometer(s), is relatively complicated and time consuming to set up. Furthermore, the nonlinear nature of the theory of CARS complicates the interpretation and analysis of the resulting spectra. However, with the combination of accurate and precise temperature and multi-species measurement capabilities, CARS is commonly used in many supersonic and hypersonic flow applications.

4.5 Temperature and Mole Fraction Measurement

Extensive dual-pump CARS measurements have been made in a dual-mode scramjet burning hydrogen.[203] The CARS lasers, which were located outside the scramjet lab, consisted of an injection-seeded Nd:YAG, frequency doubled to 532 nm, an in-house broad band dye laser (Stokes laser) centered around 603 nm with FWHM of 10 nm, and a commercial narrow-band dye laser centered around 550.5 nm. Beams were relayed to the experiment via a translation system that could move the measurement volume and through special slotted windows in the scramjet. Beams were focused and crossed in the scramjet in a planar BOXCARS arrangement (Fig. 4.2) to form the measurement volume. The signal beam was transmitted out of the scramjet, recollimated, separated from one of the pump beams, relayed to a 1 m spectrometer, then imaged onto a cooled CCD array with 1340×100 pixels. The measured spectra were background subtracted and normalized by a CARS spectrum in argon, which has no resonances, to remove the spectrum of the broad-band laser. The resulting spectra were fitted to theory, using the Sandia CARSFIT code[192] to generate the theoretical spectra and an in-house fitting code[193] to do the fitting, resulting in temperature standard deviations of ~3%.[204] The fitted parameters included vibrational temperature of N_2, a single rotational temperature for all resonant species, and mole fractions of N_2, O_2, and H_2. Figure 4.5 shows some typical (averaged) measured spectra and fits to theory. Spectrum (a) was in the freestream air of the flow and is shown with a fitted rotational temperature of 923 K and vibrational temperature of 1133 K. N_2 and O_2 Q-branch resonances may be seen. The freestream thermal non-equilibrium was a test facility effect. Spectrum (b) is in the combustion plume and shows H_2 rotational (S) lines as well as the aforementioned Q-branches, with fitted rotational and vibrational temperatures of 1588 K and 1766 K respectively. Figure 4.6 shows contour maps of vibrational temperature in the combustor. The wireframe represents the corners of the flow path; a single hydrogen injector is seen at the downstream surface of the small ramp, on the top surface of the flow path. Flow enters at Mach 2 from the

test facility nozzle, and is from left to right. The development of the combustion may be seen: combustion is initiated on the top of the plume of hydrogen, near the fuel injector, and wraps around and engulfs the plume further downstream.

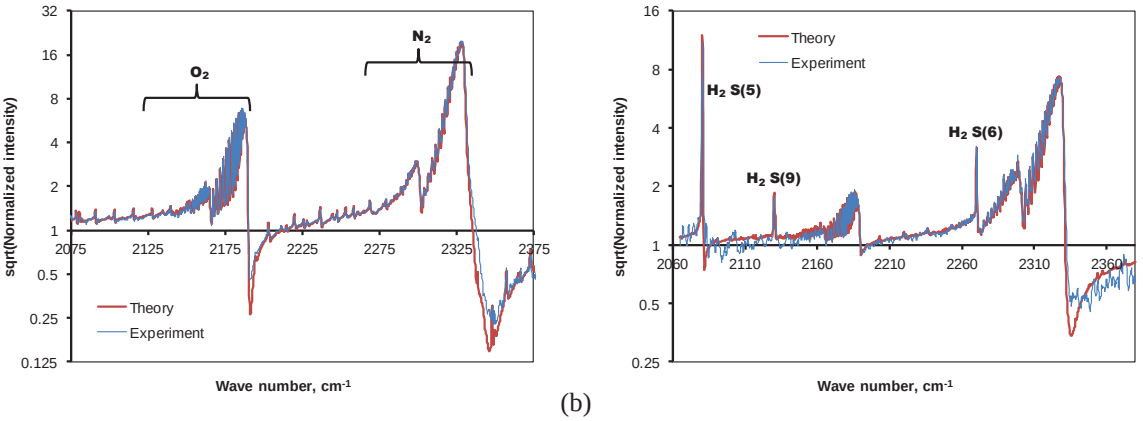

(a) (b)

Figure 4.5. Typical fits of theory to experimental dual-pump CARS spectra in a dual-mode scramjet: (a) freestream, (b) combustion plume.

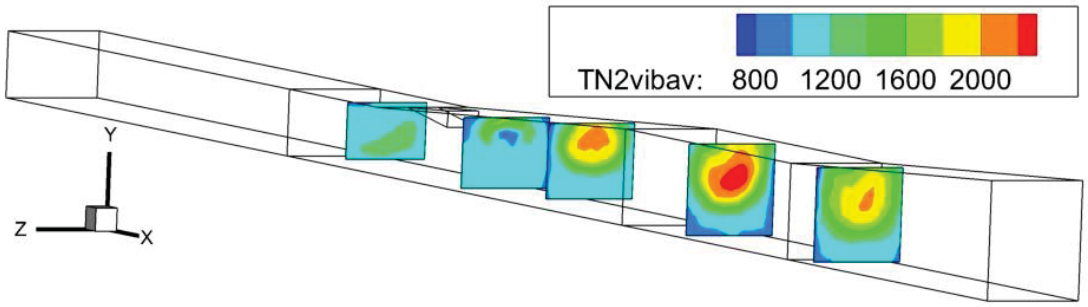

Figure 4.6. Contour plots of CARS-measured mean vibrational temperature in a dual-mode scramjet.

Simultaneous with the temperature measurements, species concentrations were also determined from CARS data. The concentration information was derived from the relative intensity of the different resonant features in the CARS spectra, comparing to the intensity of the nonresonant background, and considering that the mole fractions must sum to one.[191] Figure 4.7 shows CARS mole fraction measurements obtained at the same conditions as Fig. 4.6. The mole fraction is uniform air in the first plane at the left of each of the figures. Evidence of the cold H_2 fuel jet is seen in the temperature map (Fig. 4.6) and all three mole fraction maps in the second plane, which is located just downstream of the fuel injector (Fig. 4.7). As the fuel jet spreads spatially and is consumed by combustion, the presence of N_2 in the center of the downstream fuel plume shows evidence of fuel-air mixing. However, the O_2 mole fraction does not track exactly with the N_2 because it is reacting with the H_2. Not until the final plane at the right side of each figure, when all the H_2 is consumed, does the O_2 penetrate to the center of the duct, in the wake of the fuel plume.

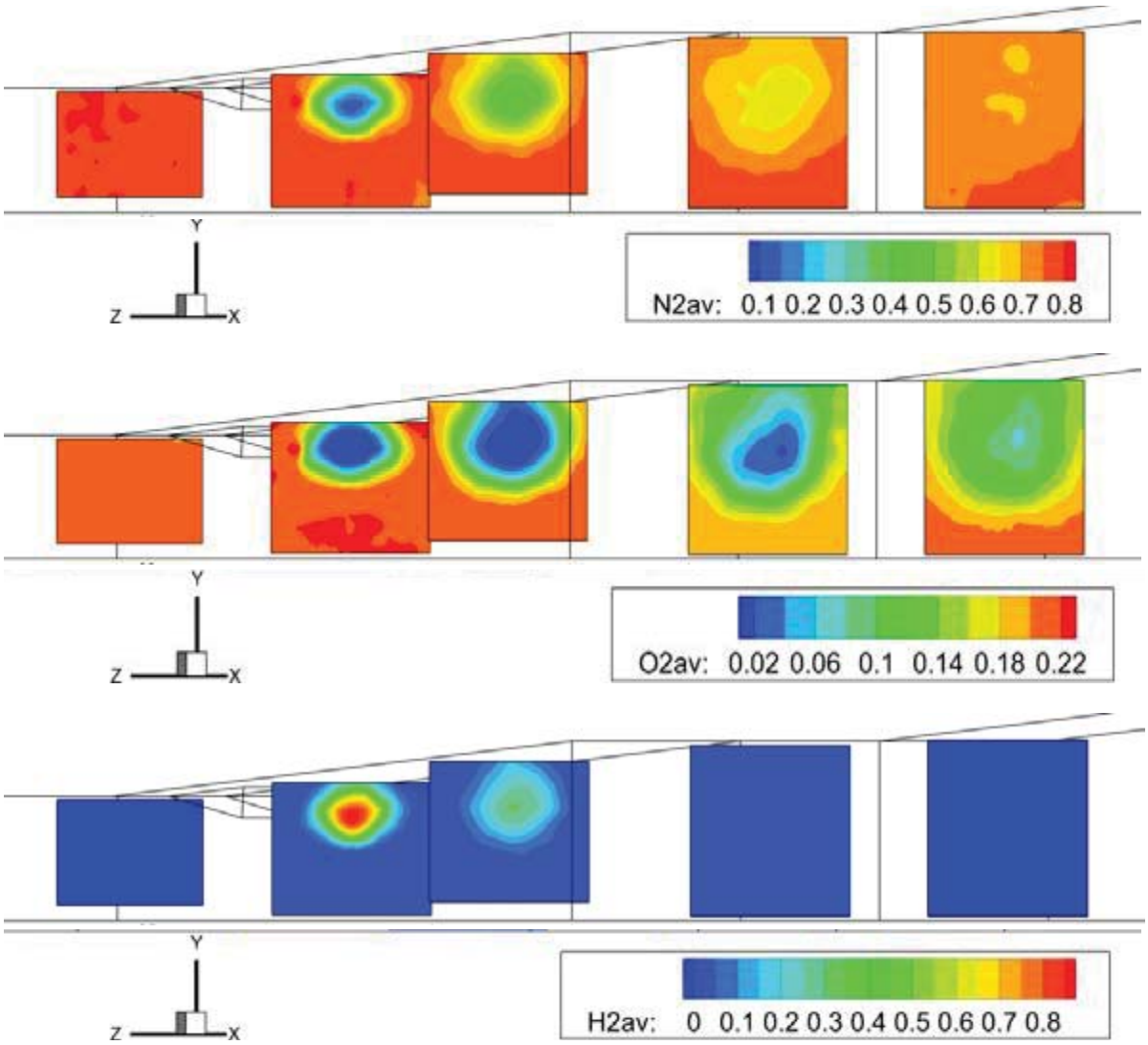

Figure 4.7. Contour plots of CARS-measured mean mole fractions of N_2 (top), O_2 (middle) and H_2 (bottom) in a dual-mode scramjet at the same conditions as Fig. 4.6.[203] Reprinted with permission of the authors.

In summary, CARS is a powerful technique for simultaneously and quantitatively measuring multiple flow parameters in gas flows with thermal and/or chemical non-equilibrium. If the gas is in thermal equilibrium, CARS can be used to measure temperature; if not it can provide information on rotational and vibrational (for rotational-vibrational CARS) state populations, allowing separate determinations of rotational and vibrational temperature. It also can be used to make quantitative measurements of the relative concentration of the species probed. It is spatially and temporally resolved, with a short measurement time (10 ns – 10 ps) and a measurement volume that is typically order 1 mm long. Nanosecond CARS is limited by available lasers to measurement rates of about 10 Hz, but femtosecond CARS data rates are often 1 kHz or more. Nanosecond CARS is a well-established technique, picosecond and femtosecond

CARS in gases is quite recent, due to the advent of suitable lasers, and techniques are still under development. The primary limitations of CARS include its complexity (which has meant relatively few applications of it to large-scale test facilities), the fact that measurements are pointwise and not planar or volumetric, and (for nanosecond CARS) the low data rate. Other issues include sensitivity to optical misalignment due to vibrations or refractive index variations along the beam path, and lack of spectral modeling for some species.

5. Other Molecular-Based Measurement Techniques

5.1 Introduction

Many different surface-based, probe-based and particle-based instruments have been used to study transition and turbulence. However, this manuscript focuses only on molecular-based measurement techniques. Raman scattering, Rayleigh scattering, laser-induced fluorescence (LIF) and coherent anti-Stokes Raman spectroscopy (CARS) are some of the most commonly used techniques, and for this reason have been detailed in the preceding sections. This section briefly describes additional molecular-based measurement techniques that have been used, or that show some promise for use, in studying transition and turbulence in high speed flows.

5.2 Interferometry

Interferometry uses interference of light to measure small changes in optical path length. Variation in gas flow properties along the optical path cause the index of refraction to vary, which generates these path length changes relative to a reference path. The two paths are then aligned onto a one- or two-dimensional detector where interference (or a so-called *interferogram*) is observed. This method is very sensitive because it can measure optical path differences that are fractions of a wavelength of the light from which they are generated.

In fluid mechanical applications, interferometry is usually used for flow visualization or to measure the gas density. The gas density is related to the index of refraction through the Gladstone-Dale equation:

$$n - 1 = K\rho \tag{5.1}$$

Where n is the index of refraction, ρ is the density and K is the Gladstone-Dale constant, which depends on the gas and the wavelength of light. The Springer Handbook of Experimental Fluid Mechanics recently reviewed applications of various types of interferometry to fluid mechanics.[162] These include Mach Zehnder interferometry, holographic interferometry, shearing interferometry and others. The different interferometric methods can be sensitive to the density or the gradient in density.[162] As a path-averaged measurement technique, most interferometry techniques require experimental methods and/or analysis to determine spatially-resolved information. If measurements along multiple lines of sight can be obtained, tomographic reconstruction can be used to deconvolve spatial information. Or, in axisymmetric flows, an

Abel inversion can be used. However, in the general case of 3D turbulent and transitional flows, these approaches are challenged by the short spatial and temporal scales of the experiments, which require many simultaneous high-resolution views from different angles. While time-averaged measurements in such turbulent flow fields are possible, it is more difficult to use these methods to resolve small temporal or spatial scales.

Laser differential interferometry (LDI) is a sensitive method that has been used to detect weak perturbations in low-noise wind tunnels that have been developed to study hypersonic transition to turbulence.[205] This technique uses two loosely focused, parallel beams that pass through the wind tunnel flow and are recombined on a detector on the far side of the wind tunnel. A perturbation experienced by one of the beams (for example, when a laser-generated hot-spot passes by) but not the other can be observed by the interference of light on a high-speed detector. The system has a flat bandwidth response up to 400 kHz, with 0.1 mm spatial resolution (determined by the beam diameter) in the streamwise direction. The system can be calibrated, allowing quantitative phase shifts to be determined. However, it integrates disturbances along its optical path, so it does not provide spatial resolution along the beams.

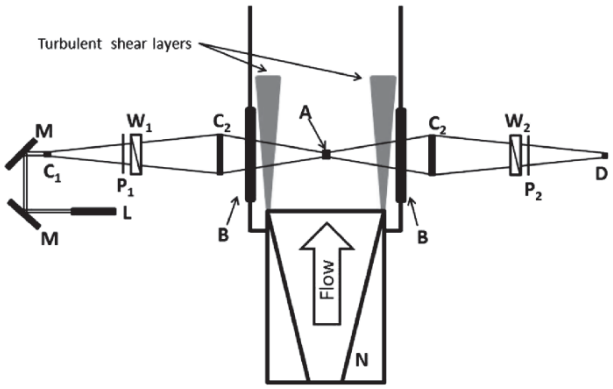

Figure 5.1. Schematic of the FLDI setup in a wind tunnel, showing the laser (L), mirror (M), lens (C), polarizer (P), Wollaston prism (W), window (B), probe volume (A), photodiode (D) and nozzle (N).[208] Reprinted with permission of the authors.

A different version[206] of LDI called focused LDI (FLDI) has recently been implemented at CalTech[207,208] for studying transitional flows. It maintains or even improves the advantages of the LDI systems mentioned above in terms of sensitivity, dynamic range and fast time response, but it has the important advantage of being able to spatially localize the measured perturbations. Whereas LDI uses two loosely focused and widely separated (~7 mm) laser beams, FLDI uses stronger focusing and closer spacing. Figure 5.1 shows the FLDI experimental setup. The Wollaston prisms have the effect of deflecting the incoming beam into two beams with perpendicular polarizations. A

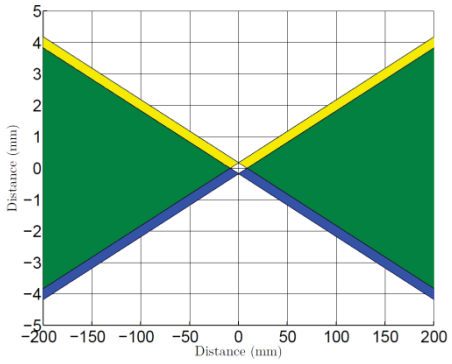

Figure 5.2. Calculated laser beam profiles at the focus of the FLDI measurement region for the two orthogonally parallel beams (one yellow and one blue, with green showing the overlapped region).[207] Reprinted with permission of the authors.

lens then directs these beams into the flow where they focus. As shown in Fig. 5.2, the two beams (one yellow and one blue), focus in two different spatial locations in the flow (because the Wollaston prism causes them to travel at slightly different angles before passing through the lens). They then diverge, pass through another lens and Wollaston prism, a polarizer, and onto a detector where the two beams interfere.

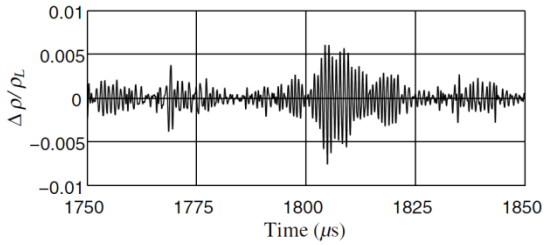

Figure 5.3. FLDI measured instability wave packet in the boundary layer of a cone.[208] Reprinted with permission of the authors.

The advantage of the FLDI technique is that, over most of the optical path, the two beams have common optical paths so that both beams experience the same disturbances. This is shown as the green region in Fig. 5.2. Thus, optical disturbances in this region (for example, wall boundary layers or disturbances elsewhere in the flow) cancel out, leaving sensitivity only to disturbances in the focus region. The resulting interference signal is then mostly sensitive to the difference in density, $\Delta\rho$, between the gas located at the two foci. Data are usually reported by referencing to the mean local density, ρ, which must be estimated. The two beams focus to a 0.1 mm diameter and are located 0.35 mm apart. The reported spatial resolution is 0.7 mm in the streamwise direction, although the system is sensitive to perturbations along the ±10 mm interaction length. The system has a 20 MHz time response, which is the highest frequency response of any measurement technique described in this manuscript. The system was used to study small disturbances on a cone, with the laser beams oriented tangent to and ~0.5 mm above the surface of a cone model, where the boundary layer was slightly larger than 1 mm thick. A typical burst originating from a wave packet travelling in the boundary layer is shown in Fig. 5.3. The strongest oscillation occurs at 1.17 MHz. The reported accuracy in measuring $\Delta\rho/\rho$ is ~30% while the precision is 0.5% in $\Delta\rho/\rho$, sufficient to resolve acoustic instabilities in the flow.[208] Limitations of this technique are its somewhat long (~20 mm) probe volume and that it is sensitive to the density difference between two closely spaced points instead of the easier-to-compute and more physically intuitive density fluctuation about the mean. Nonetheless, it is much more sensitive than the other measurement techniques reported in this manuscript.

5.3 Background Oriented Schlieren (BOS)

A relatively new measurement technique that is sensitive to density (through index of refraction gradients) is known as Background Oriented Schlieren (BOS).[209,210] BOS uses a CCD camera equipped with a lens to image a flow placed in front of a *background* consisting of a random dot pattern (or other[211,212] random pattern). A *reference* image of the background pattern is acquired with the flow absent and then a second image is acquired with the flow present. Refractive index gradients cause the dots to move slightly from one image to the other. The pair of dot pattern images is processed using particle-image velocimetry (PIV) software to

recover the path-integrated light deflections (pixel shifts) caused by the refractive index (density) gradients.

To obtain the highest possible spatial resolution, both the dot pattern and the flow disturbance should be in crisp focus. This suggests the use of small lens apertures to obtain a large depth of field. To obtain maximum sensitivity, the flow disturbance should be located as close to the camera lens as possible.[213] Since it is difficult to achieve a long enough depth of field to optimize both of these requirements, in practice, the object is usually put closer to the background dot pattern, for example from 0.5 to 0.875 of the way from the camera to the background pattern.[213, 214] Also affecting spatial resolution are the camera pixel size, the resolution and quality of the background pattern used and the interrogation window size used in image processing.

In a two-dimensional flow, the pixel shifts can be used to directly compute the density gradient and thus the density field.[213] In an axisymmetric flow, the density gradient varies along the optical path and additional processing of the data is required to make quantitative measurements. In such axisymmetric cases, an Abel or Radon inversion can be used to compute the density field, for example in the supersonic flow over a cone at zero degrees angle of attack.[215] In non-axisymmetric flows, tomography using multiple camera views is required to obtain density information.[213] The multiple views can either be obtained using a single camera that observes the flow from different angles at different times, resulting in time-averaged measurements,[213] or by using multiple cameras to take many simultaneous images, providing time resolution, which is a current research topic. Since BOS measures gradients and is thus a relative measurement technique, the density in one point in the flow must be known or estimated to obtain the density field. BOS has the advantages of being a low-cost technique and being able to provide both qualitative flow visualization and quantitative measurements for large fields of view. One disadvantage is that BOS does not produce real-time visualization and measurement results since the raw images require processing. Also, as a tomographic technique using a limited number of views, it has much lower spatial resolution than laser-sheet based techniques such planar laser induced fluorescence, at least in unsteady flow where it is impractical to have a large number of views.

5.4 Tunable Diode Laser Absorption Spectroscopy (TDLAS)

Another path-averaged measurement technique used to study supersonic and hypersonic flows is Tunable Diode Laser Absorption Spectroscopy (TDLAS).[216,217] TDLAS measurements are path-integrated, so experimental methodologies and post-processing are required if it is vital to extract spatially resolved information from the data. Though not necessarily providing spatially resolved information in all implementations of the technique, TDLAS has several advantages compared to the measurements described in prior sections. Relatively inexpensive, small, low-power lasers from the telecommunications industry can be used. These lasers can scan at very high rates, providing information at tens or hundreds of kHz,[216,217] and the lasers are

typically routed to and from the flowfield using optical fibers, simplifying the experimental setup. Technology from the telecommunications industry, such as fiber couplers and multiplexers, can be used to split the laser light into many channels and/or to combine many wavelengths into a single fiber, allowing multiple species to be probed with multiple colors along many paths through the flow. The light from the fibers is coupled into lenses, propagated across the flow and captured by lens-coupled multi-mode fibers, separated into wavelengths and directed onto detectors. Thus, different species and spectral lines can be probed at different locations in a ducted flow, for example, allowing some spatially-resolved concentration and temperature information to be determined from the line-of-sight measurements.

Recent advancements in TDLAS include systems that scan a single laser or multiple lasers spatially across the flow and from different directions to allow time averaged tomographic reconstruction of temperature and species concentrations in turbulent combusting flowfields[218] or a grid of fixed optical paths transmitting across the flow, allowing a low-resolution but time-resolved tomographic reconstruction of concentration and temperature.[219,220] Figure 5.4 (from Ref. 220) shows temperature and mole fraction maps obtained in a General Electric J85 gas turbine engine. Thirty individual laser beams—15 in the horizontal direction and 15 in the vertical direction, making a square mesh of 225 grid points—were used to probe the flow. The laser was rapidly scanned over multiple water vapor absorption lines near 1.35 μm with scans occurring at a rate of 50 kHz. While the smaller turbulent length (and time) scales of the flow are not resolved with this system, the large-scale spatial (and temporal) distribution of the temperature and mole fraction are resolved.

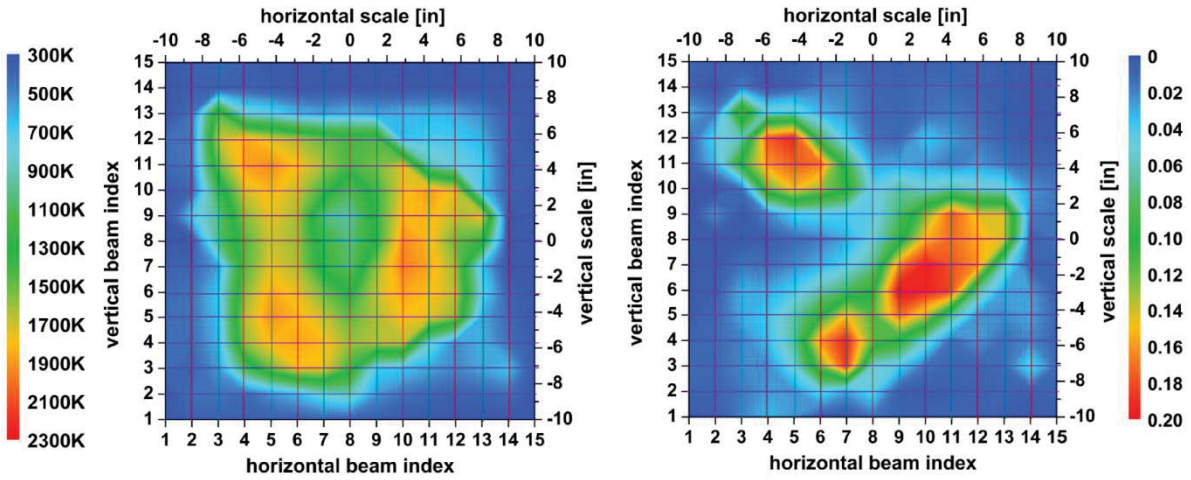

Figure 5.4. Temperature (left) and water vapor mole fraction (right) measured at the exit of a General Electric J85 engine, with 50 kHz diode laser tomography, adapted from Ref. 220. The paper online has links to play animated movie clips of these data. Reprinted with permission of the authors and publisher.

5.5 Degenerate Four-Wave Mixing (DFWM)

Like CARS, Degenerate Four-Wave Mixing (DFWM) is a nonlinear, four-wave mixing measurement technique that involves the crossing of three laser beams to generate a fourth beam that is detected. DFWM's three input laser beams are all of the same color (degenerate) and are usually tuned to an absorption in the atom or molecule being probed. The signal beam from DFWM measurements is typically analyzed in the spectral domain using scanned or broadband lasers to measure a spectrum of signal intensity versus wavelength. DFWM has been used to measure gas concentration, temperature and velocity.[42] Compared to LIF, it has an advantage for measuring species concentrations because it is relatively insensitive to collisional quenching, owing to the fact that it is an absorption-based technique (not depending on fluorescence).[221] Since each beam is resonant, it is also relatively sensitive and can be used for detecting minor species. [42] Since the DFWM signal is a laser-like beam, it is suitable for studying luminous flows since background radiation can be spatially filtered with an aperture. DFWM is usually implemented as a single-point measurement, though it has been extended to line and 2D imaging applications. [42] The main drawbacks of DFWM are that it is more difficult to align and implement than LIF, it has much lower spatial resolution than LIF (because of its elongated probe volume), it is sensitive to absorption of the laser beams, it is sensitive to saturation of the molecular transitions, and it requires very high beam quality to obtain 2D images.[42] DFWM temperature measurements in a flame have reported accuracies and precisions more than a factor of two worse than CARS[222,42] while also having a larger probe volume.

5.6 Laser Induced Thermal Acoustics (LITA)

Another four-wave mixing technique, laser induced thermal acoustics (LITA), uses two pump beams to generate acoustic waves that scatter a probe laser into a signal beam that is detected.[223] The two pumps and probe can be the same wavelengths, in which case it is also DFWM. Or, the probe beam can be a different wavelength than the pumps, which reduces light interferences from the incident, high-powered pump beams. Whereas the signal beam from the DFWM techniques described in the previous section is usually analyzed in the *spectral* domain, LITA usually uses the *time* domain (signal beam intensity versus time) to measure gas velocity, speed of sound (which can be converted to temperature if the gas composition is known)[223,224] and gas pressure.[225] In the time domain, the signal intensity is characterized by a damped oscillation, which can have beat frequencies containing the velocity and temperature information. Velocity and temperature accuracies and precisions on the order of 1 m/s and 1 K, respectively, have been reported in air flows.[224,226] These accuracies and precisions are the best reported in this manuscript for these parameters. LITA is usually implemented as a single-point, single-velocity-component measurement. The main limitations of LITA are its relative complexity and that the measurements are obtained over relatively long probe volumes – on the order of 1 to 2 cm – which is much longer than most transitional and turbulent length scales occurring in high speed flows. Since the technique is a nonlinear technique, the resulting measurements are not simple averages over the probe volume. Instead, as with CARS, there is a

nonlinear bias that skews the averaging towards higher gas density (lower temperature) regions[227] which complicates interpretation of the measurements. This problem is more severe for LITA, which typically has a probe volume ~10x longer than CARS.

6. Conclusion

This manuscript has described numerous molecular-based measurement techniques that are potentially applicable to the investigation of high-speed transitional and/or turbulent flows. One might ask, *"Which technique is best?"* or *"Which one should I use?"* The answer to the first question is that none is best. The different techniques measure different properties in different ways and have relative merits. The answer to the second, more important question depends on many factors. It depends on the measurement requirements as well as the past experience of the research team. It depends on the available equipment, the budget for new equipment and the time frame available to do the measurement. Some techniques, such as CARS, require a year or years of training to learn well enough to apply the technique expertly. Dual-pump CARS requires home-built equipment (i.e. a broadband dye laser) as well as two commercially available lasers, a spectrometer, a low noise CCD camera, and other equipment. It is therefore relatively time consuming and expensive to set up. If a researcher or research team has experience with similar technology (for example Nd:YAG lasers, dye lasers, CCD cameras), then the work will progress faster. Less complicated (easier to set up and to understand) methods might yield usable results in a shorter time frame. These practical issues are certainly important, but a major consideration in planning an experiment is the measurement requirements.

A measurement campaign should begin with an interview of the customer for whom the data is being acquired. Answers to the following questions need to be obtained:

- What parameter(s) need to be measured?
- Must multiple parameters be obtained simultaneously to determine correlations?
- What spatial resolution is required?
- Is imaging required or are single-point or line measurements sufficient?
- What temporal resolution is required? (e.g. time required for a single measurement)
- Do measurements need to be time resolved? (e.g. a continuous sequence of data)
- What accuracy is needed?
- What precision is needed?
- What quantity of data is required?
- When is the data needed? Is instant (real-time) data required?
- Where in the flow are measurements required? (inflow, exit, near walls, etc.)
- What type of optical access is available?
- Can (toxic) seed gases be introduced? Will they influence the properties being measured?
- What is the ordered priority of the above requirements?

This list of requirements must be matched up with available measurement technologies such as those reported in the sections above. There is rarely a perfect solution for this exercise. Instead, there is a compromise between the needs of the customer and the capabilities of the instrumentation team. A common set of goals should then be established and agreed upon before the research actually starts. This exercise is fruitful for the measurement scientist because it often results in a need for a new measurement technique that can be developed if existing techniques are not suitable.

In the case of measurements of transitional flows, the precision, time resolution, acquisition rate, and spatial resolution requirements are all important factors. Considering only the precision requirement, we see from Table 1.1 that freestream perturbations in quiet wind tunnels are on the order of 0.01% - 0.2%. Even the most sensitive technique reported herein, FLDI, which can measure gas density with a precision of 0.5%,[207] lacks the sensitivity to monitor quiet tunnel freestream disturbances (although it is possible that this instrument could be optimized or improved to make such measurements). LITA, which has a demonstrated single-shot precision of ~1 m/s[226] could potentially measure these fluctuations. From Table 1.1, it can be seen that conventional tunnels have larger fluctuations, typically on the order of a percent. But to measure these fluctuations, sub-percent precision is required. FLDI and possibly LITA would appear to be appropriate measurement techniques in these applications, but most of the other techniques reviewed herein are insufficient as far as resolving fluctuations is concerned.

From Table 1.2, the fluctuations in the transitional flow downstream of discrete roughness on a flat plate are much higher – on the order of tens of percent. Turbulent boundary layer flow (also shown in Table 1.2) also shows tens-of-percent fluctuations. To resolve these fluctuations, techniques with precisions on the order of a few percent are suitable. Several of the techniques described herein are suitable for this application, for example Rayleigh scattering, LIF molecular tagging velocimetry, and CARS thermometry, all of which have precisions around a few percent. Still other techniques have precisions that are so poor that they cannot even resolve turbulent fluctuations. These techniques still may be useful or measuring mean quantities in turbulent flowfields.

Nonetheless, measurement precision is not the only requirement: spatial resolution and other factors must be taken into consideration. For example, though LITA may be precise enough to measure freestream perturbations in conventional wind tunnels, it is possible that the 1 cm long probe volume may be too large to observe small-scale flow structures. Also, LITA uses high-powered lasers and has usually been implemented at a rate of ~10 Hz, which is far too slow to provide time-sequence data that may be required in some applications. Turbulent flows, by definition, have a wide range of length scales. Many of the measurement techniques described herein may be able to resolve the larger length scales, but great care must be taken in order to resolve the smallest structures. Even if only larger turbulence length scale data is obtained, the data can be of value to the high-speed turbulence research community, especially since very little

experimental data (both mean and, particularly, fluctuating) have been obtained in the hypersonic regime.[40]

Clearly, more sensitive (higher precision) measurement techniques are needed to study transition and turbulence in high speed flows. It is also desired to make the measurements simpler and easier to understand, to set up, and to use. Higher repetition rate and higher accuracy methods are also needed. Since no single technique can measure every parameter of interest with uncertainties that meet all requirements, combining existing instruments together is a possible method for meeting more requirements. For example, CARS/Rayleigh[228] has been used for temperature, major species concentrations and velocity in unseeded supersonic combusting flows, Raman/Rayleigh/LIF[91] for major and minor species concentrations and temperature in turbulent combusting flows, and CARS/LDV[229] for temperature and velocity in particle-seeded combustion flows. However, performing multiple measurements simultaneously brings additional complexity, and compromises often must be made between the different technologies. An alternate approach is to extend the capabilities of an existing technique to measure more parameters. For example, Tedder et al. used WIDECARS to extend the dual-pump CARS technique to measure additional species.[230]

With continued research, molecular-based instrumentation for studying high-speed transitional and turbulent flows will continue to improve in its specific capabilities (e.g., precision, accuracy, spatial and temporal resolution), as well as in ease of implementation. Close collaboration with customers will help define research goals. Ultimately, the use of molecular-based diagnostic techniques will provide data to help validate computational codes as well as to help understand the complex fluid physics of high-speed unsteady flows.

Acknowledgements

The authors wish to thank Jennifer Inman and Joel Everhart of NASA Langley Research Center and Christopher Combs from the University of Texas at Austin for assistance in reviewing this manuscript. The authors acknowledge support from the NASA Fundamental Aeronautics Program, Hypersonics and High Speed Projects. Dr. Cutler received support from the National Center for Hypersonic Combined Cycle Propulsion grant FA 9550-09-1-0611. The technical monitors on the grant are Chiping Li (AFOSR), and Aaron Auslender and Rick Gaffney (NASA).

References

1 E. Reshotko, "*Transition Issues for Atmospheric Entry*," Journal of Spacecraft and Rockets, 45(2), pp. 161-164, March-April, 2008.

2 L. S. G Kovasznay "*Turbulence in Supersonic Flow*," Journal of the Aeronautical Sciences, 20(10), pp. 657-682, October, 1953.

[3] M. V. Morkovin, "*On Transition Experiments at Moderate Supersonic Speeds*," Journal of the Aeronautical Sciences, 24(7), pp. 480-486, July, 1957.

[4] M. V. Morkovin, "*On Supersonic Wind Tunnels With Low Free-Stream Disturbances*," Journal of Applied Mechanics, 26(3), pp. 319-324, September, 1959.

[5] S. P. Schneider, "*Development of Hypersonic Quiet Tunnels*," Journal of Spacecraft and Rockets, 45(4), pp. 641-664, July-August, 2008.

[6] S. P. Schneider, "*Effects of High-Speed Tunnel Noise on Laminar-Turbulent Transition*," Journal of Spacecraft and Rockets, 38(3), pp. 323-333, May-June, 2001.

[7] I. E. Beckwith, and C. G. Miller III, "*Aerothermodynamics and transition in high-speed wind tunnels at NASA Langley*," Annual Review of Fluid Mechanics, 22, pp. 419-439, 1990.

[8] S. R. Pate, C. J. Schueler, "*Radiated Aerodynamic Noise Effects on Boundary-Layer Transition in Supersonic and Hypersonic Wind Tunnels*," AIAA Journal, 7(3), pp. 450-457, March, 1969.

[9] S. R. Pate, "*Measurements and Correlations of Transition Reynolds Numbers on Sharp Slender Cones at High Speeds*," AIAA Journal, 9(6), pp. 1082-1090, June, 1971.

[10] S. J. Rufer, and D. C. Berridge, "*Pressure Fluctuation Measurements in the NASA Langley 20-Inch Mach 6 Wind Tunnel*," 42nd AIAA Fluid Dynamics Conference, AIAA 2012-3262, New Orleans, LA., June 25-28, 2012.

[11] N. Chokani, A. N. Shiplyuk, A. A. Sidorenko, and C. B. McGinley, "*Comparison between a hybrid constant-temperature anemometer and constant-voltage anemometer in hypersonic flow*," 34th AIAA Fluid Dynamics Conference, AIAA 2004-2248, Portland, OR. June 28 – July 1, 2004.

[12] D. Masutti, E. Spinosa, O. Chazot, and M. Carbonaro, "*Disturbance Level Characterization of a Hypersonic Blowdown Facility*," AIAA Journal, 50(12), pp. 2720-2730, December, 2012.

[13] B. M. Wheaton, and S. P. Schneider, "*Roughness-Induced Instability in a Hypersonic Laminar Boundary Layer*," AIAA Journal, 50(6), pp. 1245-1256, June, 2012.

[14] L. E. Steen, *Characterization and Development of Nozzles for a Hypersonic Quiet Wind Tunnel*, Master's Thesis, Purdue University, December, 2010.

[15] D. Masutti, E. Spinosa, O. Chazot, and M. Carbonaro, "Disturbance Level Characterization of a Hypersonic Blowdown Facility," AIAA Journal, 50(12), December, 2012.

[16] N. Chokani, A. N. Shiplyuk, A. A. Sidorenko, and C. B. McGinley, "Comparison between a hybrid constant-current anemometer and constant-voltage anemometer in hypersonic flow," 34th AIAA Fluid Dynamics Conference, AIAA 2004-2248, Portland, OR., June 28 - July 1, 2004.

[17] S. J. Rufer, and D. C. Berridge, "Pressure Fluctuation Measurements in the NASA Langley 20-Inch Mach 6 Wind Tunnel," 42nd AIAA Fluid Dynamics Conference, AIAA 2012-3262, New Orleans, LA, June 25-28, 2012.

[18] L. E. Steen, Characterization and Development of Nozzles for a Hypersonic Quiet Wind Tunnel, Master's Thesis, Purdue University, December, 2010.

[19] S. A. Berry, and T. J. Horvath "*Discrete Roughness Transition for Hypersonic Flight Vehicles*," 45th AIAA Aerospace Sciences Meeting, AIAA 2007-307, Reno, NV, January 8-11, 2007.

[20] S. A. Berry, T. J. Horvath, R. P. Lillard, B. S. Kirk, and A. M. Cassady, "*Aerothermal Testing for Project Orion Crew Exploration Vehicle*," 41st AIAA Thermophysics Conference, AIAA 2009-3842, San Antonio, TX., June 22-25, 2009.

[21] J. L. Everhart, "*Supersonic/Hypersonic Laminar Heating Correlations for Rectangular and Impact-Induced Open and Closed Cavities*," Journal of Spacecraft and Rockets, 46(3), pp. 545-560, May-June, 2009.

[22] D. S. Liechty, "*Aerothermodynamic Testing of Protuberances and Penetrations on the NASA Crew Exploration Vehicle Heat Shield*," 46th AIAA Aerospace Sciences Meeting, AIAA 2008-1240, Reno, NV, January 7-10, 2008.

[23] S. P. Schneider, "*Effects of Roughness on Hypersonic Boundary-Layer Transition*," Journal of Spacecraft and Rockets, 45(2), pp. 193-209, March –April 2008.

[24] D. C. Reda, "*Review and Synthesis of Roughness-Dominated Transition Correlations for Reentry Applications*," Journal of Spacecraft and Rockets, 39(2), p. 161-167, March-April, 2002.

[25] E. Reshotko, "*Roughness-Induced Transition, Experiment and Modeling*," 38th AIAA Fluid Dynamics Conference, AIAA 2008-4294, Seattle, WA., June 23-26, 2008.

[26] C-L. Chang, M. M. Choudhari, and F. Li, "Numerical Computations of Hypersonic Boundary-Layer over Surface Irregularities," 48th AIAA Aerospace Sciences Meeting, AIAA 2010-1572, Orlando, FL., January 4-7, 2010.

[27] L. Duan, I. Beekman, and M. P. Martín, "*Direct numerical simulation of hypersonic turbulent boundary layers. Part 3. Effect of Mach number*," Journal of Fluid Mechanics, 672, pp. 245-267, 2011.

[28] R. A. Heinrich, M. Choudhari, and E. J. Kerschen, "*A comparison of boundary layer receptivity mechanisms*," AIAA, SIAM, and APS, National Fluid Dynamics Congress, 1, pp. 1273-1280, 1988.

[29] L. M. Mack, "*Linear Stability Theory and the Problem of Supersonic Boundary-Layer Transition*," AIAA Journal, 13(3), pp. 278-289, March, 1975.

[30] L. M. Mack, "*Boundary-Layer Linear Instability Theory*," AGARD Report 709, pp. 3-1 – 3-81, 1984.

[31] E. Reshotko, "*Boundary Layer Instability, Transition, and Control*," 32nd AIAA Aerospace Sciences Meeting, AIAA 1994-1, Reno, NV., January 10-13, 1994.

[32] H. L. Reed, and W. S. Saric, "*Linear Stability Theory Applied to Boundary Layers*," Annual Review of Fluid Mechanics, 28(1), pp. 389-428, 1996.

[33] E. Reshotko, "*Transient growth: A factor in bypass transition*," Physics of Fluids, 13(5), pp. 1067-1075, May, 2001.

[34] A. Federov, A., "*Transition and Stability of High-Speed Boundary Layers*," Annual Review of Fluid Mechanics, 43, pp. 79-95, 2011.

[35] W. S. Saric, H. L. Reed, and E. J. Kerschen, "*Boundary-Layer Receptivity to Freestream Disturbances*," Annual Review of Fluid Mechanics, 34(1), pp. 291-319, 2002.

[36] J. M. Kendall, "*Experiments on Boundary-Layer Receptivity to Freestream Turbulence*," 36th AIAA Aerospace Sciences Meeting, AIAA 1998-530, 1998.

[37] S. H. Collicott, S. P. Schneider, and N. L. Messersmith, "*Review of Optical Diagnostic Methods for Hypersonic Low-Noise Facilities*," 34th AIAA Aerospace Sciences Meeting, AIAA 1996-0851, Reno, NV., January 15-18, 1996.

[38] J. M. Kendall, "*Wind Tunnel Experiments Relating to Supersonic and Hypersonic Boundary-Layer Transition*," AIAA Journal, 13(3), pp. 290-299, March, 1975.

[39] T. B. Gatski, and J. P. Bonnet, "Compressibility, turbulence and high speed flow." Academic Press, 2nd Ed., 2013.

[40] A. J. Smits, M.P. Martin, and S. Girimaji, "Current Status of Basic Research in Hypersonic Turbulence," 47th AIAA Aerospace Sciences Meeting, AIAA 2009-151, Orlando, FL, January 5-8, 2009.

[41] J. Slotnick, A. Khodadoust, J. Alonso, D. Darmofal, W. Gropp, E. Lurie, D. Mavriplis, "Summary of the Vision 2030 CFD Survey, NASA Vision 2030 CFD Code," Contract NNL08AA16B, Task NNL12AD05T. Prepared for NASA Langley Research Center, Hampton, Virginia 23681-2199, March 29, 2013.

[42] A. C. Eckbreth, *Laser Diagnostics for Combustion Temperature and Species 2nd Ed*., Combustion Science & Technology Book Series, Volume 3, Taylor & Francis, New York, 1996.

[43] K. Kohse-Höinghaus, and J. B. Jeffries, eds., *Applied Combustion Diagnostics*, Combustion: An International Series, Taylor & Francis, New York, 2002.

[44] P. C. Palma, *Laser-Induced Fluorescence Imaging in Free-Piston Shock Tunnels*, PhD Thesis, Australian National University, submitted May 1998, revised February 1999.

[45] B. A. E. Saleh, and M. C. Teich, *Fundamentals of Photonics 2nd Ed*., John Wiley & Sons, Inc., Hoboken, New Jersey, 2007.

[46] J. Humlíček, "*An efficient method for the evaluation of the complex probability function: The Voigt function and its derivatives*," Journal of Quantitative Spectroscopy and Radiative Transfer, 21, pp. 309-313, 1979.

[47] M. Kuntz, "*A new implementation of the Humlicek algorithm for the calculation of the Voigt profile function*," Journal of Quantitative Spectroscopy and Radiative Transfer, 57(6), pp. 819-824, 1997.

[48] W. Ruyten, "*Comment on "A new implementation of the Humlicek algorithm for the calculation of the Voigt profile function" by M. Kuntz [JQSRT 57(6) (1997) 819-824]*," Journal of Quantitative Spectroscopy and Radiative Transfer, 86, pp. 231-233, 2004.

[49] Thorne, A., Litzén, U., and Johansson, S., *Spectrophysics: Principles and Applications*, Berlin Heidelberg, 1999.

[50] W. K. Bischel, P. J. Kelly, and C. K. Rhodes, "*High-resolution Doppler-free two-photon spectroscopic studies of molecules. I. The v_3 bands of $^{12}CH_3F$*," Physical Review A, 13(5), 1976.

[51] T. J. McIlrath, R. Hudson, A. Aikin, and T. D. Wilkerson, "*Two-photon lidar technique for remote sensing of atomic oxygen*," Applied Optics, 18(3), 1979.

[52] W. K. Bischel, B. E. Perry, and D. R. Crosley, "*Detection of fluorescence from O and N atoms induced by two-photon absorption*," Applied Optics, 21(8), 1982.

[53] U. Meier, J. Bittner, K. Kohse-Höinghaus, and Th. Just, "*Discussion of two-photon laser-excited fluorescence as a method for quantitative detection of oxygen atoms in flames*," 22nd Symposium (International) on Combustion, The Combustion Institute, 1988.

[54] D. R. Crosley, "*Rotational and Translational Effects in Collisions of Electronically Excited Diatomic Hydrides*," Journal of Physical Chemistry, 1989, 93, 6273 – 6282.

[55] J. D. Anderson Jr., *Hypersonic and High-Temperature Gas Dynamics 2nd ed.*, AIAA Education Series, AIAA, Reston, VA, 2006.

[56] W. G. Vincenti, and C. H. Kruger Jr., *Introduction to Physical Gas Dynamics*, Reprint of 1967 ed., Wiley, New York, 1975.

[57] P. H. Paul, J. A. Gray, J. L. Durant, J. W. Thoman, "*Collisional Quenching Corrections for Laser-Induced Fluorescence Measurements of NO $A^2\Sigma^+$*," AIAA Journal, 32(8), August 1994.

[58] D. S. Baer, H. A. Chang, and R. K. Hanson, "*Fluorescence diagnostics for atmospheric-pressure plasmas using semiconductor lasers*," Journal of the Optical Society of America B, 9(11), pp. 1968-1978, November, 1992.

[59] J. G. Liebeskind, R. K. Hanson, and M. A. Cappelli, "*Laser-induced fluorescence diagnostic for temperature and velocity measurements in a hydrogen arcjet plume*," Applied Optics, 32(30), pp. 6117-6127, October 20, 1993.

[60] J. A. Inman, B. F. Bathel, C. T. Johansen, P. M. Danehy, S. B. Jones, J. G. Gragg, and S. C. Splinter, "*Nitric Oxide PLIF Measurements in the Hypersonic Materials Environmental Test System (HYMETS)*," 49th AIAA Aerospace Sciences Meeting, AIAA Paper 2011-1090, Orlando, FL, January 4-7, 2011.

[61] P. V. Storm, and M. A. Cappelli, "*LIF Characterization of Arcjet Nozzle Flows*," AIAA, ASME, SAE, and ASEE, Joint Propulsion Conference, AIAA Paper 1996-2987, Lake Buena Vista, FL, July 1 – 3, 1996.

[62] D. G. Fletcher, "*Arcjet flow properties determined from laser-induced fluorescence of atomic nitrogen*," 36th AIAA Aerospace Sciences Meeting, AIAA Paper 1998-0205.

[63] D. G. Fletcher, "*Arcjet flow properties determined from laser-induced fluorescence of atomic nitrogen*," Applied Optics, 38(9), March 20, 1999.

[64] J. H. Grinstead, B. J. Porter, and J. E. Carballo, "*Flow Property Measurement Using Laser-Induced Fluorescence in the NASA Ames Interaction Heating Facility*," 49th AIAA Aerospace Sciences Meeting, AIAA Paper 2011-1091, Orlando, FL., January 4 – 7, 2011.

[65] A. Lutz, J. Meyers, W. Owens, S. Smith, and D. G. Fletcher, "*Experimental Analysis of Carbon Nitridation and Oxidation Efficiency with Laser-Induced Fluorescence*," 51st AIAA Aerospace Sciences Meeting, AIAA Paper 2013-0924, Grapevine, TX., January 7 – 10, 2013.

[66] R. L. McKenzie, and K. P. Gross, "*Two-photon excitation of nitric oxide fluorescence as a temperature indicator in unsteady gasdynamic processes*," Applied Optics, 20(12), June 15, 1981.

[67] B. K. McMillin, J. L. Palmer, and R. K. Hanson, "*Temporally resolved, two-line fluorescence imaging of NO temperature in a transverse jet in a supersonic cross flow*," Applied Optics, 32(36), December, 20, 1993.

[68] J. M. Seitzman, R. K. Hanson, P. A. DeBarber, and C. F. Hess, "*Application of quantitative two-line OH planar laser-induced fluorescence for temporally resolved planar thermometry in reacting flows*," Applied Optics, 33(18), June 20, 1994.

[69] B. K. McMillin, J. M. Seitzman, and R. K. Hanson, "*Comparison of NO and OH Planar Fluorescence Temperature Measurements in Scramjet Model Flowfields*," AIAA Journal, 32(10), October 1994.

[70] P. C. Palma, P. M. Danehy, and A. F. P. Houwing, "*Fluorescence Imaging of Rotational and Vibrational Temperature in Shock-Tunnel Nozzle Flow*," AIAA Journal, 41(9), September 2003.

[71] E. R. Lachney, and N. T. Clemens, "*PLIF imaging of mean temperature and pressure in a supersonic bluff wake*," Experiments in Fluids, 24, pp. 354-363, 1998.

[72] U. Koch, A. Gülhan, and B. Esser, "*Determination of NO-rotational and vibrational temperature profiles in a high enthalpy flow field with nonequilibrium*," 1st Joint French-German Symposium on Simulation of Atmospheric Entries by Means of Ground Test Facilities, Stuttgart, Germany, 1999.

[73] A. Del Vecchio, G. Palumbo, U. Koch, and A. Gülhan, "*Temperature Measurements by Laser-induced Fluorescence Spectroscopy in Nonequilibrium High-Enthalpy Flow*," Journal of Spacecraft and Rockets, 14(2), April-June 2000.

[74] S. Löhle, M. Auweter-Kurtz, G. Herdrich, and T. Laux, "*LIF Measurements of NO in N_2/O_2 and N_2/CO_2 Plasma Flows*," 36th AIAA Thermophysics Conference, AIAA Paper 2003-3487, Orlando, FL., June 23-26, 2003.

[75] E. A. Brinkman, G. A. Raiche, M. S. Brown, and J. B. Jeffries, "*Optical diagnostics for temperature measurement in a DC arcjet reactor used for diamond deposition*," Applied Physics B, 64(6), pp. 689-697, 1997.

[76] W. G. Bessler, and C. Schulz, "*Quantitative multi-line NO-LIF temperature imaging*," Applied Physics B, 78, pp. 519-533, 2004.

[77] J. L. Palmer, and R. K. Hanson, "*Planar laser-induced fluorescence temperature measurements in free jet flows with vibrational nonequilibrium*," 31st AIAA Aerospace Sciences Meeting, AIAA Paper 1993-0046, Reno, NV., January 11-14, 1993.

[78] H. Katô, and M. Baba, "*Dynamics of Excited Molecules: Predissociation*," Chemical Review, 95, pp. 2311-2349, 1995.

[79] G. Herzberg, "*Molecular Spectra and Molecular Structure: I. Spectra of Diatomic Molecules"*, New York, Van Nostrand Reinhold, 1950.

[80] G. Laufer, T. M. Quagliaroli, R. H. Krauss, R. B. Whitehurst III, J. C. McDaniel, and J. H. Grinstead, "*Planar OH Density and Apparent Temperature Measurements in a Supersonic Combusting Flow*," AIAA Journal, 34(3), March 1996.

[81] J. Zhang, G. B. King, N. M. Laurendeau, and M. W. Renfro, "*Two-point time-series measurements of hydroxyl concentration in a turbulent nonpremixed flame*," Applied Optics, 46(23), August 10, 2007.

[82] T. B. Settersten, B. D. Patterson, and W. H. Humphries, "*Radiative lifetimes of NO $A^2\Sigma^+(v'=0,1,2)$ and the electronic transition moment of the $A^2\Sigma^+$-$X^2\Pi$ system*," Journal of Chemical Physics, 131, 2009.

[83] T. B. Settersten, B. D. Patterson, and J. A. Gray, "*Temperature- and species-dependent quenching of NO $A^2\Sigma^+(v'=0)$ probed by two-photon laser-induced fluorescence using a picosecond laser*," Journal of Chemical Physics, 124, 2006.

[84] T. B. Settersten, B. D. Patterson, and C. D. Carter, "*Collisional quenching of NO $A^2\Sigma^+(v'=0)$ between 125 and 294 K*," Journal of Chemical Physics, 130, 2009.

[85] J. H. Grinstead, D. M. Driver, and G. A. Raiche, "*Radial profiles of arcjet flow properties measured with laser-induced fluorescence of atomic nitrogen*," 41st AIAA Aerospace Sciences Meeting, AIAA 2003-400, Reno, NV., January 6-9, 2003.

[86] D. G. Fletcher, and M. Playez, "*Characterization of supersonic and subsonic plasma flows*," 25th AIAA Aerodynamic Measurement Technology and Ground Testing Conference, AIAA 2006-3294, San Francisco, CA., June 5-8, 2006.

[87] B. J. Lochman, Z. R. Murphree, V. Narayanaswamy, and N. T. Clemens, "*PLIF imaging of naphthalene-ablation products in a Mach 5 turbulent boundary layer*," 27th AIAA Aerodynamic Measurement Technology and Ground Testing Conference, AIAA 2010-4346, Chicago, IL., June 28 – July 1, 2010.

[88] O. R. H. Buxton, B. J. Lochman, M. Sharma, and N. T. Clemens, "*Simultaneous PIV and PLIF Imaging of Low-Temperature Ablation in a Mach 5 Turbulent Boundary Layer*," 50th AIAA Aerospace Sciences Meeting, AIAA 2012-440, Nashville, TN., January 9-12, 2012.

[89] M. Versluis, Georgiev, L. Martinsson, M. Aldėn, and S. Kröll, "*2-D absolute OH concentration profiles in atmospheric flames using planar LIF in a bi-directional laser beam configuration*," Applied Physics B, 65, pp. 411-417, 1997.

[90] C. D. Carter, and R. S. Barlow, "*Simultaneous measurements of NO, OH, and the major species in turbulent flames*," Optics Letters, 19(4), pp. 299-301, February 15, 1994.

[91] R. S. Barlow, G.-H. Wang, P. Anselmo-Filho, M. S. Sweeney, and S. Hochgreb, "*Application of Raman/Rayleigh/LIF diagnostics in turbulent stratified flames*," Proceedings of the Combustion Institute, 32, pp. 945-953, 2009.

[92] W. J. Marinelli, W. J. Kessler, M. G. Allen, S. J. Davis, S. Arepalli, and C. D. Scott, "*Copper atom based measurements of velocity and turbulence in arc jet flows*," 29th Aerospace Sciences Meeting, AIAA 1991-358, Reno, NV., January 7-10, 1991.

[93] J. C. McDaniel, B. Hiller, and R. K. Hanson, "*Simultaneous multiple-point velocity measurements using laser-induced iodine fluorescence*," Optics Letters, 8(1), pp. 51-53, January 1983.

[94] A. Y. Chang, B. E. Battles, and R. K. Hanson, "*Simultaneous measurements of velocity, temperature, and pressure using rapid cw wavelength-modulation laser-induced fluorescence of OH*," Optics Letters, 15(12), June 15, 1990.

[95] K. G. Klavuhn, G. Gauba, and J. C. McDaniel, "*OH Laser-Induced Fluorescence Velocimetry Technique for Steady, High-Speed, Reacting Flows*," Journal of Propulsion and Power, 10(6), 1994.

[96] W. D. Kulatilaka, S. V. Naik, and R. P. Lucht, "*Development of High-Spectral-Resolution Planar Laser-Induced Fluorescence Imaging Diagnostics for High-Speed Gas Flows*," AIAA Journal, 46(1), January 2008.

[97] S. V. Naik, W. D. Kulatilaka, K. K. Venkatesan, and R. P. Lucht, "*Pressure, Temperature, and Velocity Measurements in Underexpanded Jets Using Laser-Induced Fluorescence Imaging*," AIAA Journal, 47(4), April 2009.

[98] P. M. Danehy, P. Mere, M. J. Gaston, S. O'Bryne, P. C. Palma, A. F. P. and Houwing, "*Fluorescence velocimetry of the hypersonic, separated flow over a cone,*" AIAA Journal, 39(7), pp. 1320-1328, 2001.

[99] R. Hruschka, S. O'Byrne, and H. Kleine, "*Two-component Doppler-shift fluorescence velocimetry applied to a generic planetary entry probe model*," Experiments in Fluids, 48, pp. 1109-1120, 2010.

[100] D. G. Fletcher, and J. C. McDaniel, "*Laser-Induced Iodine Fluorescence Technique for Quantitative Measurement in a Nonreacting Supersonic Combustor*," AIAA Journal, 27(5), May 1989.

[101] R. J. Hartfield, S. D. Hollo, and J. C. McDaniel, "*Planar Measurement Technique for Compressible Flows Using Laser-Induced Iodine Fluorescence*," AIAA Journal, 31(3), March 1993.

[102] J. M. Donohue, and J. C. McDaniel, "*Computer-Controlled Multiparameter Flowfield Measurements Using Planar Laser-Induced Iodine Fluorescence*," AIAA Journal, 34(8), August 1996.

[103] M. Zimmerman, and R. B. Miles, "*Hypersonic-helium-flow-field measurements with the resonant Doppler velocimeter*," Applied Physics Letters, 37(10), November 15, 1980.

[104] B. F. Bathel, C. Johansen, J. A. Inman, S. B. Jones, and P. M. Danehy, "*Review of Fluorescence-Based Velocimetry Techniques to Study High-Speed Compressible Flows*,"AIAA 2013-0339, 51st AIAA Aerospace Sciences Meeting, Grapevine, TX, January 7-10, 2013.

[105] B. Hiller, and R. K. Hanson, "*Two-frequency laser-induced fluorescence technique for rapid velocity-field measurements in gas flows*," Optics Letters, 10(5), May, 1985.

[106] B. Hiller, and R. K. Hanson, "*Simultaneous planar measurements of velocity and pressure fields in gas flows using laser-induced fluorescence*," Applied Optics, 27(1), January 1, 1988.

[107] U. Westblom, and M. Aldėn, "*Spatially resolved flow velocity measurements using laser-induced fluorescence from a pulsed laser*," Optics Letters, 14(1), January 1, 1989.

[108] P. H. Paul, M. P. Lee, and R. K. Hanson, "*Molecular velocity imaging of supersonic flows using pulsed planar laser-induced fluorescence of NO*," Optics Letters, 14(9), May 1, 1989.

[109] M. Allen, S. Davis, W. Kessler, H. Legner, K. McManus, P. Mulhall, T. Parker, and D. Sonnenfroh, "*Velocity Field Imaging in Supersonic Reacting Flows near Atmospheric Pressure*," AIAA Journal, 32(8), August 1994.

[110] M. M. Koochesfahani, and D. G. Nocera, *"Molecular Tagging Velocimetry*," *Handbook of Experimental Fluid Dynamics*, Chap. 5.4, edited by J. Foss, C. Tropea, and A. Yarin, Springer-Verlag, Berlin, 2007.

[111] B. Hiller, R. A. Booman, C. Hassa, and R. K. Hanson, "*Velocity Visualization in Gas Flows Using Laser-Induced Phosphorescence of Biacetyle*," Review of Scientific Instruments, 55(12), pp. 1964-1967, December, 1984.

[112] P. M. Danehy, S. O'Byrne, A. F. P. Houwing, J. S. Fox, and D. R. Smith, "*Flow-Tagging Velocimetry for Hypersonic Flows Using Fluorescence of Nitric Oxide*," AIAA Journal, 41(2), February 2003.

[113] B. F. Bathel, P. M. Danehy, J. A. Inman, S. B. Jones, C. B. Ivey, C. P, and Goyne, "*Velocity Profile Measurements in Hypersonic Flows Using Sequentially Imaged Fluorescence-Based Molecular Tagging*," AIAA Journal, 49(9), September 2011.

[114] W. R. Lempert, N. Jiang, S. Sethuram, and M. Samimy, "*Molecular Tagging Velocimetry Measurements in Supersonic Microjets*," AIAA Journal, 40(6), June, 2002.

[115] W. R. Lempert, M. Boehm, N. Jiang, S. Gimelshein, and D. Levin, "*Comparison of molecular tagging velocimetry data and direct simulation Monte Carlo simulations in supersonic micro jet flows*," Experiments in Fluids, 34, pp. 403-411, 2003.

[116] A. G. Hsu, R. Srinivasan, R. D. W. Bowersox, and S. W. North, "*Two-component molecular tagging velocimetry utilizing NO fluorescence lifetime and NO_2 photodissociation techniques in an underexpanded jet flowfield*," Applied Optics, 48(22), August 1, 2009.

[117] J. A. Inman, P. M. Danehy, B. F. Bathel, D. W. Alderfer, and R. J. Nowak, "*Laser-Induced Fluorescence Velocity Measurements in Supersonic Underexpanded Impinging Jets*," 48th AIAA Aerospace Sciences Meeting, AIAA 2010-1438, Orlando, FL., January 4-7, 2010.

[118] C. T. Johansen, P. M. Danehy, S. W. Ashcraft, B. F. Bathel, J. A. Inman, and S. B. Jones, "*PLIF study of Mars Science Laboratory capsule reaction control system jets*," 41st AIAA Fluid Dynamics Conference, AIAA Paper 2011-3890, Honolulu, HI., June 27-30, 2011.

[119] C. T. Johansen, J. Novak, B. Bathel, S. W. Ashcraft, and P. M. Danehy, "*Comparison of MSL RCS jet computations with flow visualization and velocimetry*," 50th AIAA Aerospace Sciences Meeting, AIAA Paper 2012-0594, Nashville, TN., January 4-7, 2012.

[120] R. J. Balla, "Iodine Tagging Velocimetry in a Mach 10 Wake", AIAA Journal, Technical Note, (accepted).

[121] A. F. P. Houwing, D. R. Smith, J. S. Fox, P. M. Danehy, and N. R. Mudford, "*Laminar boundary layer separation at a fin-body junction in a hypersonic flow*," Shock Waves, 11, pp. 31-42, 2001.

[122] B. F. Bathel, P. M. Danehy, J. A. Inman, A. N. Watkins, S. B. Jones, W. E. Lipford, K. Z. Goodman, C. B. Ivey, and C. P. Goyne, "*Hypersonic Laminar Boundary Layer Velocimetry with Discrete Roughness on a Flat Plate*," AIAA Paper 2010-4998, 40th Fluid Dynamics Conference and Exhibit, Chicago, IL, June 28 - July 1, 2010.

[123] J. B. Michael, M. R. Edwards, A. Dogariu, and R. B. Miles, "*Femtosecond laser electronic excitation tagging for quantitative velocity imaging in air*," Applied Optics, 50(26), pp. 5158-5162, September 10, 2011.

[124] J. B. Michael, M. R. Edwards, A. Dogariu, and R. B. Miles, "*Velocimetry by femtosecond laser electronic excitation tagging (FLEET) of air and nitrogen*," 50th AIAA Aerospace Sciences Meeting, AIAA 2012-1053, Nashville, TN., January 9-12, 2012.

[125] M. R. Edwards, A. Dogariu, and R. B. Miles, "*Simultaneous Temperature and Velocity Measurement in Unseeded Air Flows with FLEET*," 51st AIAA Aerospace Sciences Meeting, AIAA 2013-0043, Grapevine, TX., January 7-10, 2013.

[126] P. Barker, A. Bishop, and H. Rubinsztein-Dunlop, "*Supersonic velocimetry in a shock tube using laser enhanced ionization and planar laser induced fluorescence*," Appl. Phys. B, 64 (3), pp. 369-376, 1997.

[127] P. F. Barker, A. M. Thomas, T. J. McIntyre, and H. Dunlop-Rubinsztein, "*Velocimetry and Thermometry of Supersonic Flow Around a Cylindrical Body*," AIAA Journal, 36 (6), pp. 1055-1060, June 1998.

[128] B. N. Littleton, A. I. Bishop, T. J. McIntyre, P. F. Barker, and H. Dunlop-Rubinsztein, "*Flow tagging velocimetry in a superorbital expansion tube*," Shock Waves, 10, pp. 225-228, 2000.

[129] R. Miles, C. Cohen, J. Connors, P. Howard, S. Huang, E. Markovitz, and G. Russell, "*Velocity measurements by vibrational tagging and fluorescent probing of oxygen*," Optics Letters, 12 (11), pp. 861-863, November, 1987.

[130] R. B. Miles, D. Zhou, B. Zhang, W. R. Lempert, and Z-S. She, "*Fundamental Turbulence Measurements by Relief Flow Tagging*," AIAA Journal, 31(3), March, 1993.

[131] R. B. Miles, J. Conners, E. Markovitz, P. Howard, and G. Roth, "*Instantaneous supersonic velocity profiles in an underexpanded sonic air jet by oxygen flow tagging*," Physics of Fluids A, 1(2), pp. 389-393, February, 1989.

[132] R. B. Miles, J. Grinstead, R. H. Kohl, and G. Diskin, "*The RELIEF flow tagging technique and its application in engine testing facilities and for helium-air mixing studies*," Measurement Science and Technology, 11(9), pp. 1272-1281, September, 2000.

[133] L. R. Boedeker, "*Velocity measurement by H_2O photolysis and laser-induced fluorescence of OH*," Optics Letters, 14 (10), pp. 473-475, May 15, 1989.

[134] J. A. Wehrmeyer, L. A. Ribarov, D. A. Oguss, F. Batliwala, R. W. Pitz, and P. A. DeBarber, "*Flow tagging velocimetry for low and high temperature flowfields*," *37th AIAA Aerospace Sciences Meeting*, Reno, NV, 1999.

[135] J. A. Wehrmeyer, L. A. Ribarov, D. A. Oguss, R. W. and Pitz, "*Flame flow tagging velocimetry with 193-nm H_2O photodissociation*," Applied Optics, 38 (33), pp. 6912-6917, November, 20, 1999.

[136] L. A. Ribarov, J. A. Wehrmeyer, S. Hu, and R. W. Pitz, "*Multiline hydroxyl tagging velocimetry measurements in reacting and nonreacting experimental flows*," Experiments in Fluids, 37, pp. 65-74, 2004.

[137] L. A. Ribarov, S. Hu, J. A. Wehrmeyer, R. W. and Pitz, "*Hydroxyl tagging velocimetry method optimization: signal intensity and spectroscopy*," Applied Optics, 44 (31), pp. 6616-6626, November, 1, 2005.

[138] R. W. Pitz, M. D. Lahr, Z. W. Douglas, J. A. Wehrmeyer, S. Hu, C. D. Carter, K-Y. Hsu, C. Lum, and M. M. Koochesfahani, "*Hydroxyl tagging velocimetry in a supersonic flow over a cavity*," Applied Optics, 44(31), pp. 6692-6700, November 1, 2005.

[139] M. D. Lahr, R. W. Pitz, Z. W. Douglas, and C. D. Carter, "*Hydroxyl-Tagging-Velocimetry Measurements of a Supersonic Flow over a Cavity*," Journal of Propulsion and Power, 26 (4), pp. 790-797, July – August 2010.

[140] A. M. ElBaz, and R. W. Pitz, "*N_2O molecular tagging velocimetry*," Applied Physics B, 106, pp. 961-969, 2012.

[141] R. W. Pitz, T. M. Brown, S. P. Nandula, P. A. Skaggs, P. A. DeBarber, M. S. Brown, and J. Segall, "*Unseeded velocity measurement by ozone tagging velocimetry*," Optics Letters, 21 (10), pp. 755-757, 1996.

[142] L. A. Ribarov, J. A. Wehrmeyer, F. Batliwala, R. W. Pitz, and P. A. DeBarber, "*Ozone Tagging Velocimetry Using Narrowband Excimer Lasers*," AIAA Journal, 37(6), June 1999.

[143] N. J. Dam, R. J. H. Klein-Douwel, N. M. Sijtsema, and J. J. ter Meulen, "*Nitric oxide flow tagging in unseeded air*," Optics Letters, 26 (1), pp. 36-38, January 1, 2001.

[144] N. M. Sijtsema, N. J. Dam, R. J. H. Klein-Douwel, and J. J. ter Meulen, "*Air Photolysis and Recombination Tracking: A New Molecular Tagging Velocimetry Scheme*," AIAA Journal, 40 (6), pp. 1061-1064, June 2002.

[145] W. P. N. Van der Lann, R. A. L. Tolboom, N. J. Dam, and J. J. ter Meulen, "*Molecular tagging velocimetry in the wake of an object in supersonic flow*," Experiments in Fluids, 34, pp. 531-534, 2003.

[146] J. Bominaar, M. Pashtrapanska, T. Elenbaas, N. Dam, H. ter Meulen, W. van de Water, "*Writing in turbulent air*," Physical Review E, 77, 2008.

[147] C. Orlemann, C. Schulz, and J. Wolfrum, "*NO-flow tagging by photodissociation of NO_2. A new approach for measuring small-scale flow structures*," Chem. Phys. Lett., 307, pp. 15-20, 1999.

[148] N. Shinji, M. Kasahara, M. Tsue, and M. Kono, "*Velocity Measurements of Reactive and Non-reactive Flows by NO-LIF Method Using NO_2 Photodissociation*," Heat Transfer – Asian Research, 34 (1), pp. 40-52, 2005.

[149] A. G. Hsu, R. Srinivasan, R. D. W. Bowersox, and S. W. North, "*Molecular Tagging Using Vibrationally Excited Nitric Oxide in an Underexpanded Jet Flowfield*," AIAA Journal, 47 (11), pp. 2597-2604, November, 2009.

[150] N. Jiang, M. Nishihara, and W. R. Lempert, "*500 kHz NO_2 Molecular Tagging Velocimetry in a Mach 5 Wind Tunnel*," 27th AIAA Aerodynamic Measurement Technology and Ground Testing Conference, AIAA 2010-4348, Chicago, IL., Jun 28-July 1, 2010.

[151] R. Sánchez-González, R. Srinivasan, R. D. W. Bowersox, and S. W. North, "*Simultaneous velocity and temperature measurements in gaseous flow fields using the VENOM technique*," Optics Letters, 36(2), pp. 196-198, January 15, 2011.

[152] R. Sánchez-González, R. Srinivasan, R. D. W. Bowersox, and S. W. North, "*Simultaneous velocity and temperature measurements in gaseous flowfields using the vibrationally excited nitric oxide monitoring technique: a comprehensive study*," Applied Optics, 51(9), pp. 1216-1228, March 20, 2012.

[153] B. F. Bathel, P. M. Danehy, C. T. Johansen, S. B. Jones, and C. P. Goyne, "*Hypersonic Boundary Layer Measurements with Variable Blowing Rates Using Molecular Tagging Velocimetry*," AIAA Paper 2012-2886, 28th AIAA Aerodynamic Measurement Technology, Ground Testing, and Flight Testing Conference, New Orleans, LA., June 25-28, 2012.

[154] B. F. Bathel, C. T. Johansen, S. B. Jones, P. M. Danehy, and C. P. Goyne, "*Trip-induced Transition Measurements in a Hypersonic Boundary Layer Using Molecular Tagging Velocimetry*," 51st AIAA Aerospace Sciences Meeting, AIAA 2013-0042, Grapevine, TX., January 7-10, 2013.

[155] I. Boxx, M. Stöhr, C. Carter, and W. Meier, "*Sustained multi-kHz flamefront and 3-component velocity-field measurements for the study of turbulent flames*, Applied Physics B, 95(1), pp. 23-29, April, 2009.

[156] N. Jiang, M. Webster, W. R. Lempert, J. D. Miller, T. R. Meyer, C. B. Ivey, and P. M. Danehy, "*MHz-rate nitric oxide planar laser-induced fluorescence imaging in a Mach 10 hypersonic wind tunnel*," Applied Optics, 50(4), February 1, 2011.

[157] N. Jiang, J. Bruzzese, R. Patton, J. Sutton, R. Yentsch, D. V. Gaitonde, W. R. Lempert, K. D. Miller, T. R. Meyer, R. Parker, T. Wadham, M. Holden, and P. M. Danehy, "*NO PLIF imaging in the CUBRC 48-inch shock tunnel*," Experiments in Fluids, 53, pp. 1637-1646, 2012.

[158] B. Yip, R. L. Schmitt, and M. B. Long, "*Instantaneous three-dimensional concentration measurements in turbulent jets and flames*," Optics Letters, 13(2), pp. 96-98, February, 1988.

[159] P. M. Danehy, B. F. Bathel, J. A. Inman, D. W. Alderfer, and S. B. Jones, "*Stereoscopic Imaging in Hypersonic Boundary Layers using Planar Laser-Induced Fluorescence*," 26th AIAA Aerodynamic Measurement Technology and Ground Testing Conference, AIAA 2008-4267, Seattle, WA., June 23-26, 2008.

[160] C. S. Combs, N. T. Clemens, P. M. Danehy, B. F. Bathel, R. Parker, T. Wadhams, M. Holden, and B. Kirk, "*NO PLIF Visualizations of the Orion Capsule in LENS-I*," 51st AIAA Aerospace Sciences Meeting, AIAA 2013-0033, Grapevine, TX., January 7-10, 2013.

[161] R. B. Miles, W. R. Lempert and J. N. Forkey, "Laser Rayleigh Scattering," Meas. Sci. Technol. p. R33-R51, v.12, 2001.

[162] Springer Handbook of Experimental Fluid Mechanics, Volume 1, edited by Cameron Tropea, Alexander L. Yarin, John F. Foss, ISBN-10: 3540251413 Springer, 1st Ed. 2007.

[163] G. C. Baldwin, "An Introduction Nonlinear Optics," Plenum Press, New York, 1969.

[164] A. Thorne, U. Litzén, and S. Johansson, Spectrophysics: Principles and Applications, Berlin Heidelberg, 1999.

[165] P. Magre and R. W. Dibble, Finite chemical kinetic effects in a subsonic turbulent hydrogen flame, Combust. Flame 73, 195, 1988.

[166] V. Bergmann, W. Meier, D. Wolff, and W. Stricker, "Application of Spontaneous Raman and Rayleigh Scattering and 2D LIF for the characterization of a Turblent $CH_4/H_2/N_2$ Jet Diffusion Flame," appl. Phys. B, vol. 66, pp. 489-502, 1998.

[167] Q.V. Nguyen, R.W. Dibble, C.D. Carter, G.J. Fiechtner and R.S. Barlow, "Raman-LIF Measurement of Temperature, Major Species, OH and NO in a Methane-Air Bunsen Flame," Combust. Flame, vol. 105, pp. 499-510, 1996.

[168] R. G. Seasholtz and A. E. Buggele, "Improvement in Suppression of Pulsed Nd:YAG Laser Light With Iodine Absorption Cells for Filtered Rayleigh Scattering Measurements," NASA TM–113177.

[169] G. S. Elliott, M. Samimy, S. A. Arnette, "Details of a Molecular Filter-Based Velocimetry Technique," Paper AIAA-94-0490, 32nd Aerospace Sciences Meeting & Exhibit, Reno, NV, January 10-13, 1994.

[170] G. S. Elliott, M. Samimy, S. A. Arnette "A molecular filter based velocimetry technique for high speed flows," Experiments in Fluids, Volume 18, Issue 1-2, pp 107-118, December 1994.

[171] R.G. Seasholtz, A.E. Buggele, and M.F. Reeder, "Flow Measurements Based on Rayleigh Scattering and Fabry-Perot Interferometer," Optics and Lasers in Engineering, Vol. 27, No. 6, 1997, pp. 543-570.

[172] D. Bivolaru, M. V. Otugen, A. Tzes, and G. Papadopoulos, "Image Processing for Interferometric Mie and Rayleigh Scattering Velocity Measurements," AIAA J.Vol. 37, No. 6, June 1999.

[173] D. Bivolaru, P. M. Danehy, R. L. Gaffney, Jr. and A. D. Cutler, "Direct-View Multi-Point Two-Component Interferometric Rayleigh Scattering Velocimeter," 46th AIAA Aerospace Sciences Meeting and Exhibit, Reno, Nevada, AIAA Paper 2008-236, January 7-10, 2008.

[174] A. F. Mielke-Fagan, K. A. Elam, and M. M. Clem, "Multiple-Point Mass Flux Measurement System Using Rayleigh Scattering," AIAA-2009-528, 2009 47th AIAA Aerospace Sciences Meeting Including The New Horizons Forum and Aerospace Exposition, Orlando, Florida, January 5 - 8 2009.

[175] J. Panda, R. G. Seasholtz, and K. A. Elam, "Investigation of noise sources in high-speed jets via correlation measurements," Journal of Fluid Mechanics, Vol. 537, pp.349-385, 2005.

[176] A.F. Mielke, K.A. Elam, C.J. Sung, "Multiproperty Measurements at High Sampling Rates Using Rayleigh Scattering," AIAA Journal, Vol. 47, No. 4, pp. 850-862, 2009.

[177] D. Bivolaru, A. D. Cutler, and P. M. Danehy, "Spatially- and Temporally-resolved Multi-parameter Interferometric Rayleigh Scattering," Paper AIAA-2011-1293, 49th AIAA Aerospace Sciences Meeting including the New Horizons Forum and Aerospace Exposition, Orlando, Florida, January 4-7, 2011.

[178] A. F. Fagan, M. M. Clem, K. A. Elam, "Improvement in Rayleigh Scattering Measurement Accuracy," 50th AIAA Aerospace Sciences Meeting including the New Horizons Forum and Aerospace Exposition, AIAA 2012-1060 Nashville, TN., January 9-12, 2012.

[179] J. Kojima, D. Fischer, and Q.-V. Nguyen, "Subframe burst gating for Raman spectroscopy in combustion," Optics Letters, Vol. 35, No. 9, p. 1323-1325, May 1, 2010.

[180] J. Kojima and D. G. Fischer, "Multiscalar Analyses of High-Pressure Swirl-Stabilized Combustion via Single-Shot Dual-SBG Raman Spectroscopy," Combust. Sci. technol. (under review).

[181] J. Kojima and Q.-V. Nguyen, "Single-shot rotational Raman thermometry for turbulent flames using a low-resolution bandwidth technique," Meas. Sci. Technol. 19 (2008).

[182] S. M. Schoenung, R. E. Mitchell, Comparison of Raman and Thermocouple Temperature Measurements in Flames, Combust Flame 35 (1979) 207-211.

[183] A.D. Cutler, G. Magnotti, L. M. L. Cantu, E. C. A. Gallo, P.M. Danehy and R. Baurle, R. Rockwell, C. Goyne, and J. McDaniel "Measurement of Vibrational Non-equilibrium in a Supersonic Freestream using Dual-Pump CARS" AIAA-2012-3199, 28th Aerodynamic Measurement Technology, Ground Testing, and Flight Testing Conference, New Orleans, Louisiana, June 25-28, 2012.

[184] J. A. Wehrmeyer, S. Yeralan, and K. S. Tecu, "Linewise Raman-Stokes/anti-Stokes temperature measurements in flames using an unintensified charge-coupled device," Appl. Phys. B. 62, p. 21–27, 1996.

[185] F. Rabenstein, A. Leipertz, Two-Dimensional Temperature Determination in the Exhaust Region of a Laminar Flat-Flame Burner with Linear Raman Scattering, Appl Opt 36 (1997) 6989-6996.

[186] J. Kojima, and Q.-V. Nguyen, "Strategy for Multiscalar Raman Diagnostics in High-Pressure Hydrogen Flames," In: New Developments in Combustion Research (Edited by W. J. Carey), ISBN: 1-59454-826-9, NOVA Science Publishers, New York, (2006), pp. 227-256.

[187] S. P. Sharma, S. M. Ruffin, W. D. Gillespie and S. A. Meyer, "Vibrational Relaxation Measurements in an Expanding Flow Using Spontaneous Raman Scattering," J. of Thermophys. and Heat Trans. Vol. 7, No. 4, Oct.-Dec. 1993.

[188] T. M. Dyer, "Rayleigh scattering measurements of time-resolved concentration in a turbulent propane jet,"AIAA Journal, vol. 17, Aug. 1979, p. 912-914.

[189] R. W. Boyd, Nonlinear Optics, 3rd Ed., Academic Press, 2008.

[190] R. P. Lucht, "Three-laser coherent anti-Stokes Raman scattering measurements of two species," *Optics Letters*, Vol. 12, No. 2, Feb. 1987, pp. 78-80.

[191] S. O'Byrne, P. M. Danehy, S. A. Tedder, A. D. Cutler, "Dual-Pump Coherent Anti-Stokes Raman Scattering Measurements in a Supersonic Combustor," *AIAA Journal*, Vol. 45, No. 4, p. 922-933, April 2007.

[192] R. E. Palmer, The CARSFT Computer Code for Calculating Coherent Anti-Stokes Raman Spectra: User and Programmer Information, Sandia report SAND89-8206, Feb. 1989.

[193] A. D. Cutler, G. Magnotti, "CARS Spectral Fitting with Multiple Resonant Species Using Sparse Libraries," *J. Raman Spectroscopy*, Vol. 42, Issue 11, 2011, pp. 1949-1957.

[194] K. M. Bultitude, P.M. Danehy, E. Fraval, J.S. Fox, A.F.P. Houwing "Broadband coherent anti-Stokes Raman spectroscopy (BB-CARS) in flames and hypersonic flows," 2nd Australian Conference on Laser Diagnostics in Fluid Mechanics and Combustion, Monash University, Melbourne Australia, 1999.

[195] W. D. Kulatilaka, N. Chai, S. V. Naik, N. M. Laurendeau, R. P. Lucht, J. P. Kuehner, S. Roy, J. R. Gord, "Measurement of nitric oxide concentrations in flames by using electronic-resonance-enhanced coherent anti-Stokes Raman scattering," *Optics Letters*, Vol. 31, Issue 22, pp. 3357-3359, http://dx.doi.org/10.1364/OL.31.003357, 2006.

[196] S. Roy, J. R. Gord, A. K. Patnaik, "Recent advances in coherent anti-Stokes Raman scattering spectroscopy: Fundamental developments and applications in reacting flows," *Progress in Energy and Combustion Science*, Vol. 36, Issue 2, pp. 280-306, ISSN 0360-1285, 10.1016/j.pecs.2009.11.001, April 2010.

[197] R. P. Lucht, P. J. Kinnius, S. Roy, J. R. Gord, "Theory of femtosecond coherent anti-Stokes Raman scattering spectroscopy of gas-phase transitions," *J. Chem. Phys*. 127, 044316, http://dx.doi.org/10.1063/1.2751184, 2007.

[198] R. P. Lucht, S. Roy, T. R. Meyer, J. R. Gord, "Femtosecond coherent anti-Stokes Raman scattering measurement of gas temperatures from frequency-spread dephasing of the Raman coherence," *Appl. Phys. Lett*. 89, 251112, http://dx.doi.org/10.1063/1.2410237, 2006.

[199] T. R. Meyer, S. Roy, J. R. Gord, "Improving Signal-to-Interference Ratio in Rich Hydrocarbon–Air Flames Using Picosecond Coherent Anti-Stokes Raman Scattering," *Applied Spectroscopy*, Vol. 61, Issue 11, pp. 1135-1140, 2007.

[200] P. S. Hsu, A. K. Patnaik, J. R. Gord, T. R. Meyer, W. D. Kulatilaka, S. Roy, "Investigation of optical fibers for coherent anti-Stokes Raman scattering (CARS) spectroscopy in reacting flows," Experiments in Fluids, Volume 49, Issue 4, pp 969-984, October 2010.

[201] M. A. Woodmansee, J. C. Dutton, R. P. Lucht, "Experimental Measurements of Pressure, Temperature, and Density Measurements in an Underexpanded Sonic Jet Flowfield," Paper No. AIAA 99-3600, presented at the 30th AIAA Fluid Dynamics Conference, Norfolk, VA., June 28-July 1, 1999.

[202] J. Zheng, J. B. J. B. Snow, D. V. Murphy, A. Leipertz, R. K. Chang, R. L. Farrow, "Experimental comparison of broadband rotational coherent anti-Stokes Raman scattering (CARS) and broadband vibrational CARS in a flame," *Optics Letters*, Vol. 9, No. 8, pp. 341-343, August 1984.

[203] A. D. Cutler, G. Magnotti, L. M. L. Cantu, E. C. A. Gallo, P. M. Danehy, R. D. Rockwell, C. P. Goyne, J. C. McDaniel, "Dual-Pump CARS Measurements in the University of Virginia's Dual-Mode Scramjet: Configuration "C"," AIAA-2013-0335, 51st Aerospace Sciences Meeting, Grapevine, TX, 7-10 Jan, 2013.

[204] G. Magnotti, A.D. Cutler and P.M. Danehy, "Development of a Dual-Pump CARS System for Measurements in a Supersonic Combusting Free Jet", Paper AIAA-2012-1193, presented at the 50th AIAA Aerospace Sciences Meeting, Nashville TN., January 9-12, 2012.

[205] T. R. Salyer, S. H. Collicott, and S. P. Schneider, "Feedback Stabilized Laser Differential Interferometry for Supersonic Blunt Body Receptivity Experiments," AIAA-2000-0416, 38th Aerospace Sciences Meeting & Exhibit, Reno, NV, January 10-13, 2000.

[206] G. Smeets, and A. George, "Laser Differential Interferometer Applications in Gas Dynamics," Translation of ISL Internal Report 28/73, Original 1975, Translation, 1996.

[207] N. J. Parziale, J. E. Shepherd, and H. G. Hornung "Reflected Shock Tunnel Noise Measurement by Focused Differential Interferometry," 42nd AIAA Fluid Dynamics Conference and Exhibit, AIAA Paper, 2012-3261, June 2012.

[208] N. J. Parziale, J. E. Shepherd, and H. G. Hornung, "Differential Interferometric Measurement of Instability in a Hypervelocity Boundary Layer," AIAA J., Vol. 51, No. 3, p. 750-753, March 2013.

[209] G. E. A. Meier, "Hintergrund schlierenmessverfahren." Deutsche Patentanmeldung DE 199, no. 42 (1999): 856.

[210] H. Richard, and M. Raffel. "Principle and applications of the background oriented schlieren (BOS) method." Measurement Science and Technology 12, no. 9, p. 1576-1585, 2001.

[211] M. J. Hargather, and G. S. Settles. "Natural-background-oriented schlieren imaging." Experiments in fluids 48, no. 1, 59-68, 2010.

[212] T. Mizukaki, H. Tsukada, K. Wakabayashi, T. Matsumura, and Y. Nakayama, "Quantitative visualization of open-air explosions by using background-oriented schlieren with natural background," in: K. Kontis (ed) 28th International Symposium on Shock Waves 2:465–470, 2012.

[213] E. Goldhahn, and J. Seume. "The background oriented schlieren technique: sensitivity, accuracy, resolution and application to a three-dimensional density field." Experiments in Fluids 43, no. 2-3, p. 241-249, 2007.

[214] M. J Hargather and G. S. Settles. "A comparison of three quantitative schlieren techniques." Optics and Lasers in Engineering 50, no. 1 p. 8-17, 2012.

[215] L. Venkatakrishnan, and G. E. A. Meier. "Density measurements using the background oriented schlieren technique." Experiments in Fluids 37, no. 2, p. 237-247, 2004.

[216] M. G. Allen, "Diode laser absorption sensors for gas-dynamic and combustion flows," Meas. Sci. Technol. v.9 p. 545-562, 1998.

[217] R. K. Hanson, "Applications of quantitative laser sensors to kinetics, propulsion and practical energy systems," Proc. Combust. Inst. 33, 1–40 2011.

[218] K. M. Busa, E. N. Ellison, B. J. McGovern, and J. C. McDaniel G. S. Diskin, M. J. DePiro, D. P. Capriotti, and R. L. Gaffney, "Measurements on NASA Langley Durable Combustor Rig by TDLAT: Preliminary Results," 51st AIAA Aerospace Sciences Meeting including the New Horizons Forum and Aerospace Exposition, Paper AIAA 2013-0696, Grapevine TX., 7-10 January 2013.

[219] M. S. Brown, G. C. Herring, K. Cabell, N. Hass, T. F. Barhorst, and M. Gruber, "Optical Measurements at the Combustor Exit of the HIFiRE 2 Ground Test Engine," Paper AIAA 2012-0857, 50th AIAA Aerospace Sciences Meeting including the New Horizons Forum and Aerospace Exposition, Nashville, TN., 9-12 January 2012.

[220] L. Ma, X. Li, S. T. Sanders, A. W. Caswell, S. Roy, D. H. Plemmons, and J. R. Gord, "50-kHz-rate 2D imaging of temperature and H_2O concentration at the exhaust plane of a J85 engine using hyperspectral tomography," Optics Express, Vol. 21, Issue 1, pp. 1152-1162, 2013.

[221] P. M. Danehy, E. J. Friedman-Hill, R. P. Lucht and R. L. Farrow, "The effects of collisional quenching on degenerate four-wave mixing", App. Phys. B, Vol. B57, pp. 243-248, 1993.

[222] G. M. Lloyd, I.G. Hughes, R. Bratfalean, P. Ewart, "Broadband degenerate four-wave mixing of OH for flame thermometry," Appl Phys B, 67, pp. 107–113, 1998.

[223] E. B. Cummings, "Laser-induced thermal acoustics: simple accurate gas measurements," Opt. Lett. 19, 1361–1363, 1994.

[224] R. C. Hart, R. J. Balla, and G. C. Herring "Simultaneous velocimetry and thermometry of air by use of nonresonant heterodyned laser-induced thermal acoustics," Applied Optics, Vol. 40, Issue 6, pp. 965-968, 2001.

[225] R. C. Hart, G. C. Herring, and R. J. Balla, "Pressure Measurement in Supersonic Air Flow by Differential Absorptive Laser-Induced Thermal Acoustics," Optics Letters, Vol. 32, No. 12, pp. 1689–1691, 2007.

[226] R. C. Hart, G. C. Herring, and R. J. Balla, "Common-Path Heterodyne Laser-Induced Thermal Acoustics for Seedless Laser Velocimetry," Optics Letters, Vol. 27, No. 9, pp. 710–712, 2002.

[227] J. D. Garman and D. Dunn-Rankin, "Spatial Averaging Effects in CARS Thermometry of a Nonpremixed Flame," Comb. and Flame, v. 115, p. 481–486 (1998).

[228] D. Bivolaru, J. W. Lee, S. B. Jones, S. Tedder, P. M. Danehy, M. C. Weikl, G. Magnotti, and A. D. Cutler, "Mobile CARS - Rayleigh Instrument for Simultaneous Spectroscopic Measurement of Multiple Properties in Gaseous Flows", The '22nd International Congress on Instrumentation in Aerospace Simulation Facilities,' Asilomar Conference Center, Pacific Grove, California, June 10-14, 2007.

[229] L. P. Goss, D. D. Trump, W. F. Lynn, T. H. Chen, W. J. Schmoll, and W. M. Roquemore. "Second-generation combined CARS-LDV instrument for simultaneous temperature and velocity measurements in combusting flows." Review of Scientific Instruments 60, no. 4, 638-645, 1989.

[230] S. A. Tedder, J. L. Wheeler, A. D. Cutler, and P. M. Danehy, "Width-increased dual-pump enhanced coherent anti-Stokes Raman spectroscopy," Applied Optics Vol. 49, No. 8, pp. 1305–1313, March 2010.